
Copyright Undertaking

SYNTHESIS OF TWO-DIMENSIONAL LAYERED MATERIALS FOR ELECTROCATALYSIS AND PHOTODETECTION APPLICATIONS

MAK CHUN HIN

PhD

The Hong Kong Polytechnic University

2020

The Hong Kong Polytechnic University

Department of Applied Physics

Synthesis of Two-Dimensional Layered Materials for Electrocatalysis and Photodetection Applications

Mak Chun Hin

A thesis submitted in partial fulfillment of the

requirements for the degree of Doctor of Philosophy

December 2019

Certificate of Originality

I hereby declare that this thesis is my own work and that, to the best of my knowledge and belief, it reproduces no material previously published or written nor material which has been accepted for the award of any other degree or diploma, except where due acknowledgement has been made in the text.

_________________________(Signature)

_____Mak Chun Hin______(Name of candidate)

Abstract

Two dimensional layered materials (2DLMs) have been intensively researched for the electrical and optoelectronic applications in the past decade. The quantum confinement allows one to change the energy band level of the 2DLMs by changing their thickness. The optoelectronic and mechanical properties of 2DLMs exhibit a large difference between the bulk and their ultrathin counterparts. Also, the large surface to volume ratio of the nanomaterials allow one to easily modify their physical and chemical properties by surface modification. Depending on the specific application, the band structure or materials morphology can be engineered. In this work, we focused on the potential application of the 2DLMs. Firstly, graphene and palladium diselenide ($PdSe_2$) were synthesized and optimized for the phototransistors. For graphene-based transistor, the band structure modification was done by coating the zero-dimensional material bismuth silver sulfide ($AgBiS_2$) nanocrystals (NCs) on the graphene channel. Secondly, vertically aligned platinum diselenide ($PtSe_2$) films were synthesized for hydrogen evolution reaction (HER).

$AgBiS_2$ NCs are emerging optoelectronic materials due to their high absorption coefficient and solution-processability. We report a facile method to prepare $AgBiS_2$ nanocrystals in ambient conditions. The nanocrystals are of high crystallinity and without byproducts, which make them suitable for solution processable optoelectronic devices. To overcome the low responsivity of pristine graphene-based transistor, $AgBiS_2$ NCs were incorporated into the transistors. As a light absorber on the graphene channel, the responsivity of the phototransistors was highly enhanced by the photogating effect. The transistor was suitable for near infrared detection application.

Photodetectors with a high responsivity of 10^5 A W^{-1} for 895 nm wavelength at a low operation voltage of 0.1 V were demonstrated.

The wafer-scale polycrystalline $PdSe_2$ thin films with controllable thickness by the selenization of Pd films were prepared. The $PdSe_2$ film with the thickness of 9.2 nm was employed to be the transistor channel. A $PdSe_2$ photodetector can detect a broad wavelength ranging from 420 nm to 1200 nm. The responsivity and detectivity can reach 1.96×10^3 A W^{-1} and 1.72×10^{10} W $Hz^{-1/2}$ at $V_{DS} = 3$ V, respectively. As the phototransistor is driven by the photoconductive effect, a fast response time was achieved in hundreds of milliseconds. It shows a good balance between the responsivity and response time. This work demonstrated that the polycrystalline $PdSe_2$ films are promising for broadband photodetection.

Besides the photodetection based on the 2DLMs, 2DLMs are shown to have pronounced catalytic effect in HER activity. We synthesized the large area, vertically aligned $PtSe_2$ films by selenization of the platinum films. The thicknesses of the $PtSe_2$ films can be varied from 3.8 nm to 76 nm. The density of the vertically aligned $PtSe_2$ is increased with the Pt film thickness. The HER activity of the $PtSe_2$ can be enhanced significantly as the active edge site density increases. The maximum cathodic current density of 227 mA cm^{-2} can be obtained through increasing the edge density.

List of Publication

1. **Mak, C. H**.; Lin, S.; Rogee, L.; Lau, S. P.; Photoresponse of wafer-scale palladium diselenide films prepared by selenization method. *Journal of Physics D: Applied Physics* **2019,** *53*(6), 065102.

2. Zhai, L.; **Mak, C. H.**; Qian, J.; Lin, S.; Lau, S. P.; Self-reconstruction mechanism in $NiSe_2$ nanoparticles/carbon fiber paper bifunctional electrocatalysts for water splitting. *Electrochimica Acta* **2019,** *305*, 37-46.

3. Zeng, L. H.; Lin, S. H.; Li, Z. J.; Zhang, Z. X.; Zhang, T. F.; Xie, C.; **Mak, C. H.**; Chai Y.; Lau, S. P.; Luo. L.; Tsang, Y. H.; Fast, self-driven, air-Stable, and broadband photodetector based on vertically aligned $PtSe_2$/GaAs heterojunction. *Advanced Functional Materials* **2018,** *28*(16), 1705970.

4. **Mak, C. H.**; Qian, J.; Rogée, L.; Lai, W. K.; Lau, S. P.; Facile synthesis of $AgBiS_2$ nanocrystals for high responsivity infrared detectors. *RSC advances* **2018,** *8*(68), 39203-39207.

5. Qian, J.; San Chui, Y.; Li, G.; Lin, M.; Luk, C. M.; **Mak, C. H**.; Zhang, B.; Yan, F.; Tsang, Y. H.; Lau, S. P.; Kinetically controlled redox behaviors of $K_{0.3}$ MnO_2 electrodes for high performance sodium-ion batteries. *Journal of Materials Chemistry A* **2018,** *6*(23), 10803-10812.

6. Lin, S.; Liu, Y.; Hu, Z.; Lu, W.; **Mak, C. H.**; Zeng, L. H.; Zhao, J.; Li, Y.; Yan, F.; Zhang, X.; Lau, S. P.; Tunable active edge sites in $PtSe_2$ films towards hydrogen evolution reaction. *Nano Energy* **2017,** *42*, 26-33.

7. Xie, C.; **Mak, C.H.**; Tao, X.; Yan, F.; Photodetectors based on two-dimensional layered materials beyond graphene. *Advanced Functional Materials* **2017,** *27*(19), 1603886.

8. Yang, Z.; Jie, W.; **Mak, C. H.**; Lin, S.; Lin, H.; Yang, X.; Yan, F.; Lau, S. P.; Hao, J.; Wafer-scale synthesis of high-quality semiconducting two-dimensional layered InSe with broadband photoresponse. *ACS Nano* **2017,** *11*(4), 4225-4236.

Acknowledgements

There is an uncertainty principle in quantum physics. It states that you cannot simultaneously obtain accurate information of certain pairs of physical properties. However, I found that there is also an uncertainty principle when I write this acknowledgement. If someone asks me, “Are they the only people you want to say thank you?”, then “the uncertainty principle in writing acknowledgement” will appear. I will try to acknowledge all the people who supported me during my PhD study below.

First of all, I would like to thank my supervisor Prof. S. P. Lau for his professional and invaluable advices in my PhD study. His support, supervision and opinions helped me a lot during my research study. I wish to say thank you to Prof. Feng Yan and Dr. Chao Xie for the discussion of experiments during my study. I appreciate the generous helps from Dr. Wei Lu and Dr. Hardy Lui for the use of instrument.

It is my greatest honour to receive transmission electron microscopy (TEM) training in Prof. Xiaoqing Pan’s group from UC Irvine. During the attachment program, I gained substantial knowledge in TEM. They provided me useful help, discussion and assistance in the experiments.

My special thanks are also given to my colleagues for providing me with help and support throughout my study. They include Dr. C. M. Luk, Dr. Y. Y. Hui, Dr. S. H. Lin, Dr. Y. J. Zhu, Dr. S. N. Ma, Dr. B. Chen, Dr. Q. D. Tai, Dr. Y. Zhang, Dr. J. S. Qian, Dr.

M. K. Tsang, Dr. H. M. Yau, Dr. X. X. Chen, Miss Y. T. Wong, Mr. L. Rogée, Mr. W. K. Tsui, Mr. C. Y. Tang, Mr. K. H. Ho, Mr. C. M. Wong, Mr. Ken Ko and Miss L. L. Zhai. My study in PolyU was very fruitful because of the friendship with them.

Last but not least, I earnestly appreciate the encouragement and supports from my family during my research study. They always support me every day.

Table of Contents

List of Figures

List of Tables

Chapter 1 Introduction

1.1 Background and motivation

Two dimensional layered materials (2DLMs) exhibit strong primary bond along the in-plane direction and weak van der Waals force interaction along the out-of-plane direction.[1], [2] These properties make 2DLMs having anisotropic electronic properties. The conductivity in the in-plane direction is usually much higher than that in the out-of-plane direction. The research of 2DLMs enable a revolution in device fabrication and applications such as photodetectors, gas sensors and electrocatalysis. The 2DLM experiences the tunable physical and chemical properties due to the quantum confinement[2]–[4], which are easily observable in the thickness dependent photoluminescence/absorption measurements.[5] Previous researches have been demonstrated that changing the thickness is able to tune the materials properties for different applications.[2], [3], [6]

As the first discovered one-atomic-layer material, graphene was mechanically exfoliated (ME) from a bulk graphite using a tape in 2004.[7] Afterward, it has been widely studied for the optoelectronic and electrical applications such as phototransistor and electrodes for hydrogen evolution reaction (HER). Its semimetallic nature provides high electron mobility for electron transport and suitable for high speed communications, but its atomic thinness and gapless band structure hinder its light absorption.[1], [8] Therefore, even the graphene transistors show some photocurrent under light illumination by the “photoconductive” effect, but only a very low responsivity resulted and they are not favorable for photodetection. Nowadays, graphene can be prepared by chemical vapor deposition (CVD). With the appropriate growth recipes, the single layer graphene can be grown in large-area scale. This encourages the application of graphene in future.

In addition to graphene, one-layer or few-layer 2DLMs such as MoS_2, WS_2, black phosphorus (BP), etc. were researched for photodetection and HER.[9]–[14] Besides the high mechanical flexibility and high transparency, 2DLMs exhibit a high controllability in spectral coverage and conductance by tuning their thickness. [15] The quantum confinement effect enlarges the bandgap of the materials when their sizes reduce to nanoscale, vice versa. For instance, the bandgaps of black phosphorus (BP) are about 0.3 eV and 2.0 eV for its bulk form and 1-layer (1L) form, respectively.[16]–[18] However, their application is still at the bottleneck because of fluctuated performance. For example, the single-layer MoS_2 transistors from different groups with same fabrication method showed a large difference in responsivity which are ranging from7.5 mA W^{-1} to 880 A W^{-1} .[19], [20] Hence, except the measurement environment and transistor architecture, the synthesis of the materials plays an important role in the device performance.

In this thesis, the synthesis and application of the 2DLMs will be presented. 2DLMs based transistors and electrode were researched for photodetection and HER, respectively. 2DLM-based phototransistors are the transistors which use 2DLM as the conducting channel. They absorb the illuminated light and convert the energy to electrical signal. Pristine graphene transistors show a very weak responsivity due to the gapless structure and short lifetime of photocarriers. However, the energy band structure of graphene can be modulated by depositing the semiconducting NCs absorber on the graphene channel. The absorber will dope the graphene channel and modulate the work function of the graphene, which results in p-doping or n-doping to the graphene channel. Also, the absorbers improve the light sensing ability of the graphene transistor by “photogating effect”, which will be introduce in Chapter 2. The photodetection performance is usually better than that of graphene or NCs film itself. By considering the low absorbance of graphene itself, the sensing spectrum of the resultant transistor is similar to that of the absorber. Graphene transistor is an ideal platform to amplify the intrinsic optoelectronic properties of the NCs absorbers.

Several works demonstrated graphene transistors can achieve high responsivity by depositing the NC film on the graphene channel. For instance, PbS, $CsPbX_3$ (X = Cl, Br, I) and Si NCs were coated on the graphene transistor channel for high responsivity detection.[21]–[23] However the synthesis procedures of the NC solution usually need a long time. Moreover, the lead atoms in PbS and $CsPbX_3$ NCs can cause long term environmental and biological issues, which is inevitably increased the health concern of the users. Recently, $AgBiS_2$ NC, as a non-toxic and high stability material, showed a high infrared external quantum efficiency in solar cell with a bandgap fall in the infrared region (1.0–1.25 eV).[24] Furthermore, simple and cost effective synthesis method of functional NCs is favorable. To fabricate a nontoxic, high responsivity graphene transistor for infrared photodetection, a facile method of synthesizing $AgBiS_2$ NCs was developed. Comparing to the conventional hot injection method, the method can synthesize $AgBiS_2$ NCs in ambient environment with a much shorter time. Also, an n-type doping to the graphene transistor was observed after the NCs were coated on the graphene channel, indicating the work function modulation of graphene channel. The transistor was driven by the “photogating” effect and exhibited high responsivity under 895 nm light illumination. The thickness of the NC films was tuned to explore the relationship between the photodetection performance and the absorber thickness.

Besides graphene, another well-studied family of 2DLMs is the transition metal dichalcogenides (TMDCs). The members usually have a chemical formula of MY_2, where M is the chemical symbol of transition metal and Y is the chemical symbol of chalcogen. Except $PdSe_2$, the discovered TMDC members exhibit hexagonal crystal structure. Some of their semiconducting members such as MoS_2, $MoSe_2$, SnS_2, etc. were employed as phototransistor channel. Even their electronic mobilities are not comparable to that of graphene, they showed a better responsivity in photodetection than graphene due to their bandgap structure. Also, the choice of the channel thickness can change the absorption spectrum. It is rarely observed in bulk semiconducting materials. Hence the researches of TMDC phototransistors are still continuing.

Until now, the development of high-performance 2DLM photodetectors still encounter several problems. High gain/responsivity 2DLM based phototransistors usually suffer from long response time.[25] It is because the high responsivity is usually assisted by the charge trapping level.[1], [26] The slow rate of de-trapping not only leads to high responsivity but also the longer recovery time.[27] Hence the high responsivity 2DLM phototransistors may not suitable for fast response detection. A balance between response time and responsivity is needed for different applications. Furthermore, except a few works can synthesize centimeter scale 2DLM films, many 2DLM films fabricated by exfoliation or CVD were still in a few to hundreds of micron in size.[28]–[37] It is still a big challenge to have a wafer scale synthesis of 2DLMs. It is also one of the problems which hinder their large scale production for practical application. In this aspect, sulfurization or selenization of the metal precursor films provide a facile way to synthesize the 2DLM films. The size of the film can be predefined by the metal precursor.

Among the TMDC family, $PdSe_2$ has a unique in-plane pentagonal crystal structure.[38] As a high mobility semiconductor, the $PdSe_2$-based photodiode demonstrated excellent performance.[39], [40] We employed selenization of palladium film to synthesize the polycrystalline $PdSe_2$ film in wafer scale. The film was investigated for photodetection by fabricating $PdSe_2$ phototransistor. The polycrystalline $PdSe_2$ transistor showed a p-type semiconductor in transfer characteristic curve, which was different to the previously reported $PdSe_2$ transistor fabricated by ME. The photodetection of the $PdSe_2$ transistor was based on "photoconductive" effect. The photodetection performance of the transistor is comparable to other CVD grown TMDCs based transistors. The result indicates the selenization is suitable for synthesizing $PdSe_2$.

Besides the phototransistor application, TMDCs have been utilized as the electrocatalysts for HER. Since hydrogen as energy source has high energy density and environmental friendly, it is favorable to energy storage and has been considered as an alternative energy carrier of the future.[41], [42] In past decades, noble-metal-based catalysts have been used to provide effective proton reduction sites to reduce H^+ to H_2 gas. However, their scarcity and high-cost hinder their use in HER.[43] TMDC materials such as MoS_2, WS_2, $MoSe_2$ have been shown to be the promising catalysts for HER.[13], [14], [44], [45] As the semiconductor catalysts, their conduction and valence band level positions are also suitable for the reduction of H^+.[43] The unsaturated sulfur atoms in MoS_2 are beneficial to HER.[13], [44]–[47] They can serve as the active sites to the hydrogen atoms and catalyze the production of hydrogen gas. Nowadays, the focus of the researches is to improve their HER so that their activities are comparable to the conventional metal catalysts. Maximizing the active sites of the TMDCs would be a possible way to achieve the high HER. To maximize the area density of the exposed edge and improve the electron transfer between the electrodes and electrolyte, vertically aligned TMDC films would be one of the favorable structures for HER.

Some special synthesis methods were developed to synthesize the TMDC electrodes with exposed edges. For instance, ball milling was applied to mix WO_3 powders and sulfur powders to have a homogeneous mixture. After the sulfurization, the mixture the flower – like WS_2 nanoflowers were synthesized. In another work, vertically aligned WS_2 was synthesized by employing the anodization to tungsten foil followed by sulfurization. Both WS_2 nanoflowers and vertically aligned WS_2 showed a higher current density than pristine WS_2 nanosheets in HER.[14], [45] However, the report on facile synthesis of the vertically aligned TMDCs is rare. Except the vertically aligned MoS_2 and $MoSe_2$ were reported by sulfurization and selenization of the Mo film,[13] facile synthesis of large area vertically aligned TMDCs without special tactics are seldom seen. The development in HER of the TMDC is still a continuing research topic.

As a semimetallic TMDC member, $PtSe_2$ has a high in-plane conductivity for electron transfer. We synthesized $PtSe_2$ films by selenization of platinum precursor films. We found that vertically aligned $PtSe_2$ can be grown by changing the thickness of the precursor films. The thicker the precursor film, the larger the density with vertically aligned $PtSe_2$. The vertical alignment of $PtSe_2$ can be observed on different substrates. The film structure is similar to previously reported vertically aligned MoS_2 and $MoSe_2$ films which has been employed for HER electrodes. Considering the exposed edges of the vertically aligned $PtSe_2$, the films were transferred onto the glassy carbon (GC) electrode for HER activity. Under a three-electrode system with a standard electrolyte of 0.5M H_2SO_4, the HER performance of the films were compared with the platinum and the GC electrodes. The films showed significantly enhancement to GC electrode in HER. Among the tested films, the best $PtSe_2$ film showed a high exchange current density of 1.5×10^{-5} A cm^{-2} and turnover 0.054 s^{-1}, The result is better than that of the vertically aligned MoS_2 and $MoSe_2$

electrodes under the similar test conditions. The results confirm the vertically aligned TMDCs are beneficial to HER.

In this work, $AgBiS_2$ nanocrystals were incorporated into graphene transistors for their near infrared detection application. The wafer-scale $PdSe_2$ films were fabricated by selenization of Pd films. A broad photodetection ranging from 420 nm to 1200 nm was demonstrated. The synthesis method was also extended to fabricate large-area and edge-rich $PtSe_2$ for HER.

1.2 Thesis overview

In this project, we have investigated the ability of 2DLMs for the photodetector and HER applications. Graphene and $PdSe_2$ based phototransistors and $PtSe_2$ based electrodes for HER were demonstrated. $AgBiS_2$ NCs were synthesized for modifying the work function of the graphene transistor and improve the performance of photodetection. High responsivity phototransistors and HER based on 2DLMs were demonstrated.

In Chapter 2, the brief introduction of 2DLM synthesis and photodetection are provided.

The fabrication of the 2DLMs and performance of their FET are discussed. Parameters for photodetection and the sensing mechanism of 2DLM transistors, photoconductive and photogating effect, are described.

In Chapter 3, the experimental details of the project are described. The content divides into two main sections. The first section includes the synthesis of the materials used in this project, which are monolayer graphene, $AgBiS_2$ NCs and $PdSe_2$ films. The second section introduces the techniques for the optical, electrical and structural characterizations, which are X-ray diffraction (XRD), Raman spectroscopy, scanning electron microscopy (SEM), transmitting microscopy (TEM), selected area electron diffraction (SAED), energy-dispersive X-ray spectroscopy (EDX), Fourier Transform Infrared (FTIR) spectroscopy, Atomic force microscopy (AFM), UV-Vis-NIR spectrometer and the photodetection of the transistor.

In Chapter 4, the synthesis and characterization of CVD grown graphene and $AgBiS_2$ NCs are described. The fabrication process of the graphene/$AgBiS_2$ transistors, the photodetection performance of the transistors and the performance variation of the absorber thickness are discussed.

In Chapter 5, the synthesis and characterization of wafer-scale $PdSe_2$ films are provided. The material properties of the films are described. The photodetection of the $PdSe_2$ transistor are discussed.

In Chapter 6, the synthesis and characterization of the vertically aligned $PtSe_2$ films are given. The material properties of the films are described. The HER activity of the vertically aligned $PtSe_2$ films on glassy carbon electrode are discussed.

In Chapter 7, the work in this thesis is concluded and the future work is discussed.

Chapter 2 Literature review

2.1 Introduction

In this chapter, the preparation methods for nanoscale 2DLMs are reviewed. A brief review on the 2DLM based photodetectors together with the critical parameters and the figure of merit for photodetectors are given. The development of the 2DLMs for HER is provided. The typical parameters to evaluate the performance of the HER are also presented.

2.2 Materials Preparation

2.2.1 Mechanical exfoliation (ME)

The mechanical exfoliation was firstly demonstrated by Geim and co-worker to isolate graphene (1L or FL of graphite) from highly-oriented pyrolytic graphite.[7] A Scotch tape was used to cleave the graphite crystals by breaking the van der Waals force between the layers of graphite. **Figure 2.1** shows the procedure of making graphene sheets by the Scotch tape method. The layer of graphite flake is successively peeling off by the tape until only one layer of graphite remained. [48] This technique provides minimal defects and suitable for fundamental researches. Following this technique, other FL BP, MoS_2, WS_2 flakes were cleaved. [10], [16], [49], [50] However, the method is still suffered from scalable production and low controllability in size and thickness.

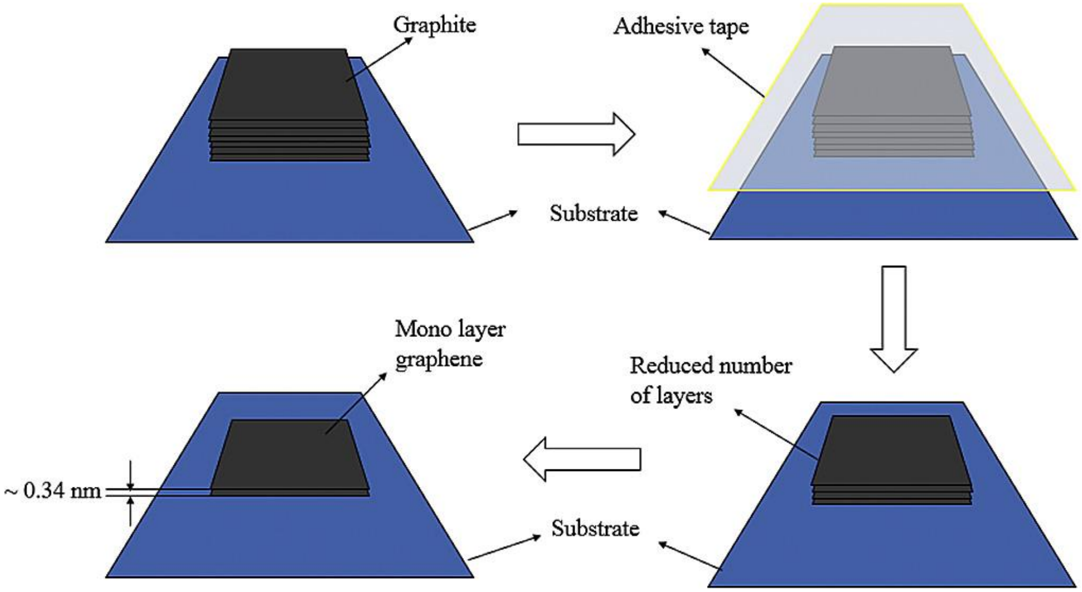

Figure 2.1 Schematic representation of sequential steps followed to exfoliate graphene layers using the Scotch tape method. Graphs and captions are adopted from reference [48].

2.2.2 Liquid exfoliation

Apart from the mechanical exfoliation, liquid exfoliation is another method to produce 2DLM flakes in solution (e.g. deionized water, ethanol, and dimethylformamide) by sonication.[51]–[53]. **Figure 2.2** illustrates the procedure of liquid exfoliation for 2DLM powder. After the powder is mixed with the solution (**Figure 2.2A**), external energy from the sonication can cleave the 2DLM into flakes which disperse in the solution (F**igure 2.2B**). Centrifugation is able to provide the size selection of the flakes by controlling the rotational speed. At a slower speed, the smaller flakes (lighter in weights) disperse in the supernatant and the larger flakes (heavier in weight) become the sediment. Size selection can be done by centrifuging the supernatant with the higher speed and collecting the sediment successively. Hence, the solutions with different size distributions can be obtained. Moreover, the concentration can be conveniently control while during the dilution of the sediment in solution. However, this method exhibits a relatively low production of large-size flakes or single-layer flakes, which are highly desired for research and some of the application.

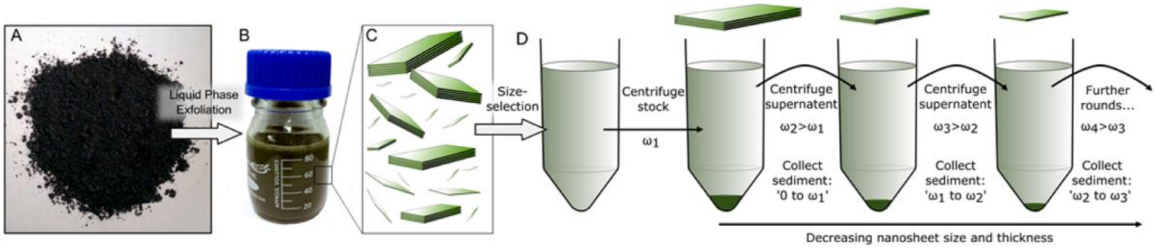

Figure 2.2 Illustration of liquid exfoliation and size selection. (A) Photograph of a typical starting material (here WS_2 powder) yielding. (B) Colloidal dispersions after the exfoliation containing. (C) A mixture of nanosheets with varying lateral sizes and thicknesses. (D) Size selection by centrifugation with subsequently increasing rotational speeds ω. The supernatant after each step is subjected to another centrifugation at higher centrifugal acceleration. Graphs and captions are modified from reference [53]

Zhang's group developed a special kind of liquid exfoliation which is based on lithium ion (Li^+) intercalation into the 2DLMs by electrochemical system. [54] As shown in **Figure**

2.3, the bulk 2DLM crystal (e.g. MoS_2, WS_2, TiS_2, etc.) and lithium foil serve as the cathode and anode in a lithium battery system, respectively. In the discharge process, Li^+ ions intercalate the layers and the interlayer distance of the 2DLMs is expanded. Thus, the van der Waals interaction is weakened and it is beneficial to exfoliation. Also, the intercalation can be controlled by monitoring the discharge curve during the process. The intercalated Li^+ is reduced to Li during the discharge process. After that, the compound formed in the cathode is cleaned and undergo liquid exfoliation with water (or ethanol). The water or ethanol reacts with Li, H_2 gas is produced between the layers and further separate the layer of the 2DLM. Then following a sonication process, the 2DLM is exfoliated into nanosheets with hundreds of nanometer in size.

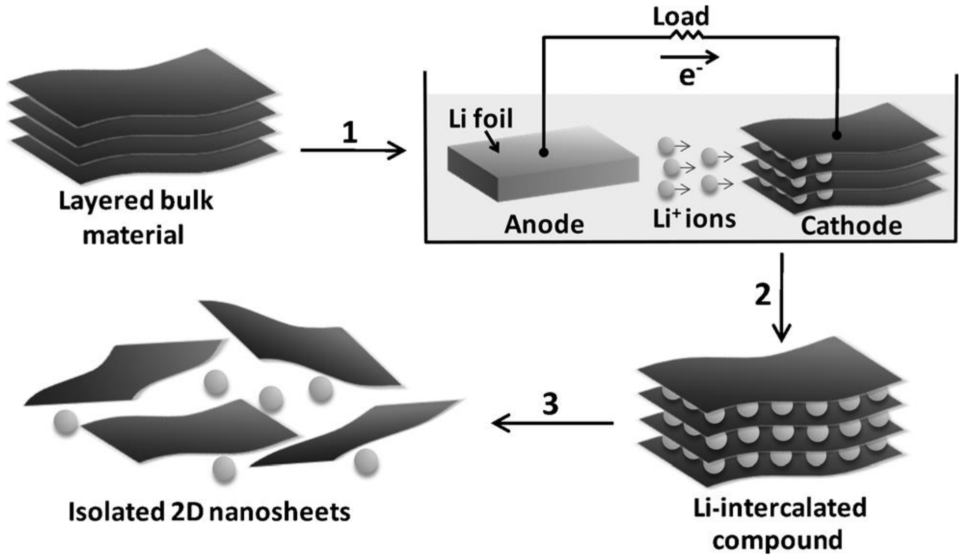

Figure 2.3 Electrochemical lithiation process for the fabrication of 2D nanosheets from the layered bulk material. Graphs and captions are adopted from reference [54].

2.2.3 Chemical vapor deposition (CVD)

CVD techniques have been developed to synthesize large-area 2DLMs. The CVD growth of 2DLMs needs an optimization in pressure, mass flow control of gas, selection of precursors/gases, temperature of heat zones, substrate and growth time. Large-area graphene films were demonstrated by CVD using metal foil such as copper or nickel as catalyst.[55], [56] The growing of TMDC films by CVD have also been reported.

To illustrate the growth of TMDCs, we select WS_2 as an example. The precursors of growing WS_2 can be WO_3, WCl_6, sulfur powder or H_2S gas.[28], [31], [57], [58] Under a suitable growth recipe, the carrier gas delivers the vapor of the precursors to the substrate. **Figure 2.4A** shows the setup for the growth of WS_2.[57] The WO_3 and sulfur powder are heated according to the temperature profiles as shown in **Figure 2.4B**. The morphology of the WS_2 films can be tuned from triangle with micron size to continuous films with centimeter size by introducing H_2 gas, as shown in **Figure 2.4 C-F.** The results indicate the gases used play an important role in the growth of 2DLMs. Synthesizing the centimeter scale of 2DLMs with precise control in thickness is still a great challenge. Also, the lateral size of many 2DLMs produced by CVD is still limited in several hundred microns. Further development and optimization of CVD process to grow large-area 2DLMs are still needed.

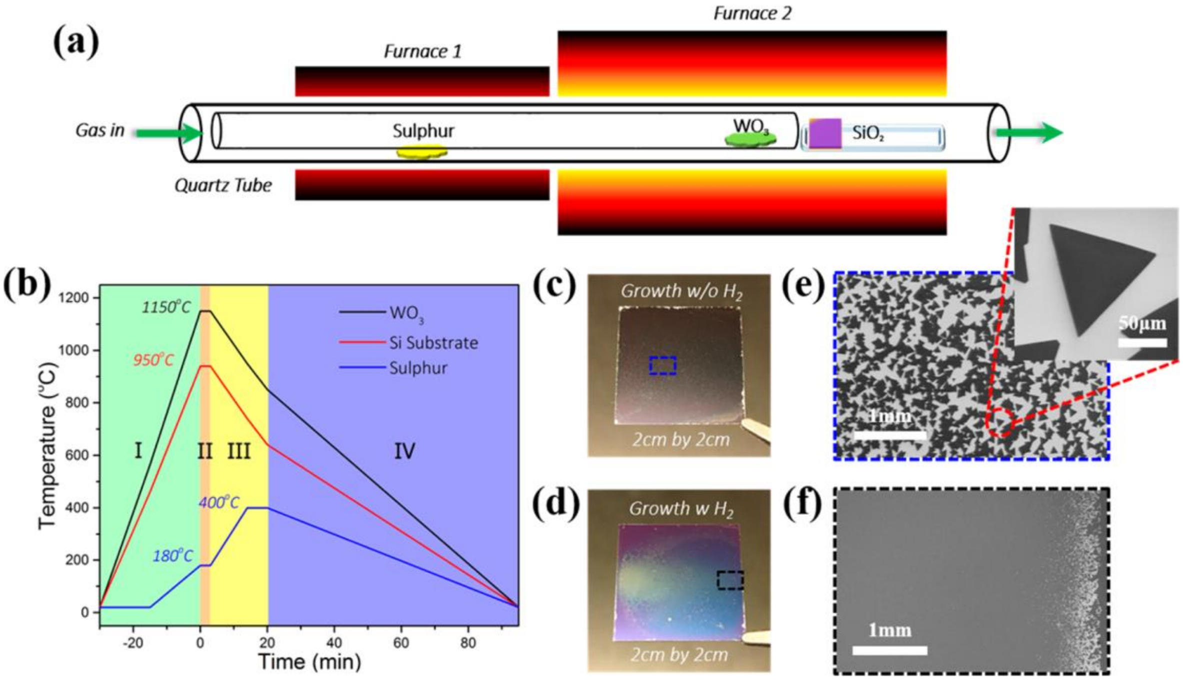

Figure 2.4 Atmospheric pressure CVD synthesis of large-area WS_2 films. (a) Schematic illustration of the CVD setup for the synthesis of WS_2. (b) Temperature profiles of the substrate, WO_3, and S. (c, d) Photos showing contrast difference between 2 cm × 2 cm SiO_2/Si substrates after CVD processes without and with H_2 addition. (e) SEM image of large triangular WS_2 crystals deposited on a SiO_2/Si substrate. (f) SEM image of a millimeter-sized WS_2 film on SiO_2/Si. Graphs and captions are modified from reference [57].

2.2.4 Sulfurization and selenization

Sulfurization and selenization are CVD-like technique to synthesize TMDCs. In a normal procedure, metal or metal oxide is deposited on the substrate and followed by annealing the sample in a sulfur-rich or selenium-rich environment at elevated temperature. The sulfur/selenium gas reacts with the precursor and converts it into 2DLM films.[1]. The method can be extended to produce heterostructures. Xue et al. fabricated a heterojunction of MoS_2 and WS_2 by a two-step sulfurization process. As shown in **Figure 2.5 A-C**, WO_3 films are predefined on SiO_2 surface by photolithography**.** Subsequently, the film is undergone first sulfurization to obtain WS_2 as shown in **Figure 2.5D**. The procedure is then repeated by depositing Mo film onto the WS_2. A heterostructure of MoS_2/WS_2 is obtained after the second sulfurization (**Figure 2.5E-G**). After the deposition of the gold electrodes, the heterostructure could be used as photodiodes (**Figure 2.5H,I**).[59]

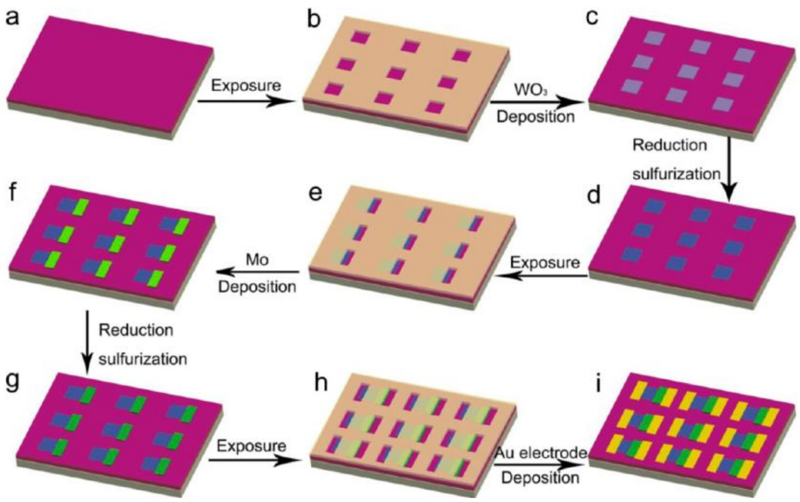

Figure 2.5 Schematic diagram of MoS_2/WS_2 vertical heterojunction preparation and corresponding devices fabrication. Graphs and captions are modified from reference [59].

Sulfurization or selenization process can synthesize vertically aligned TMDC films. Cui *et al.* demonstrated vertically aligned MoS_2 and $MoSe_2$ films.[13] Regardless of the choice of substrate, the in-plane direction of the film grows nearly perpendicular to the substrate surface. TEM image confirms the vertical alignment of the resultant film, as shown in **Figure 2.6**. Such a morphology with densely exposed edges is favorable for HER.

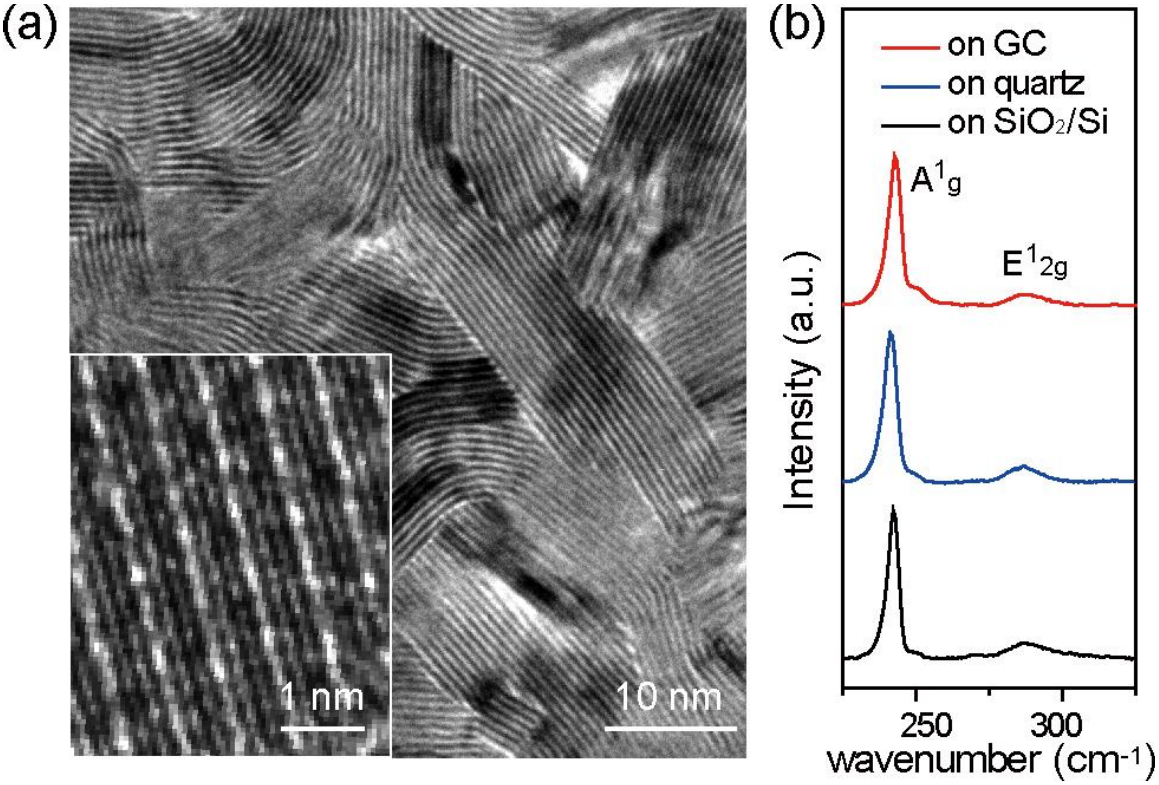

Figure 2.6 (a) TEM image of a vertically aligned $MoSe_2$ film produced by rapid selenization showing exposed edges. (b) Raman spectra from edge-terminated $MoSe_2$ films grown on glassy carbon (GC), quartz, and oxidized silicon (300 nm SiO_2/Si) substrates, respectively. Graphs and captions are modified from reference [13].

2.3 2DLM based Photodetectors

Photodetector converts absorbed light energy into electrical signal such as current or voltage. **Figure 2.7** shows a conventional phototransistor using 2DLM as a channel material. The light sensing mechanisms of 2DLM phototransistor such as photoconductive and photogating effect are discussed in this section.

Figure 2.7 Architecture of the conventional 2DLM phototransistor.

2.3.1 Parameters of photodetector

Responsivity (R)

The responsivity R is an indication of the available output photocurrent or photovoltage under certain wavelength and incident optical power of the photodetector. It is defined as the ratio of the photocurrent/photovoltage to the input optical power on the sensing region. In the mathematical form:

$$R = \frac{I_{ph}}{P_{in}} \qquad (1\text{-}1) \qquad \text{or} \qquad R = \frac{V_{ph}}{P_{in}} \qquad (1\text{-}2)$$

where I_{ph} is the photocurrent, V_{ph} is the photovoltage, and P_{in} is the input optical power.

Noise Equivalent Power (NEP)

The Noise Equivalent Power (NEP) is the minimum optical power required to achieve a signal to noise ratio of 1 in a 1 Hz bandwidth. In a practical calculation, it can be written as

$$\mathrm{NEP} = \frac{\mathrm{i}_{n,rms}}{R} \qquad (1\text{-}3)$$

where $i_{n,rms}$ is the mean-square noise current at the bandwidth of 1 Hz in darkness (unit: A $Hz^{-1/2}$). The noise level $i_{n,rms}$ is commonly found by the Fourier transform (FFT) of the measured dark current. Since 1/f noise is shown to be the most dominant noise source in 2DLM transistors,[21], [25] the corresponding NEP is commonly used for the 2DLM transistor.

Detectivity (D*):

The detectivity D* is a useful parameter for the detection and

$$\mathrm{D}^* = \frac{\sqrt{AB}}{NEP} = \frac{R\sqrt{AB}}{i_{n,rms}} \qquad (1\text{-}4)$$

where A is the effective illuminated area of the channel, B is the bandwidth, $i_{n,rms}$ is the root mean square value of the noise current and R is the responsivity of the device. D* can be viewed as the reciprocal of the NEP which is normalized by the square root of the sensing area and bandwidth. It reflects the ability of the photodetector after taking account of sensitivity, spectral response and noise of the device

2.3.2 Photoconductive effect

The photoconductive effect is originated by generating excessive charge carriers in the semiconducting 2DLM under light illumination.[1], [60] In a normal photoconductor, the 2DLM serves as the light sensing channel with drain/source electrode. Under the light illumination, the channel absorbs the photon energy which is greater than its bandgap. It generates an electron-hole-pair (EHP), which is also referred to photocarriers. When the concentration of the excessive charge carriers is increased, the conductivity increases. Under the V_{DS} bias, the photo-generated holes and electrons drift oppositely to the electrodes and increase the channel current, as shown in **Figure 2.8**. Under a given illuminated light intensity, the net increase of the channel current is the photocurrent. In most of the 2DLM-based phototransistors, their sensing mechanisms are mainly based on the photoconductive effect.[49], [60], [61]

Photocurrent produced by oppositely drifted photocarriers

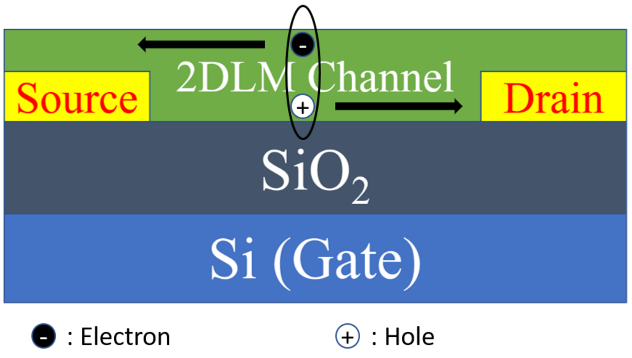

Figure 2.8 Illustration of photocurrent production in photoconductive effect.

2.3.3 Photogating effect

Photogating effect is regarded as a notable case of the photoconductive effect. Photocarriers are generated in a semiconductor when under light illumination. One kind of photocarriers (electrons or holes) is trapped in the localized states located at defects or surface absorbates, while the oppositely-charged carriers are transferred to the channel. The trapped carriers act as the local gate and provide an electrostatic field which modulate the channel conductance, while the oppositely-charged carriers will recirculate in the channel. (4,9) The multiple recirculation of photocarriers lead to very high photoconductive gain and hence the responsivity.

Photogating effect is pronounced in 2DLM based transistors since 2DLM exhibit large surface-to-volume ratio. Hence, forming heterostructure of 2DLM and other semiconducting nanomaterials (which provide localized states) can apply photogating effect to enhance the performance in photodetection, as shown in **Figure 2.9**. [21]–[23], [27], [62], [63] Compared to photoconductive effect, photogating effect usually leads to a higher gain and responsivity due to the extended life time of the trapped charge carriers. Consequently, the response and recover speeds of the transistor by photogating effect are usually slower than that by photoconductive effect.

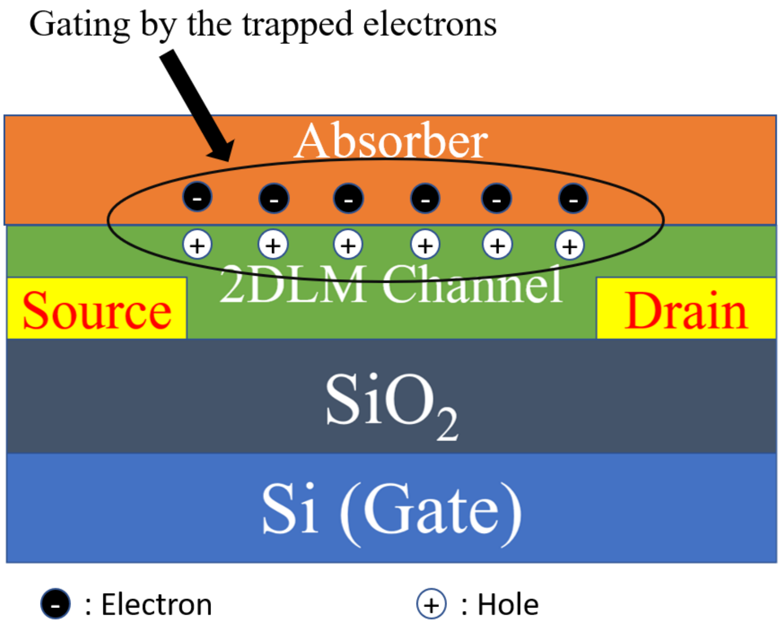

Figure 2.9 Illustration of gating produced by the trapped photocarriers in a heterostructure. Here electrons are trapped in the absorber and lead to photogating effect.

2.3.4 Phototransistors

In this section, selected 2DLM phototransistors are introduced.

Graphene phototransistors

Due to the zero bandgap and atomically thinness, pristine graphene transistors for photodetection showed a very low responsivity (<10 mA W^{-1}).[1], [64] Low optical absorbance and short photocarrier lifetime are the major drawbacks in photodetection. The experimental results showed the photoconductive effect in graphene transistors was inefficient for photodetection. However, fast response, high electron mobility and broadband detection still make graphene suitable for high frequency detection.[65]–[67] The high performance graphene phototransistor for photodetection could be achieved by applying photogating effect. Semiconducting NCs, organic semiconductors, perovskites have been employed as sensitizer in graphene transistor. [21]–[23], [27], [62], [63] After forming heterostructure with the graphene channel, the sensitizer can trap one kind of photocarriers and graphene can provide a high mobility channel to flow another kind of the photocarriers during photodetection. The photogating effect highly extends the lifetime of photocarriers and improve the responsivity of the graphene transistors to $10^7 – 10^9$ AW^{-1}. [21]–[23], [27], [62], [63] The photogating effect is an effective tactics to improve the responsivity of graphene phototransistors.

Black phosphorus (BP) phototransistors

Few-layer BP phototransistors were found to have high mobilities up to 1000 $cm^2\ V^{–1}s^{–1}$.[17] Unlike graphene, BP has a direct bandgap variation from 0.3 eV (bulk) to about 2 eV (1L).[16], [18] Wu *et al.* showed the responsivity of FL BP transistor can reach 9×10^4 A W^{-1} for near UV region (310 nm to 400 nm) while 1.82 A W^{-1} for visible – NIR region (400 – 950 nm).[49] The results suggest that BP is a potential candidate for photodetection with high mobility. However, few layers BP has a major drawback of environment-induced degradation and this hinders BP phototransistors for practical application.[68]

Transition metal dichalcogenide (TMDC) phototransistors

In addition to the aforementioned MoS_2 and WS_2, TMDC members such as $MoSe_2$, WSe_2, ReS_2, etc. have been explored for photodetection.[36], [61], [69]–[71] Due to the thickness dependent bandgap, conductance and absorption strength, [2] their performance in photodetection are dependent on the thickness. For instance, 1L MoS_2 detected only visible light but few layers MoS_2 can extend the detection range to NIR.[20], [72] The photodetection performance of the reported 2DLMs varied a lot even for the same material and same thickness. The responsivities of mechanically exfoliated 1L MoS_2 transistors are ranging from 7.5×10^{-3} A W^{-1} to 880 A W^{-1}.[19], [20] The responsivities of CVD grown 1L WSe_2 transistors are ranging from 1.1 A W^{-1} to 1.8×10^5 A W^{-1}.[11], [73] The huge variation may come from the synthesis method of TMDC and/or the fabrication of the phototransistors. Similar to the graphene transistors, the responsivity of TMDC transistor can also be improved by photogating effect. The semiconducting NCs, 2DLMs and organic semiconductors can act as sensitizers.[10], [74] **Table 2.1** summarizes the key photodetection parameters of the reported 2DLM transistors.

Table 2.1 Performance of photoconductors/phototransistors based on 2DLMs (1L: 1 layer, 2L:2 layers, FL: few layers, CVD: chemical vapor deposition)

Active layer	Channel thickness	Spectral range	Responsivity (AW^{-1})	Response times (ms)	Reference
Graphene	Mechanically exfoliated 2L	Visible-IR	~ 6.1×10^{-3}	/	[8]
Graphene + PbS QDs	Mechanically exfoliated 2L	Visible-NIR	10^7	100	[22]
Graphene + $CsPbBr_{3-x}I_x$ NCs	Mechanically exfoliated 2L	Visible-	~10^8	810	[23]
Graphene + Si QDs	CVD	UV-to-MIR	~10^9	3400−9000	[21]
BP	Mechanically exfoliated FL	Visible-NIR	4.8×10^{-3}	1	[18]
BP	Mechanically exfoliated FL	UV-visible-NIR	9×10^4	>10^5	[49]
MoS_2	Mechanically exfoliated 1L	Visible	7.5×10^{-3}	50	[19]
MoS_2	Mechanically exfoliated 1L	Visible	880	600	[20]

MoS_2	CVD-grown 1L	Visible	1.1×10^{-3}	$>10^3$	[75]
MoS_2 + PbS QD	Mechanically exfoliated 2L	Visible- NIR	6×10^5	350	[10]
WS_2	CVD-grown FL	Visible	9.2×10^{-5}	5.3	[76]
WS_2	CVD-grown 1L	Visible	1.88×10^{-2}	$<10^3$	[77]
WS_2 + PbS QD	CVD-grown 1L	NIR	14	0.6	[78]
$MoSe_2$	CVD-grown 1L	Visible	2.15×10^{-4}	25	[79]
$MoSe_2$	CVD-grown FL	Visible	93.7	400	[69]
WSe_2	Mechanically exfoliated 3L	Visible	7	1×10^{-2}	[80]
WSe_2	CVD-grown 1L	Visible- NIR	1.8×10^5	$>5 \times 10^3$	[11]
$ReSe_2$	Mechanically exfoliated 1L	Visible	95	68	[81]
ReS_2	CVD-grown 2L	Visible	604	2	[82]
SnS_2	CVD-grown FL	Visible	8.8×10^{-3}	5×10^{-3}	[83]
SnS_2	CVD-grown FL	Visible	100	22	[34]
SnS_2 + PbS QD	Mechanically exfoliated 5L	Visible- NIR	$1\text{x}10^6$	160-420	[84]

2.4 Hydrogen Evolution Reaction

For the future energy sustainability, hydrogen gas (H_2) is one of the clean and renewable energy sources. The electrocatalytic HER from water splitting is one of the most efficient methods to produce H_2 gas.[85] When choosing a semiconducting electrode for HER, the band position of the electrode should match the redox potential of the water for efficient electron transfer between the solution and electrode. Many TMDCs exhibit layer dependent band structure. Their conduction and valence band positions can be engineered to match the redox potential of water. Moreover, the unsaturated sulfur atoms of TMDC are beneficial to produce hydrogen gas.[47] More improvement are needed for TMDCs to improve the HER performance toward the conventional metal catalysts. In addition to the semiconducting members, some TMDC members are semimetals and may behave like the metal electrodes in HER. However, the cost of TMDC electrodes are usually cheaper than the conventional metal catalysts. Hence, TMDC electrodes for HER have attracted a lot of attention.

2.4.1 Mechanism

The mechanism of the HER is followed the Volmer – Heyrovsky mechanism:[46]

$H_3O^+ (aq) + e^- + * \rightleftharpoons H^* + H_2O\ (1)$, Volmer reaction (acidic)

$H_2O\ (1) + e^- + * \rightleftharpoons H^* + OH^- (aq)$, Volmer reaction (alkaline)

$H^* + H_3O^+ (aq) + e^- \rightleftharpoons H_2 (g) + H_2O\ (1) + *$, Heyrovsky reaction (acidic)

$H^* + H_2O\ (1) + e^- \rightleftharpoons H_2 (g) + OH^- (aq) + *$, Heyrovsky reaction (alkaline)

Or the Volmer-Tafel mechanism: [46]

H_3O^+ (aq) + e^- + * ⇌ H* + H_2O (1), Volmer reaction (acidic)

H_2O (1)+ e^- + *⇌ H* + OH^- (aq), Volmer reaction (alkaline)

H* + H*⇌ H_2 (g) + 2*, Tafel reaction (acidic and alkaline)

where * and H* indicate an empty active site and a hydrogen atom bound to an active site, respectively. Both mechanisms indicate the binding of the hydrogen atoms to an active site * on the catalyst/electrode surface is the main parameter for HER.

As proposed by the Volmer reaction, the electrons supplied by the electrode electrolyze the molecules in either acidic or alkaline solution. Then hydrogen is produced and bind to the empty active sites on the electrode. Even the following processes proposed from Tafel reaction and Heyrovsky reaction are different, the bound hydrogen atoms are reacted to other hydrogen or hydrogen-contained molecules to produce hydrogen gas at the active sites. The produced hydrogen gas is collected.

2.4.2 Parameters in HER

The parameters of HER is introduced. During the catalysis process, the electrons is supplied to the bound hydrogen atoms on the electrode. The catalyst activity can be analyzed by the linear scanning voltammetry (LSV) (or called “polarization curve”) in an electrochemical system. **Figure 2.10A** shows the typical polarization curve in HER activity. Parameters can be deduced from the polarization curve to evaluate the performance. The cathodic current and the potential in the polarization curve can be simplified to the Tafel equation:[46]

$$\mathrm{j} = -j_0 e^{-\frac{\eta}{b}}$$

and hence $$\eta = \mathrm{b}\ln(\mathrm{j}_0) - \mathrm{b}\ln(-j)$$

where j is the current density, j_0 is the exchange current density, b is the Tafel slope and η is the overpotential. In the equation, j has the negative value in the polarization curve and b $\ln(j_0)$ is a constant.

For simplicity, in some literature the authors write the equation as:

$$\eta = \mathrm{b}\log(j) + a$$

In this revised equation, the Tafel slope b becomes a negative value with a unit mV/dec, j is the absolute value of the current density and a is a constant. For a good catalyst, it should have a low Tafel slope and a large exchange current density.

Exchange current density j_0

It can be viewed as a measure of electron transfer rate of the electrode. The higher the current density, the higher the electron transfer rate. Hence the rate of reduction of hydrogen atoms is improved.

Tafel slope b

Tafel slope represents the change of potential per decade of current in logarithm scale. If the slope is too large, the electrode needs significant potential change to produce desired current. The slope is highly dependent on the materials properties of the catalyst and the electrochemical circuit. Besides the band structure, active site density, conductivity and preparation of the catalyst, the employed electrolyte also affects the Tafel slope.

Overpotential η

Overpotential is an excessive potential applied shown at the polarization curve. Usually, the potential where the HER activity commenced is called onset potential. The smaller onset potential is favorable for the optimal catalyst since a smaller energy is needed to start the HER.

Turnover Frequency (TOF)

TOF is the total number of moles transformed into the desired product by one mole of active site in a given time. The larger TOF indicates the better activity of the catalyst.

2.4.3 HER activity of 2DLM electrodes

Jaramillo *et al.* investigated the relationship between the edge length and exchange current density. They explored the HER activities of the triangular MoS_2 NCs with different areas. According to their result, the exchange current density showed linear dependence on the MoS_2 edge length but did not correlate with the area of the MoS_2 crystal.[47] The results indicated the unsaturated sulfur atoms are the active sites of the TMDC. Hence, it is evidenced that engineering the density of the active site of the TMDC catalysts is able to improve the HER performance of the TMDC electrodes. Among their tested samples, the Tafel slopes are 55 to 60 mV/decade and exchange current densities are about 1.3×10^{-7} to 3.1×10^{-7} A cm^{-2}

Since vertically aligned TMDC electrodes can expose the edges as much as possible, they were tactically synthesized and studied for HER. For instance, Tour *et al.* synthesized the vertically aligned porous WS_2 by the sulfurization of the porous WO_3 film. The vertically aligned porous WS_2 shows a higher catalytic current, lower onset overpotential and small Tafel slope than the pristine WS_2, as shown in **Figure 2.10**.[45] The results experimentally showed the enhancement in HER is attributed to the unsaturated active sites on the edges of WS_2. Hence the strategies of synthesizing vertically aligned TMDCs are being researched for HER.

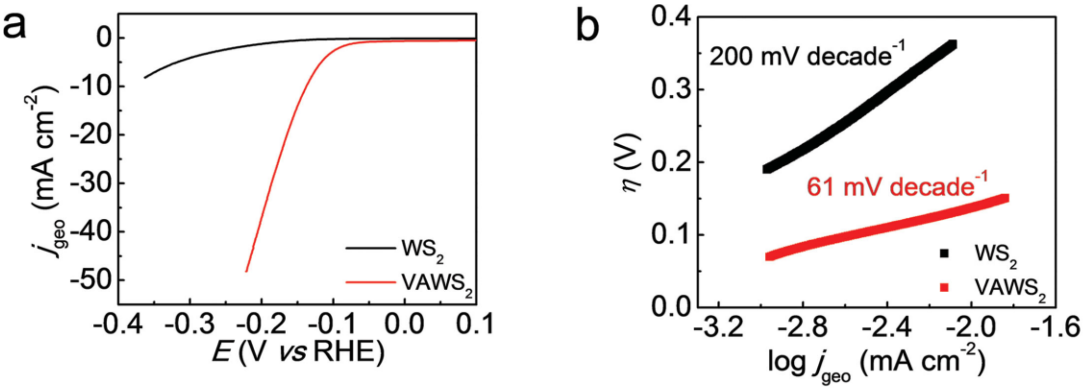

Figure 2.10 Electrochemical HER activity of the $VAWS_2$ film. a,b) Linear sweep voltammetry (LSV) curves measured at 5 mV s^{-1} in 0.5 M H_2SO_4 aqueous solution and corresponding Tafel slopes. Graphs and captions are adopted from reference (45).

Cui *et al.* also reported the large area vertically aligned MoS_2 and $MoSe_2$ synthesized by facile sulfurization and selenization process.[13] The films exposed a high density of vertically aligned MoS_2/$MoSe_2$ region and were tested for HER. In the HER measurement, the TMDC electrodes exhibited the exchange current densities about 10^{-6} A cm^{-2}, which are much greater than the MoS_2 electrodes.[47] The current densities are comparable to the common metal catalyst.[86] However, the Tafel slopes of their samples are in the range of 105−120 mV/decade. In this aspect, improvement is required since the planar MoS_2 showed the Tafel slopes of 55 to 60 mV.[47] This work showed a relatively facile approach to synthesize vertically aligned TMDC with large area and improved HER performance.

Chapter 3 Experimental and characterization Techniques

In this chapter, the synthesis of materials, fabrication of devices and characterization methods are introduced.

3.1 Synthesis of materials

3.1.1 CVD graphene

Graphene was grown on a 2-inch copper foil (Alfa Aesar, 0.025mm thick) in a plasma enhanced chemical vapor deposition (PECVD) chamber (Aixtron CVD). The procedure of the graphene growth is as follow: the Cu foil was annealed from room temperature to 1020°C in a Ar/H_2 mixture gas (Ar: 250 sccm, Ar/H_2: 1000 sccm) at constant pressure of 25 mbar. After 1020°C was reached, the methane gas (15 sccm) was injected into the chamber. Thetime for the graphene growth was 5 minutes. Finally, the sample was cooled down to 150 °C under Ar gas flow and could be taken out. The graphene was optically and electrically characterized by Raman spectrometer and graphene field effect transistor respectively.

3.1.2 $AgBiS_2$ NCs

In a typical synthesis, a flask containing 10 mL oleic acid (OA) or octanoic acid (OctA), 0.1 mmol $AgNO_3$ and 0.1 mmol $Bi(NO_3)_3 \cdot 5H_2O$ were heated (120 °C) and stirred by a heating mantle under ambient environment. Then 0.1 mmol sulfur powder was dissolved and stirred into a long chain length amine such as octylamine (OTA) or dodecylamine (DDA). After the dissolution of all the precursors, 1 mL Ag/Bi and 1 mL sulfur were mixed under vigorous stirring in room temperature and atmosphere. The color of the mixture turned black within seconds and the $AgBiS_2$ nanocrystals were formed. The $AgBiS_2$ nanocrystals were cleaned by precipitation/dispersion in a toluene/ethanol mixture via centrifugation. The $AgBiS_2$ NCs were dispersed in toluene again after cleaning by three times.

3.1.3 $PdSe_2$

Palladium (Pd) films on c-plane sapphire were prepared by DC magnetron sputtering system. The 99.95 % purity Pd sputtering target was loaded in the sputtering system. After the pressure reached to 1×10^{-6} Torr, argon gas was introduced and the pressure was kept to 5×10^{-3} Torr. During the Pd deposition, the sample holder was rotating slowly with a deposition power of 10 W. The deposition time was adjusted to control the Pd films' thickness and hence the thickness of the $PdSe_2$ samples.

The samples were then placed inside a tube furnace and underwent selenization. The selenium powder was placed upstream and 15 cm apart from the samples. The Argon flow was 90 sccm and the pressure was kept at 5 Torr. The temperature of the Pd and Se powder were 350 ^{o}C and 300 ^{o}C respectively during selenization.

3.1.4 Vertically aligned $PtSe_2$

Pt sputter target (99.99% purity) was purchased from Kurt J Lesker. Pt films with different thicknesses were firstly deposited on fluorine – doped tin oxide (FTO) and SiO_2/Si substrates using a sputtering system. Then the Pt samples were loaded into a tube furnace and placed at the center of the quartz tube and heated to 420 °C. The Se source was placed away from the Pt films with a distance of 10–15 cm. Argon gas with a flow rate of 40 sccm, was used to transport the vaporized Se to the Pt films. Prior to the heating process, argon gas with a flow rate of 300 sccm was purged the system for 20 min. Then a selenization time of 90 minutes was used to ensure complete selenization.

3.2 Characterization methods

3.2.1 Raman spectroscopy

Raman spectroscopy is a fast and non-destructive characterization technique which has been extensively used to characterize 2DLMs. In a typical measurement, an intense, monochromatic laser is focused on the sample and the molecules are excited to a virtual state. Then the excited molecules relax by releasing the photons with specific energies and stay in a lower energy level. The wavelength and intensity of the scattered lights are recorded and used for the calculation of the Raman shift.[87]

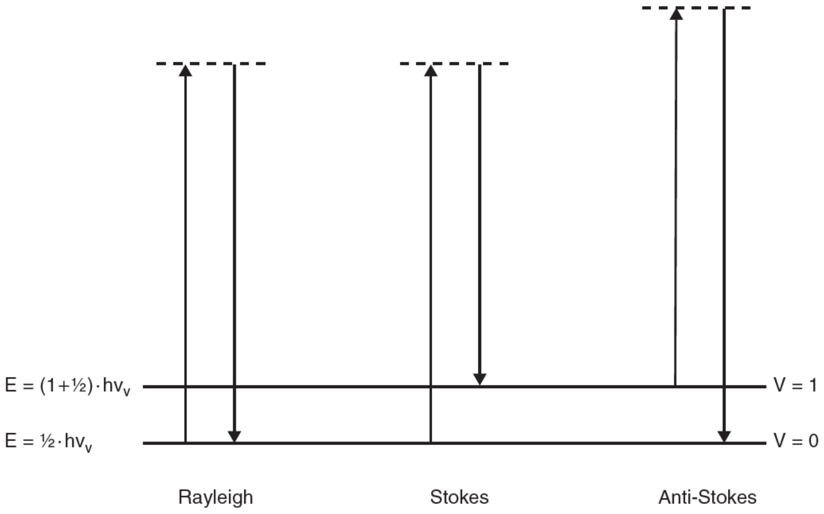

Figure 3.1 Idealized model for the dispersion of light by molecules. Graphs and captions are adopted from reference [87].

The difference in frequency between the scattered light and the incident light, or called

Raman shift, is usually presented in wavenumber with the unit cm^{-1}, which is related by the equation:

$$\omega = (\nu_{scattered} - \nu_{incident})/c$$

where $\nu_{\text{scattered}}$ and ν_{incident} are the frequencies of the scattered light and the incident light, respectively. c is speed of light and ω is the wavenumber in cm^{-1}. If the Raman shift is equal to zero, it is called Rayleigh scattering. Otherwise, Stokes and anti-Stokes scattering are named for the Raman shift when the shift is negative and positive, respectively. Since different materials have different phonon modes as well as the Raman shift, which could be used to characterize the tested sample.

Raman scattering of the samples were collected by LabRAM HR 800 Raman Spectrometer. A laser source with a wavelength of 488 nm was served as the incident wavelength.

3.2.2 X-ray diffraction (XRD)

As another non-destructive characterization technique, X-ray diffraction (XRD) provides the crystal structure information of the materials. Typically, parallel X-ray beam is illuminated on the target material and diffracted by the atoms (Figure 3.2). The diffracted

X-ray will produce interference pattern which is dependent on the crystal structure of the target material. The constructive interference pattern of the diffracted X-ray satisfies the Bragg's law:

$$2\mathrm{d}_{hkl} sin\theta = n\lambda$$

where h, k, l are the Miller indices of the crystal plane, $\mathrm{d}_{\mathrm{hkl}}$ is the inter-planar spacing of the plane (hkl), a is the lattice constant, θ is the incident angle between the plane and the X-ray, n is integer and λ is the wavelength of the X-ray.

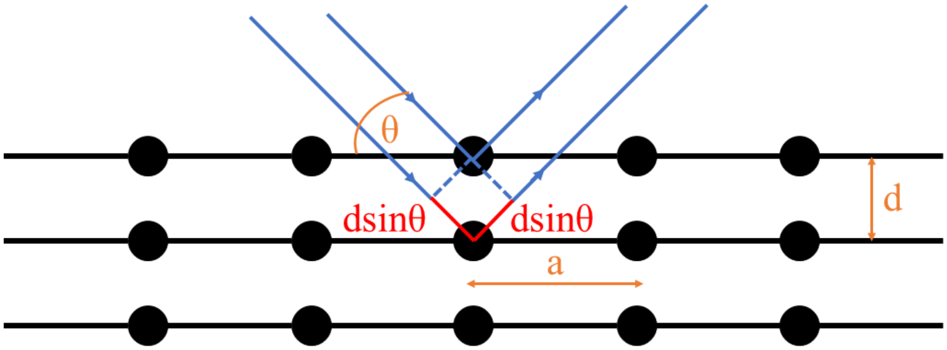

Figure. 3.2 Schematic diagram showing the diffraction of x-ray in target material during XRD measurement.

Depended on the crystal structure of the materials, there are equations to obtain the inter-planar spacing d by knowing Miller indices (h, k, l) and the lattice constant a. For instance, the equation for obtaining the inter-planar spacing in cubic structure materials is $\mathrm{d}_{hkl} = \frac{a}{\sqrt{h^2+k^2+l^2}}$. Hence one can deduce the Miller indices of the XRD peaks, crystal structure of the tested material by the obtained XRD pattern. The powder diffraction files of different materials can be found in some databases. The XRD pattern was obtained by X-ray Diffractometer (Rigaku SmartLab). A wavelength of 1.54 Å (K_α radiation of copper) was used as the X-ray probe.

3.2.3 Transmission electron microscopy (TEM)

Transmission electron microscopy (TEM) is an inevitable instrument for nano-science. There are some compulsory components, such as electron gun, objective lens, condenser lens and electron detectors. Generally, the electron beam is generated by the electron gun and pass through the electromagnetic lens to become parallel beam. The electron wavelength is smaller than the spacing between the atoms. So the beam penetrates the sample and reach the detector so that the images can be obtained. As a high resolution and magnification electron microscope, it can obtain the size, continuity, atomic plane separation and thickness information of the measured nanomaterials.

Further supplementary parts such as selected area electron diffraction (SAED) and energy-dispersive X-ray spectroscopy (EDX) can be installed in the TEM system to study the crystal structure and composition of the specimen. Some TEM can be operated in scanning mode called STEM. The mode can scan the selected area in nanoscale. The details of the atomic arrangement or distribution can be investigated.

Field Emission Electron Microscope STEM (JEOL Model JEM-2100F) equipped with SAED and EDX was employed to study the crystallography, composition and morphology of the samples. Carbon coated copper grid served as the sample holder for the TEM measurement.

3.2.4 Selected area electron diffraction (SAED)

During TEM measurement, the electron wavelength is smaller than the spacing of atoms, so the atoms can serve as the diffraction grating to the electrons which is similar to the principle of having XRD pattern. The crystal structure of the samples will scatter part of the electron beam in particular angles, which is beneficial to determine the crystallinity and crystal structure of the selected zone. The dot pattern and ring patterns represent the single crystalline and polycrystalline materials, respectively. For crystalline materials, the crystal plane and structure can be deduced by the dot pattern obtained in SAED.

3.2.5 Energy-dispersive X-ray spectroscopy (EDX)

Energy-dispersive X-ray spectroscopy (EDX) is a technique to obtain the atomic ratio of the measured sample. In the electron microscopy measurement, high energy electron beam may also excited the electrons to higher energy level which are originally in the inner shell of the atoms. When the electrons of the atoms refill the holes of inner shell, X-ray are released. The X-ray spectrum is element dependent. X-ray detector and analyzer collect and analyze the X-ray spectrum so that the atomic ratio of the composition can be obtained. Figure 3.3 describes the principle of EDX. In STEM mode, an EDX mapping can be done to analyze the atomic distribution in the selected region.

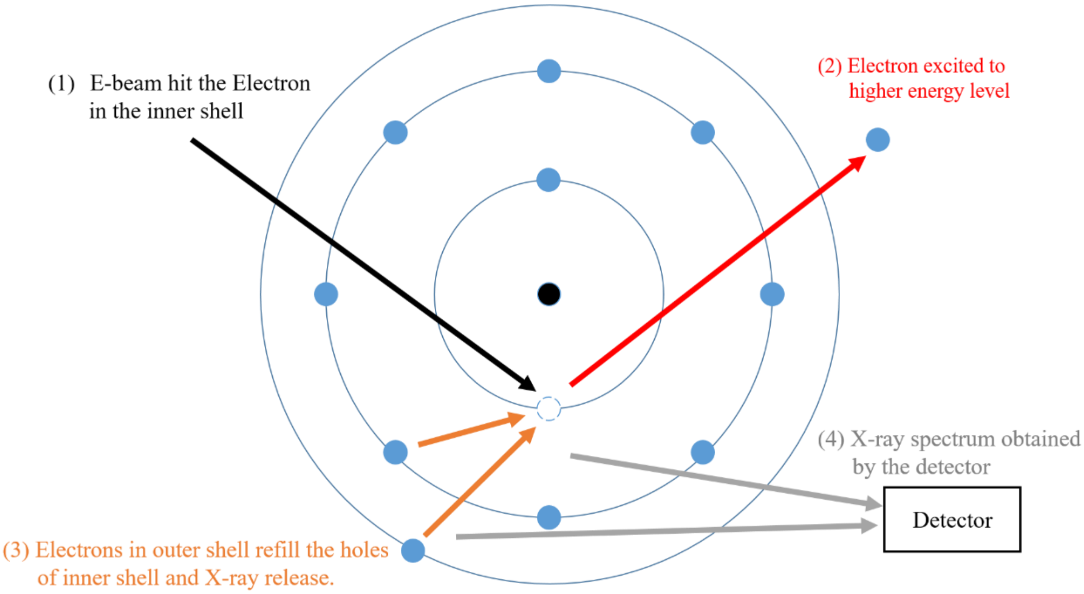

Figure 3.3 Principle of EDX.

3.2.6 Fourier Transform Infrared (FTIR) spectroscopy

Fourier Transform Infrared (FTIR) spectroscopy is one of the common techniques which can obtain the natural vibration frequency of the chemical bonding in solid, liquid and gas. The bonds of the ligands or dopants can be detected by this technique. The FTIR transmittance spectra of the NCs films before and after ligand exchange were obtained by the Bruker Vertex-70 FTIR.

3.2.7 UV-Vis-NIR spectrometer

The absorption spectrum of the nanomaterials is of importance for optoelectronic application. In a typical experiment, two rays of light pass through the reference material and the sample. The light received by the detector will then be analyzed. The absorbance of the sample under different wavelengths is then calculated and the absorption spectrum of the sample is obtained. The setup is briefly presented in Figure 3.4. UV-vis-NIR spectrometer (Perkin Elmer) was used for absorption measurement.

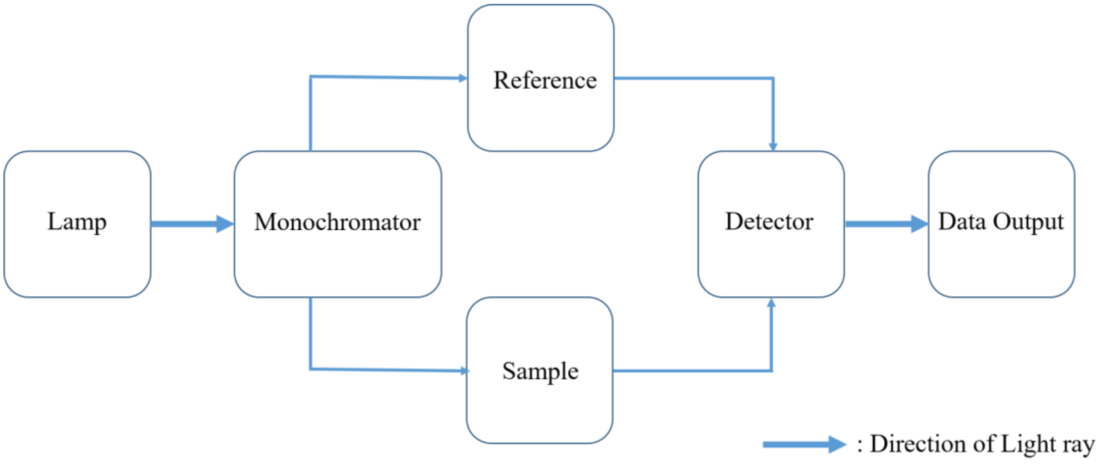

Figure. 3.4 Schematic diagram of set up showing a double beam UV–visible spectrophotometer.

3.2.8 Atomic force microscopy (AFM)

In the typical atomic force microscopy (AFM) measurement, the sample is on the piezoelectric stage and probed by a flexible cantilever with a very sharp tip. As a non-destructive measurement for the thickness, tapping mode is usually employed. The tip scans the surface and oscillate up-and-down near the sample surface and receive a repulsive interatomic force when the tip is close to the surface atoms. The cantilever will deflect away from the surface if it is too close. The whole process is monitored by a laser beam which is directed on the cantilever (back side of the tip) and reflected to the photodiode array. The light signal from deflection of the cantilever is then received and the surface details such as roughness and thickness are analyzed by the computer. An AFM (Asylum MFP-3D Infinity) was used to measure the thickness of the PdSe2 and $PtSe_2$ films.

3.2.9 X-ray photoelectron spectroscopy (XPS)

X-ray photoelectron spectroscopy (XPS) is a quantitative technique to measure the elemental composition, chemical state and electronic state of the elements of a material. In a typical measurement, an X-rays beam is illuminated the sample. Then the number and the kinetic energy of the escape electrons are measured simultaneously. The electron binding energy of the emitted electrons can be determined by using an equation.

$$E_b = E_{X\text{-ray}} - E_{KE} + \phi$$

where E_b is the binding energy of the electron, $E_{X\text{-ray}}$ is the photon energy of the X-ray, E_{KE} is the kinetic energy of the electron received in the measurement and ϕ is the work function depended on both the spectrometer and the material. Since each element has its own characteristic binding energy and electron configuration, the elements in the material can produce a characteristic set of XPS spectrum by their characteristic binding energies. These characteristic XPS spectrum can be employed to determine the composition of the specimen. The XPS (KRATOS Analytical, AXIS Ultra DLD) was employed to analyze the composition and electron state of the $PtSe_2$ films.

3.2.10 Electrical measurement of the 2DLM transistors

All the electrical measurements of the 2DLM-based transistors were conducted in a nitrogen filled glove box with O_2, $H_2O < 10$ ppm at room temperature. A source meter (Keithley 4200-SCS) was used to provide voltage and record the current. For photodetection, light emitting diodes (LEDs) with different emission wavelengths were used to illuminate the transistor channel. The photocurrents of the devices under various light intensities were recorded. The experimental setup is shown in Figure 3.5

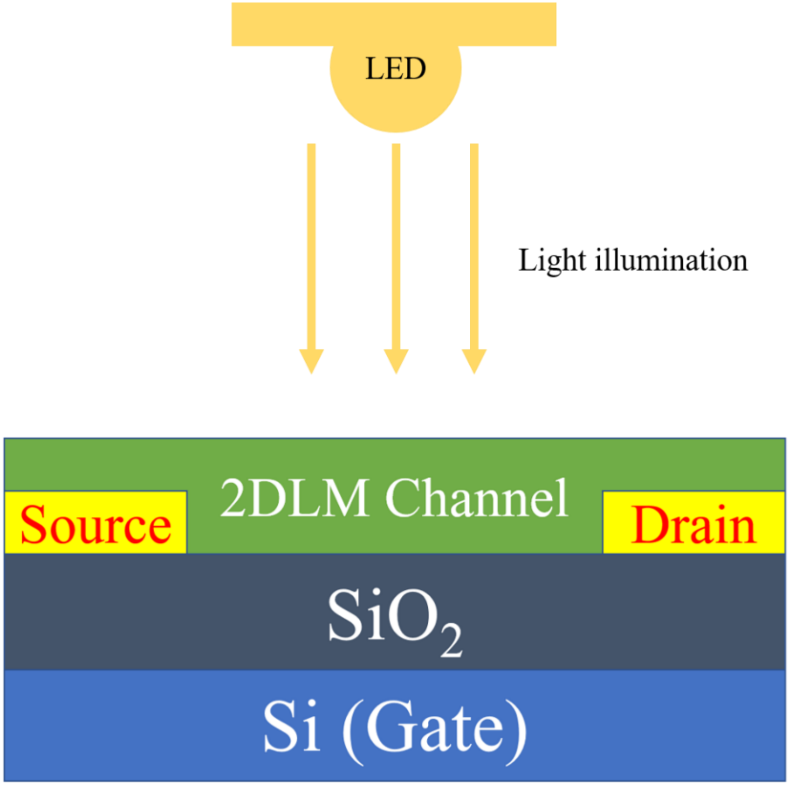

Figure. 3.5 Experimental setup of the electrical measurements.

3.2.11 HER measurement of the vertically aligned $PtSe_2$ film

The electrochemical measurements were carried out in a three-electrode system using a CHI 660E electrochemical workstation. The $PtSe_2$ films with different thicknesses (1.9 – 76 nm) were transferred onto glassy carbon (GC) disk electrodes which served as the working electrodes with a platinum (Pt) counter electrode and an Ag/AgCl (saturated KCl) reference electrode (Hach). All linear scanning voltammetry (LSV) and Tafel plots of the samples were conducted using a 0.5 M sulfuric acid (H_2SO_4) electrolyte prepared in Millipore water (18 MΩ cm). All potentials reported in this work were given with respect to the reversible hydrogen electrode (RHE), which were calibrated by the following equation: $E \text{ vs RHE} = E \text{ vs Ag / AgCl} + 0.059 \times pH + 0.199$ (V). Bare GC and Pt electrodes were also performed with the same measurement for comparison. The experimental setup is illustrated in Figure 3.6.

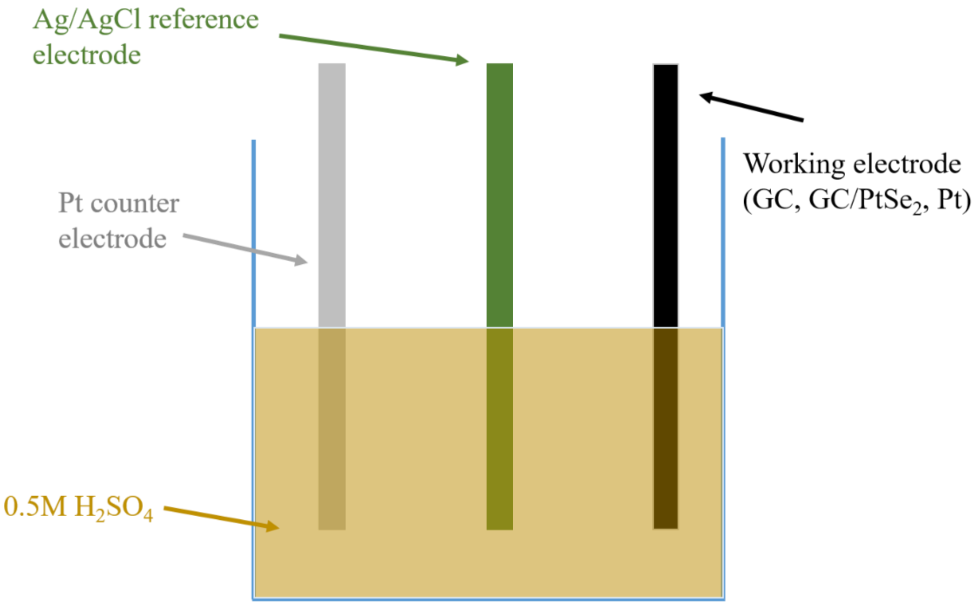

Figure. 3.6 The experimental setup of the electrochemical measurements.

Chapter 4 Graphene phototransistor with $AgBiS_2$ NCs

4.1 Introduction

As described in the chapter 2, graphene transistor can be sensitized by absorbers to improve its responsivity in photodetection. The photoresponsivities of PbS and $CsPbX_3$ based graphene transistors could reach 10^7 and 10^8 A W^{-1}, respectively. [22], [23] Recently another non-toxic Si NCs were hybridized with graphene and showed a photo-responsivity of 10^8 to 10^9A W^{-1} under 375 nm to 1870 nm light illumination. The devices also exhibited mid-infrared photo-responsivity of 0.22 – 44.9 A W^{-1} in 2.5 to 3.9 µm. [21] Both works evidence that graphene transistors with NCs is a promising approach for high performance photodetection devices.

During the past years, lead-based nanocrystals (NCs), such as lead sulphide (PbS), have been widely studied for solar cells and infrared (IR) detection.[10], [84], [88]–[90] Due to their high absorption coefficient and solution dispersibility, they have been employed to enhance the photodetection of the 2DLM transistors.[10], [22] However, the toxicity of lead causes long-term environmental and biological issues,[91] which limits its applications. $AgBiS_2$, a non-toxic and high stability material, has been employed to the active material for solar cells showing a power conversion efficiency of 6.3%.[24] The work was recognized as the first demonstration of efficient inorganic nanocrystal-based solar cells which simultaneously fulfilled the advantages of non-toxicity, abundance, low-temperature and solution processability. Although the $AgBiS_2$ NCs exhibited a high infrared external quantum efficiency in the aforementioned solar cells with a bandgap fall in the infrared region (1.0 – 1.25 eV),[24], [92] the investigation of its IR detection is scarce.

Herein we present a facile synthetic route for $AgBiS_2$ NCs with a much shorter processing time under ambient conditions as compared to the conventional hot injection method.[24] The $AgBiS_2$ NC solution was spincoated onto a graphene transistor for 895 nm light detection. A high photo-responsivity of 1.24×10^5 A W^{-1} was achieved by a small operation voltage of $V_{DS} = 0.1$ V. Our findings demonstrate that the $AgBiS_2$ NCs can be synthesized by a facile technique for optoelectronic application. A high responsivity, non-toxic graphene phototransistor for IR detection without complicated procedures is successfully fabricated.

4.2 Chemicals and Reagents

Oleic acid (OA), Octanoic acid (OctA), octylamine (OTA), dodecylamine (DDA), Tetrabutylammonium iodide (TBAI) and sulfur powder were purchased from Sigma Aldrich. Silver Nitride ($AgNO_3$) and bismuth (III) nitrate pentahydrate ($Bi(NO_3)_3 \cdot 5H_2O$) were purchased from Aladdin. Toluene, methanol and ethanol were ACS reagent grade. All chemicals were used without any purification.

4.3 Results and discussion

4.3.1 Basic characterization of $AgBiS_2$ NCs

In a typical synthesis, 0.1 mM Ag/Bi oleate solution and 0.2 mM sulfur amine solution were mixed under rigorous stirring, resulting to a black solution. Fig. 1A shows the photograph of the three solutions and revealing their colours. Besides the OA and DDA ligand pair used, two other pairs namely OA and OTA, OctA and OTA, were also employed to fabricate the NCs with similar result. Detailed synthesis information is described in the Section 3.1.2.

Figure 4.1 Photograph of the Ag/Bi-oleate, sulfur in amine and the $AgBiS_2$ NCs.

TEM was used to characterize the size distribution and crystal structure of the NCs produced by the OA/DDA ligand. The size distribution of the NCs is ranging from 7 to 15 nm with the most frequent size at around 8 nm, as shown in **Figure 4.2C**. TEM image and SAED pattern in **Figure 4.2A** depict that the NCs are having a cubic structure. SAED pattern shows clear rings of the (111), (200), and (220) crystal planes. **Figure 4.2B** shows the high resolution TEM image of a single NC revealing the interplanar distance of 0.32 nm for the atomic plane of (111). Similar characterization results were obtained when the ligand pairs changed to OA/OTA and OctA/OTA (**Figure 4.3 D-F** and **G-I**). The result indicates that the choice of the ligand – pair is independent on the synthesis process.

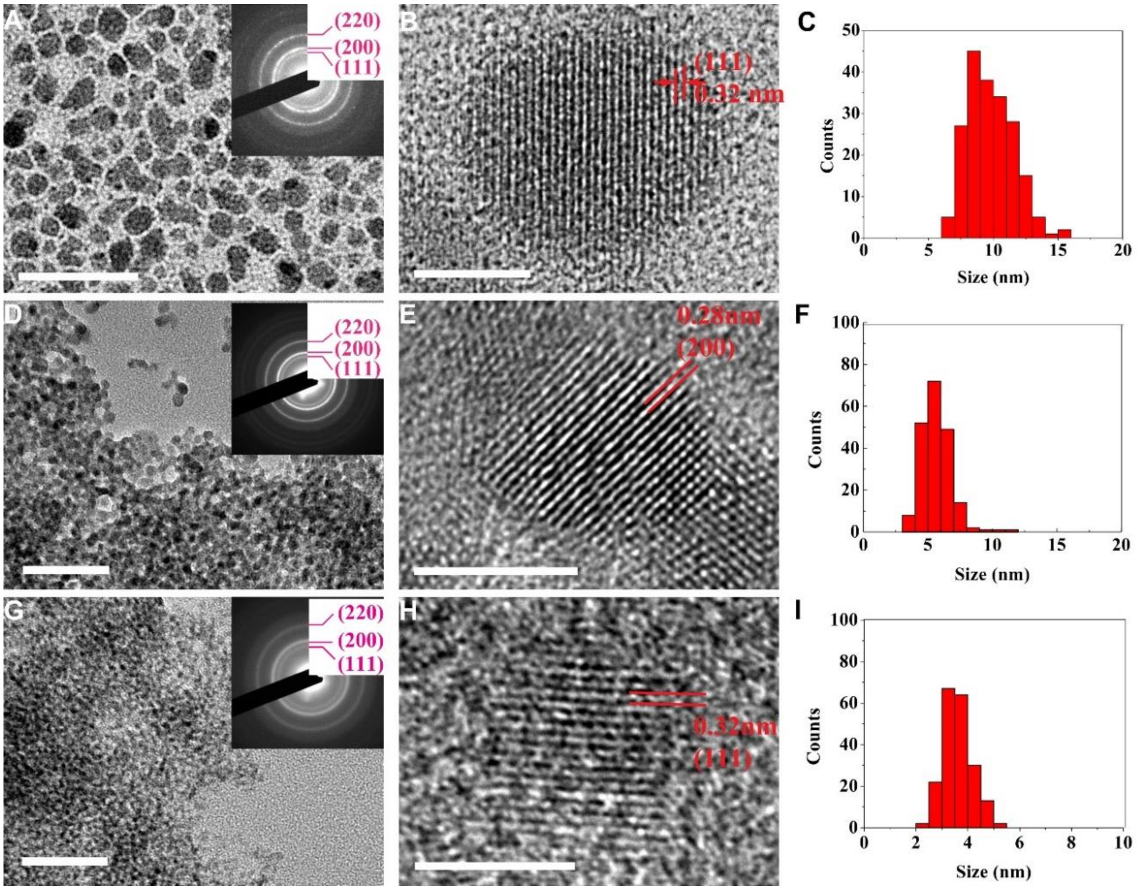

Figure 4.2 TEM characterizations of $AgBiS_2$ NCs synthesized by OA/DDA (A-C), OA/OTA (D-F) and OctA/OTA (G-I). A,D,G) TEM images of the $AgBiS_2$ NCs. Scale bar is 50 nm. Inset: SAED pattern. B,E,H) High resolution TEM images of a single $AgBiS_2$ NC. Scale bar is 5 nm. C,F,I). Size distribution profile of the $AgBiS_2$ NCs.

XRD and EDX measurements were applied to further analyze the $AgBiS_2$ NCs. The XRD pattern for the NCs and the reference pattern (Black lines, PDF#21-1178) are shown in **Figure 4.3**. The XRD pattern reveals the major peaks corresponding to the plane (111), (200), and (220) of $AgBiS_2$, which is in good agreement with the SAED pattern of the sample. The composition of the product was analyzed by EDX. The uncertainty of the EDX measurement is less than 10% and the obtained atomic ratio are shown in **Figure 4.4**. The result reveals that the atomic ratio of Ag/Bi/S is very close to 1 : 1 : 2 and no oxygen is detected.

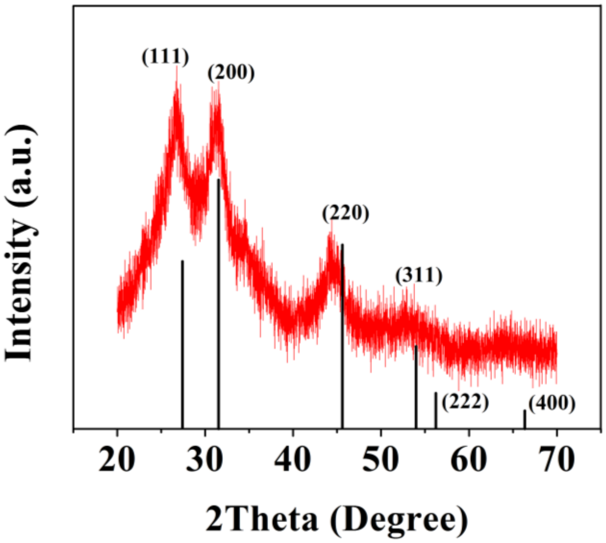

Figure 4.3 XRD pattern of the AgBiS$_2$ NCs, reference pattern for cubic AgBiS$_2$

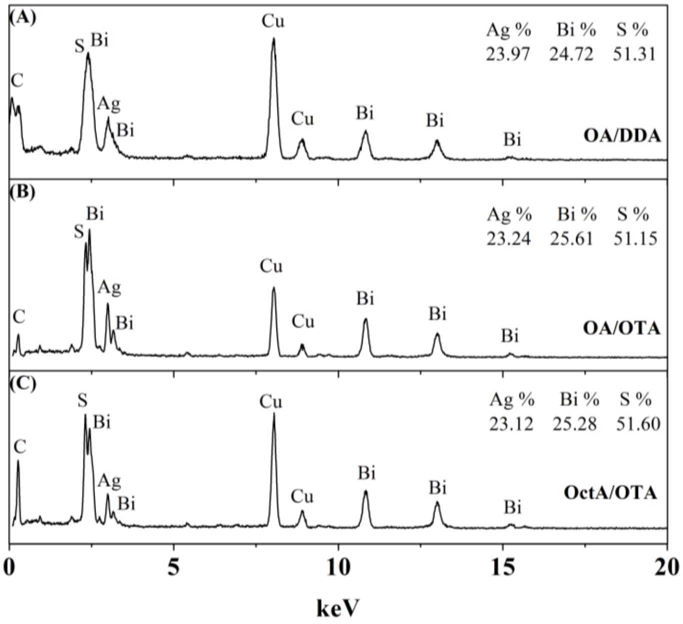

Figure 4.4 Detailed EDX spectra of the AgBiS$_2$ NCs grown by using A) OA/DDA, B) OA/OTA, C) OctA/OTA.

Cubic $AgBiS_2$ was reported to have the bandgap of about 0.8 eV in the bulk form and about 1.0–1.25 eV in the nanocrystalline form.[24], [92] **Figure 4.5A** shows the absorption spectrum of the NCs in toluene, revealing a broad absorption covering 400 nm to 1000 nm. It is noteworthy that the long aliphatic chain molecule ligands such as OA/DDA are insulating which inhibits the charge transfer through the NCs to the surrounding.[93], [94] Therefore, the surface ligand exchange was changed to iodide ligand to enhance the surface's conductivity. Fourier-transform infrared spectroscopy (FTIR) was measured on the samples before and after the ligand exchange. **Figure 4.5B** shows the transmittance spectra of the $AgBiS_2$ NCs on a quartz substrate before and after the ligand exchange. The C–H vibrations (2922 cm^{-1} and 2852 cm^{-1}) are nearly disappeared after the ligand exchange, which implies the removal of the long aliphatic chain ligand OA/DDA from the NCs surface.[90], [95]

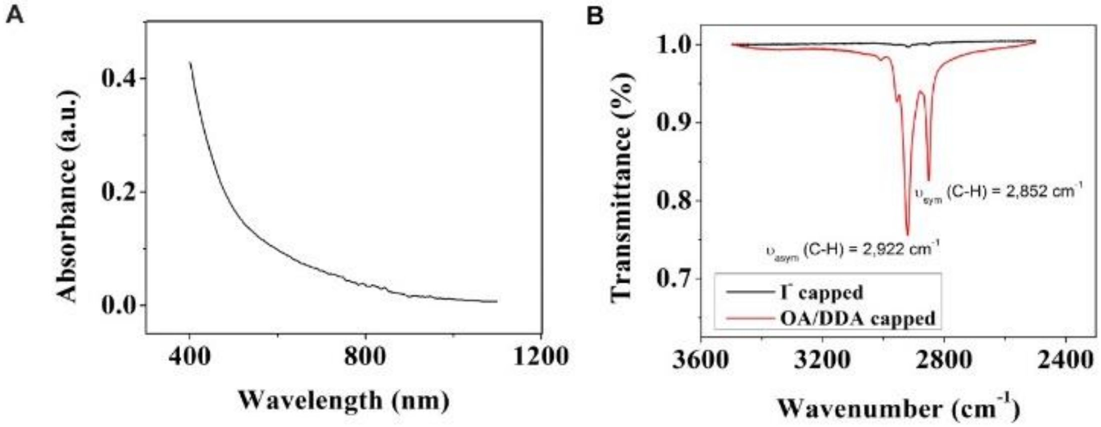

Figure 4.5 (A) UV-vis absorption spectrum of $AgBiS_2$ NCs in toluene. (B) The FTIR spectra of the films before (OA/DDA capped) and after (I^- capped) solid state ligand exchange.

4.3.2 Fabrication and characterization of graphene transistor

The monolayer graphene was prepared by CVD method and characterized by Raman scattering. No defect peak is observed as shown in **Figure 4.6A**. To fabricate the graphene transistor, Cr/Au metal electrodes were patterned on Si/SiO_2 substrate (SiO_2, 300 nm thick) by photolithography. A thin layer of poly(methyl methacrylate) (PMMA) was spun-coated on top of graphene/copper foil and heated at 150 ^{o}C for 30 minutes. Then the PMMA/graphene/copper composite was let to float on ammonium persulfate solution with concentration 2g/60 mL. After the copper foil was completely etched, the PMMA/graphene composite was cleaned with DI water for two times and transferred onto the patterned Cr/Au electrodes and dried at 120 ^{o}C for 30 minutes. Finally, the samples were immersed into acetone for 6 hours to remove PMMA. Under an applied voltage of 0.1 V across the drain and source electrodes (i.e. V_{DS} = 0.1 V), the intrinsic transfer characteristic curve of the graphene transistor from -80 V to 80 V was characterized (**Figure 4.6B**). The Dirac point is located at 5 V which indicates a slight p-type characteristic.

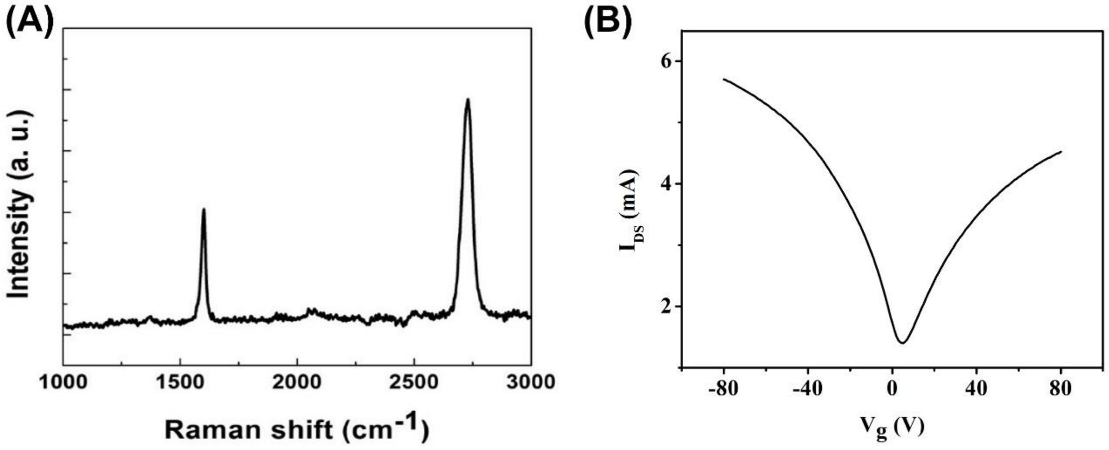

Figure 4.6 (A) The Raman spectrum of the graphene prepared by the chemical vapor deposition. (B) Characteristic curve of the graphene transistor with V_{DS} = 0.1V in N_2 environment.

4.3.3 Fabrication and characterization of graphene/$AgBiS_2$ transistors

To fabricate the graphene/$AgBiS_2$ transistors, the layer-by-layer deposition was employed again to deposit the NC film and exchange the ligands to provide different thicknesses of the $AgBiS_2$ films on the transistors.[24] We prepared two graphene transistors with 5-layer (5L) and 10-layer (10L) NC films. According to the SEM measurement, the film thickness of the 10L sample is about 72 nm (**Figure 4.7**).

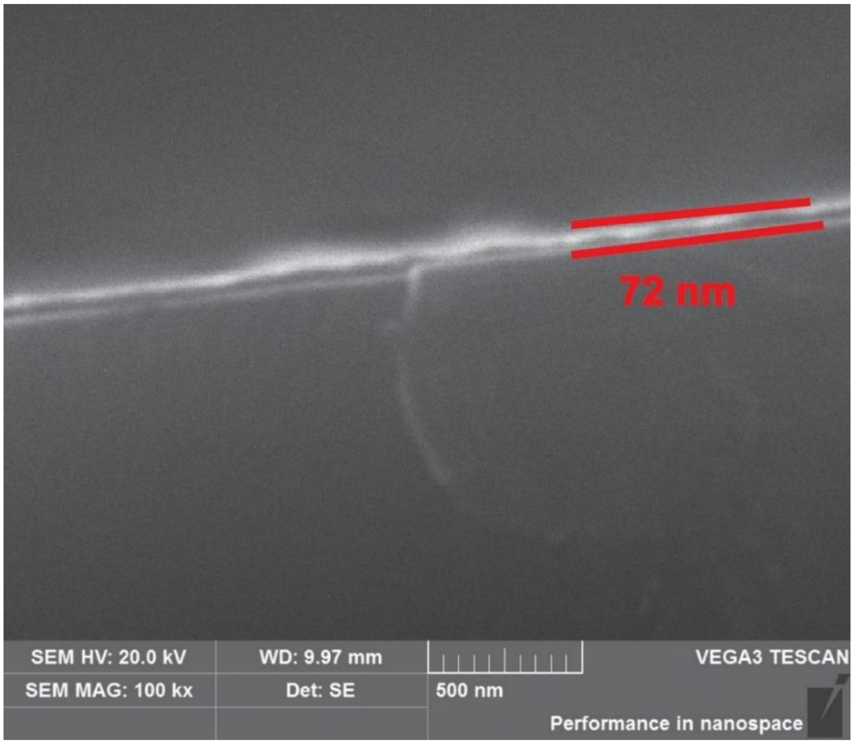

Figure 4.7 Cross-sectional SEM image for the 10-layer $AgBiS_2$ NC film.

Figure 4.8 A and **4.8B** show the transfer characteristic curves of the 5L and 10L devices with and without 895 nm light illumination. The curves of the devices in dark environment show that the Dirac point of the 5L and 10L devices are in the negative voltage region and indicating their n-type characteristic. Under light illumination, the Dirac point of 10L device is obviously shifted to the positive voltage side which indicates a net hole doping to the graphene channel. The decrease in current are resulted since the quantity of the main charge carrier electron is reduced due to the hole doping. As an evidence, the currents under illumination in **Figure 4.8 A** and **4.8B** at V_g = 0 V are also decreased as compared to the dark current. The absolute photocurrent of these devices was calculated by subtracting of the current of the illuminated and unilluminated devices. The high absolute photocurrents values around V_g = 0 V were observed in both devices. Therefore, the responsivity measurement was characterized at V_g = 0 V and V_{DS} = 0.1 V.

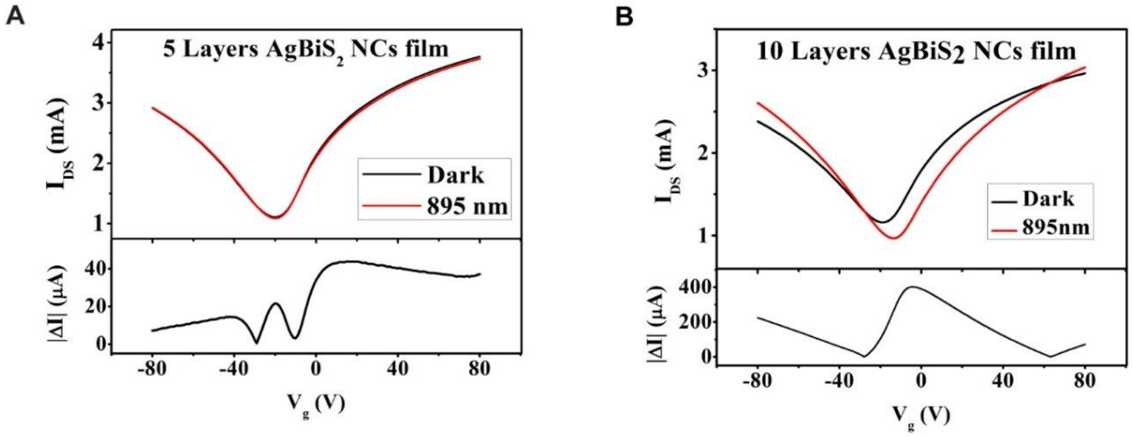

Figure 4.8 The transfer characteristic curves with/without 895 nm light illumination (UP) and photocurrent change (DOWN) for the hybrid transistor with 5 layers NC film (A) and 10 layers NC film (B), illumination intensity : 10.43 mWcm^{-2}.

Figure 4.9 shows the temporal photo-response of the 5L and 10L devices under an intensity of 12.28 μW cm^{-2}. The response time and current change are highly repeatable for both devices. The current change is about 1 μA for the 5L device and about 20 μA for the 10L device (**Figure 4.9A** and **Figure 4.9C**, respectively). The response time of the 5L device is 2.62 s while the recovery time is about 1.31s (**Figure 4.9B**). In addition, the response time becomes longer when the NC film thickness has increased. The response time of the 5L device is 9 s, while the recovery time is 29 s (**Figure 4.9D**). The results clearly demonstrate that under the same light intensity illumination, the thicker absorber film will lead to higher photocurrent change but longer stabilization time for response and recovery, vice versa.

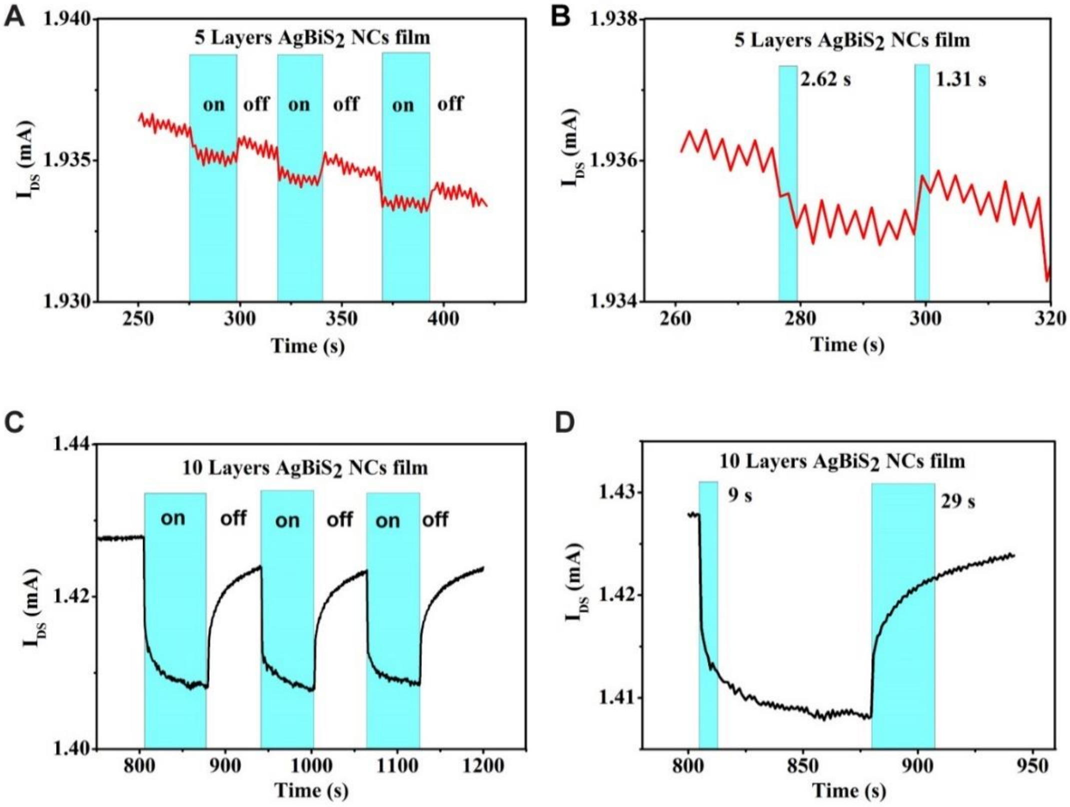

Figure 4.9 (A) The photocurrent response of the 5L device. (B) Reaction time and recovery time of the 5L device. (C) The photocurrent response of the 10L device. (D) Reaction time and recover time of the 10L device. The light intensity of 12.28 µW cm^{-2} was used for all the measurements.

Figure 4.10 shows a schematic diagram of charge transfer mechanism to illustrate the difference of stabilization time. When the light illuminates the graphene transistor, electron – hole pairs (EHPs) are generated and holes are transferred to the graphene channel (**Figure 4.10B**). This result in the decrease of Fermi level in the graphene, leading to positive shift of the Dirac point. According to the photogating effect, the holes will be accumulated in the graphene channel while electrons are trapped into the $AgBiS_2$ NC film. By considering the transistors were annealed and characterized in a N_2-filled glovebox, the surface adsorbates such as moisture and oxygen were removed as much as possible. So the trapping of charge carriers are likely come from the surface defects of the NCs.[1], [21], [22] Under light illumination, the current is changing with the increasing holes concentration in the graphene until equilibrium is reached.[1], [3] However, the holes at the graphene channel generate an opposing electric field to the absorber and hinder the rate of holes injection. As a result, a longer response time is needed for the equilibrium state.

Considering the thickness dependent light absorption of the absorber under illumination, fewer holes are generated from the NC film and injected to graphene for the 5L device due to weaker absorption. It produces a weaker opposing field as compared with the 10L device. When the light is off, the trapped electrons are released and recombined with the holes.

The 10L device have thicker NC film and hence it trapped more electrons than the 5L device. The total time of releasing the electrons is longer in the 10L device as compared to the 5L one. Consequently the temporal photo-response and recovery time of the 5L device is faster than the 10L device, but the photocurrent is smaller than the 10L device.[27]

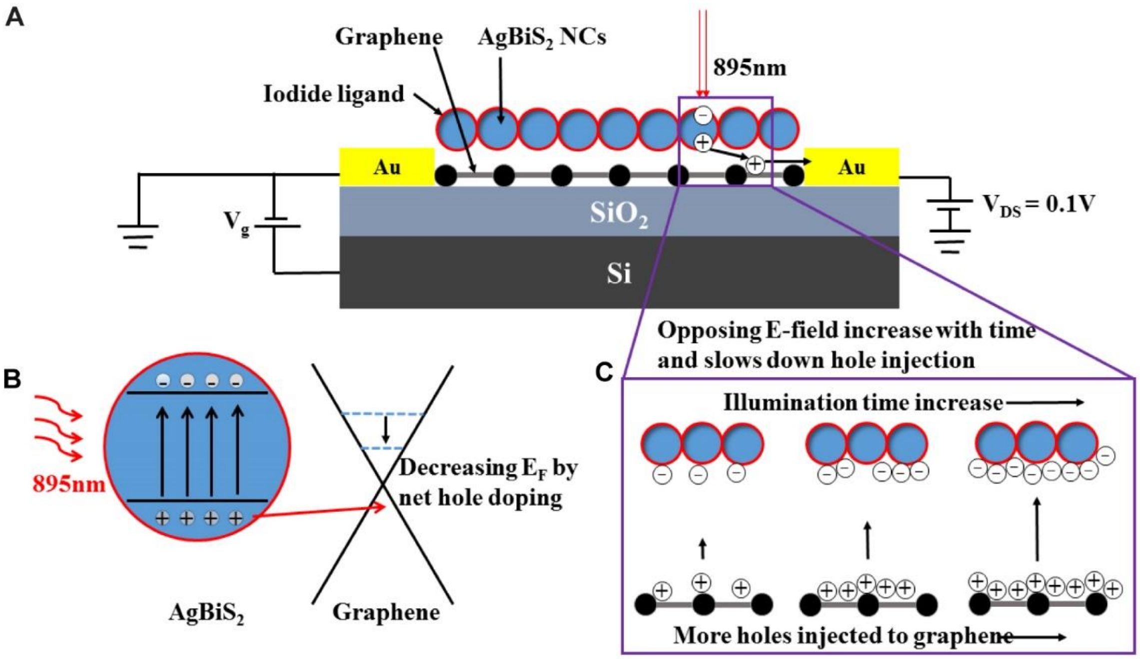

Figure 4.10 (A) The schematic illustration of the AgBiS$_2$ NCs/graphene photodetector. The wavelength of light is 895 nm. (B) The schematic diagram for charge generation at the AgBiS$_2$ NCs/graphene heterojunction under illumination. (C) The schematic diagram for opposing field at the AgBiS$_2$ NCs/graphene heterojunction, thicker film usually lead to a longer response time and stabilization time.

Recall the equation (1) for the photo-responsivity R with some mathematical manipulation [1], [3] i.e.

$$R = \frac{I_{ph}}{P_{in}} = \frac{\Delta I_{DS}}{W L E_{in}} = \frac{C_i \mu \Delta V_G V_{DS}}{L^2 E_{in}} \qquad (4\text{-}1)$$

where I_{ph} is the photocurrent, P_{in} is the incident power, W and L are the channel width (800 μm) and channel length (5 μm) respectively. E_{in} is the light intensity, C_i is the capacitance of the gate dielectric per unit area, V_{DS} and I_{DS} are the drain source voltage and current respectively, μ is the field effect mobility and ΔV_G is the gate voltage shift. **Figure 4.11** shows the photo-responsivity of the 5L and 10L devices as a function of light intensity. A maximum responsivity of 2.85×10^3 A W^{-1} is achieved at a detection limit 491.2 pW in the 5L device, while an improved maximum responsivity of 1.24×10^5 AW^{-1} with detection limit 8.86 pW is achieved in the 10L device. This detection limit of the 10L device is comparable to the PbS/graphene hybrid phototransistor.[89] Since graphene transistor has a weak responsivitiy, the high responsivities of the devices are mainly attributed to the $AgBiS_2$ NCs.

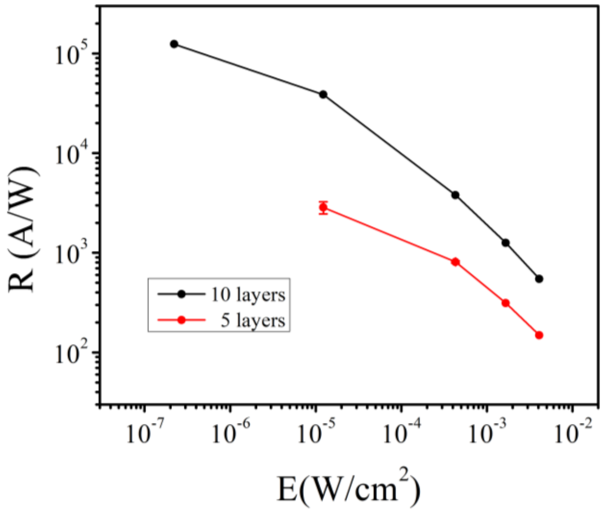

Figure 4.11 Photo-responsivities of the 5L and 10L devices under 895 nm illumination. The signal-to-noise ratio is less than 3.

Table 4.1 summarizes the device performance of this work and PbS NCs IR photodetectors in the literature.[10], [22], [78], [84] The photo-responsivities were normalized to V_{DS} to eliminate the contribution of the working voltage V_{DS} to R. The performance of our $AgBiS_2$/graphene transistors are comparable with the PbS-based photodetectors.

Table 4.1 Comparison of the $AgBiS_2$ photodetector with PbS based hybrid phototransistors.

Channel materials (atomic layers)	**Absorber and thickness**	**Wavelength/ lowest detection**	**Operating voltage V_{DS} (V)**	**Responsivity (AW^{-1})**	**R/V_{DS} ($AW^{-1}V^{-1}$)**	**Reference**
ME Graphene (1-2 layers)	60-80 nm PbS QDs in EDT	600 nm/8fW	5	$4x10^7$	8×10^6	[22]
ME SnS_2 (5 layers)	PbS QDs in EDT	400–1000 nm/~10 nW/cm^{-2}	1	$1x10^6$	1×10^6	[84]
ME MoS_2 (≥2 layers)	40-60 nm PbS QDs in EDT	400–1500 nm/3 μWcm^{-2}	1	6×10^5	6×10^5	[10]
CVD WS_2 (1 layer)	87.8nm PbS QDs in EDT	808 nm/ about 0.2 mW/cm^2	1.5	14	9.3	[78]
CVD Graphene (1 layer)	72nm $AgBiS_2$ NCs in Iodide	895 nm /8.86 pW	0.1	1.24×10^5	1.24×10^6	This work

ME: mechanical exfoliation, CVD: chemical vapor deposition, EDT: Ethanedithiol

4.4 Summary

In summary, we have successfully developed a facile method to synthesize $AgBiS_2$ NCs in an ambient environment without any observable by-products or oxide content. The NCs are highly dispersive in toluene which makes the NCs solution very suitable for solution processable device. The $AgBiS_2$ NCs was introduced to the graphene transistor, which showed high responsivity of 10^3 to 10^5 AW^{-1} with infrared illumination.

Chapter 5 Photoresponse of wafer-scale palladium diselenide films

5.1 Introduction

In Chapter 4, the $AgBiS_2$/graphene phototransistor was driven by the photogating effect. The responsivity can be enhanced by increasing the thickness of the absorber, but the response time is inevitably long due to the trapping/detrapping process of the charge carriers. In some application, requirement of fast response time is desirable. It may be fulfilled by 2DLM as a channel material. For example, few layer $MoSe_2$ transistor showed a responsivity of 93.7 A W^{-1} with a response time of 400 ms,[69] while few layer WSe_2 transistor showed a responsivity of 1.1 A W^{-1} with a response time of 1000 ms.[73] They both showed a lower responsivity but a faster response time than the $AgBiS_2$/graphene transistor.

As described in the Chapter 1, the development of the 2DLM-based field effect transistors (FETs) is still suffering from non-scalable production. Until now, most of the FETs were based on the exfoliation of bulk crystals. In most of these works, the dimensions of the flakes are usually within the range of several hundred µm.[10], [22], [30], [96]–[99] For the next generation photodetectors, a better controllability on thickness, area and shape are required.[25] In this aspect, sulfurization and selenization of metal precursor films show a trade-off between material quality and large-area with controllable thickness. This fabrication method has already showed its advantages in noble metal based 2DLMs such as $PtSe_2$ and $PdSe_2$.[39], [100]–[102]

Among the TMDC family, $PdSe_2$ has a unique in-plane pentagonal crystal structure.[103] As a high mobility semiconductor, the $PdSe_2$-based photodiode demonstrated excellent performance.[39], [40] However, the research on large-area $PdSe_2$ films is still scarce. In this chapter, we demonstrated the photodetection performance of $PdSe_2$ phototransistor where the $PdSe_2$ films were fabricated by selenization of Pd films. The films exhibited homogeneous semi-transparency across a 2” sapphire substrate. A broad photodetection ranging from 420 nm to 1200 nm was demonstrated. A high responsivity of 1.96×10^3 AW^{-1} for 980 nm was also achieved.

5.2 Chemicals and substrate

Selenium powder (99.99%) was purchased from Sigma Aldrich. Polished 2” in diameter c-plane (0001) sapphire wafer and polished 4'' SiO_2/Si (500 nm thick) were purchased from Silicon Valley Microelectronics, Inc.

5.3 Result and discussion

5.3.1 Synthesis of $PdSe_2$ films

The synthesis procedure of the $PdSe_2$ films is described in Section 3.1.3. **Figure 5.1A** illustrates the selenization process. The thicknesses are about 1.7 nm, 4.9 nm, 9.2 nm, 10.4 nm with the Pd deposition time of 15 s, 30 s, 60 s, 75 s, respectively. The temperature profile of selenization in tube furnace and the calibration curve of the $PdSe_2$ thickness against the sputtering time are shown in **Figure 5.1B** and **5.1C**, respectively. **Figure 5.2** provides the AFM images of the film thickness.

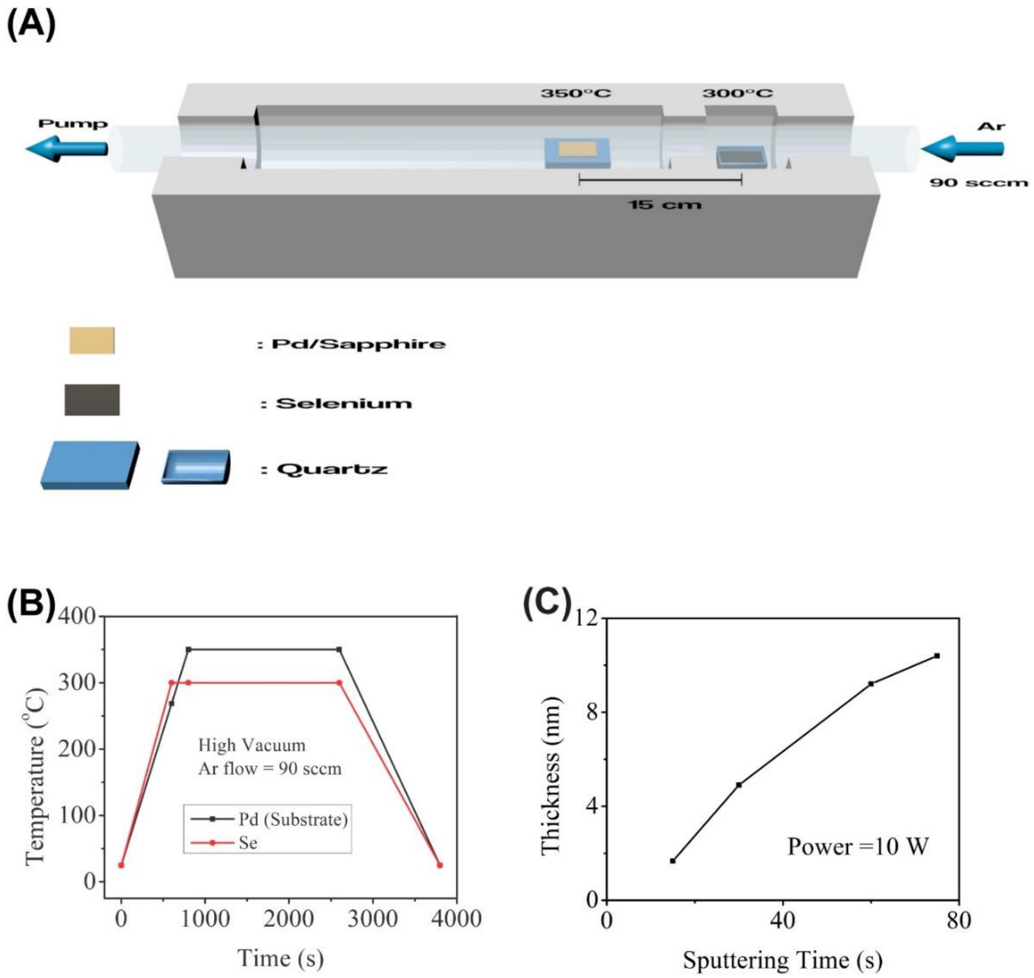

Figure 5.1 (a) Illustration of the selenization process. (b) Temperature profile of the selenization process. (c) The thickness of the $PdSe_2$ film as a function of Pd sputtering time.

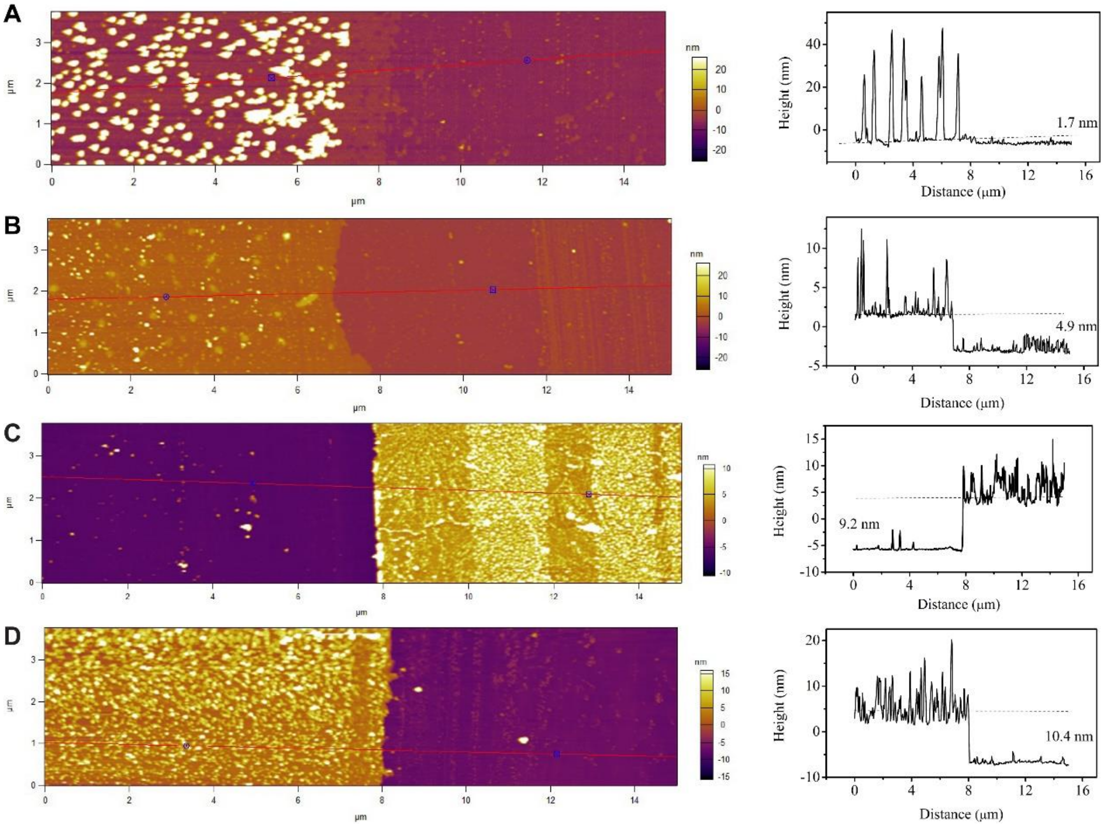

Figure 5.2 AFM measurement of the $PdSe_2$ films for different Pd deposition times: A) 15s, B) 30s, C) 60s and D) 75s.

5.3.2 Material characterization of $PdSe_2$ films

Figure 5.3A shows the photograph of a sapphire substrate, sputtered Pd film and the selenized $PdSe_2$ film. The Pd and $PdSe_2$ films are semi-transparent and $PdSe_2$ is darker. **Figure 5.3B** shows the Raman scattering spectra under the 433 nm laser excitation. The Raman modes of A_g^1 ($\approx 143\ cm^{-1}$), A_g^2 ($\approx 206\ cm^{-1}$), B_{1g} ($\approx 222\ cm^{-1}$) and A_g^3 ($\approx 256\ cm^{-1}$) are well consistent with the literature.[38], [104] The peak intensity was also varied with the thickness of the $PdSe_2$. **Figure 5.3C** shows the intensity ratio of A_g^1/A_g^3, it decreases as the thickness increases. The ratio could serve as an indicator of $PdSe_2$ film thickness. Similar result was also found in the literature.[101]

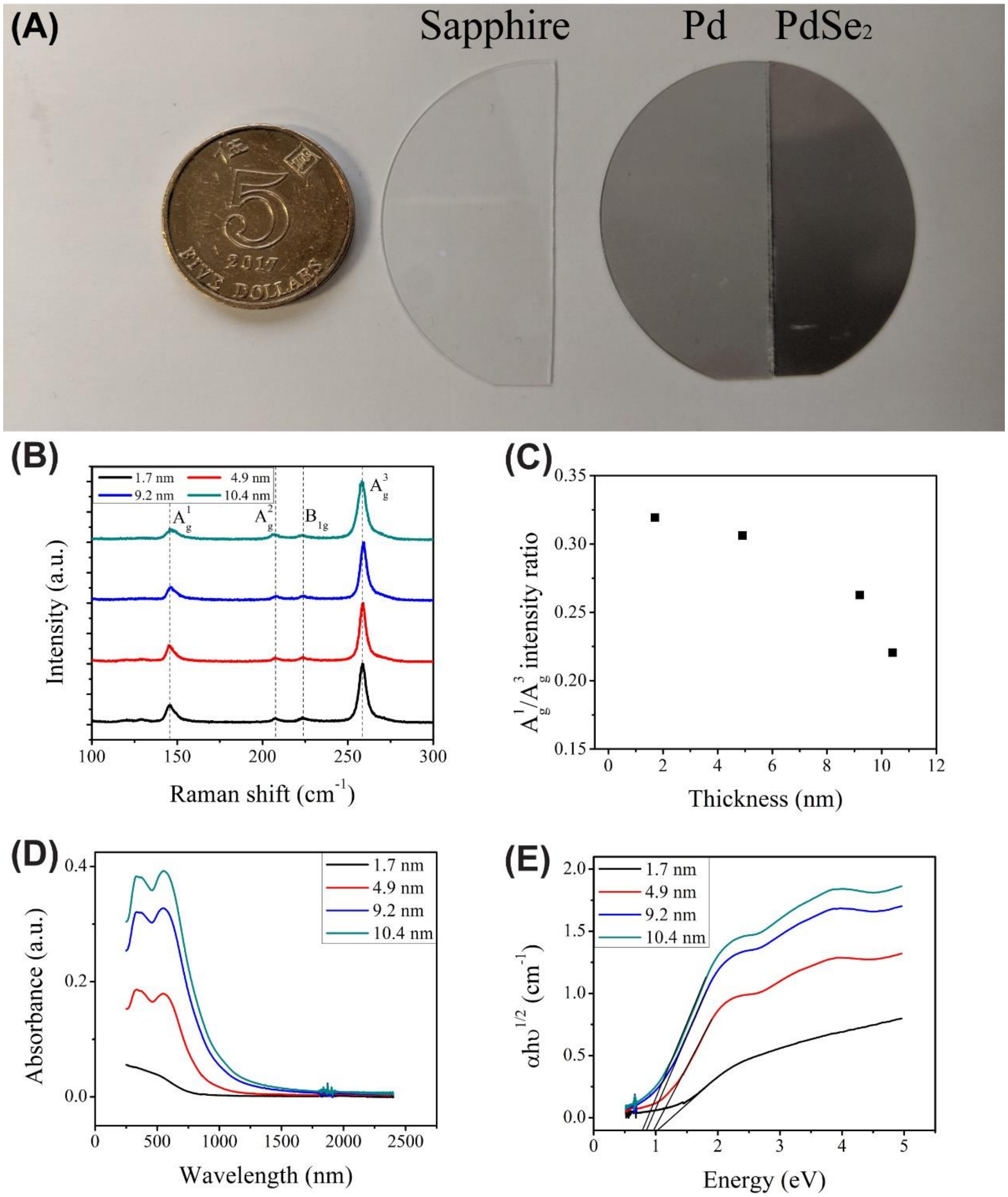

Figure 5.3 (A) The photographs of sapphire substrate, Pd and $PdSe_2$ on sapphire. (B) The Raman scattering of the films with various thickness. (C) The ratio of A_g^1/A_g^3 with various thickness. (D) The UV – vis – NIR absorption spectra and (E) the Tauc plot of the $PdSe_2$ films.

The UV – vis – NIR absorption spectra of the $PdSe_2$ films on sapphire are shown in **Figure 5.3D**. The absorbance and absorption range can be enhanced by increasing the thickness. Besides, there exists two obvious absorption peaks at 330 nm and 558 nm in the films which thickness reaches 4.9 nm or above. **Figure 5.3E** shows the Tauc plot of the samples. The optical band gap of the films decreases as the film thickness increases. The bandgap of the $PdSe_2$ films is thickness dependent.

The 9.2-nm-thick $PdSe_2$ film was selected to conduct TEM and XRD measurements. **Figure 5.4A** shows the TEM image of the film with the SAED pattern is shown in the inset. SAED patterns were randomly selected on the copper grid to investigate the crystallinity of the films in a microscopic view. The regular spot sequences with superimposition of the rings patterns are shown. The superimposition implies the film is polycrystalline. The crystal quality is comparable to the previous sulfurization/selenization works.[102], [103] The HRTEM image of the film is shown in **Figure 5.4B.** The lattice constant of 0.29 nm is consistent with the (200) planes of the previous reported $PdSe_2$ film.[105] Moreover, the EDX spectrum of the film was acquired during the TEM measurement (**Figure 5.4C)**. It shows the signals of carbon, copper, palladium and selenium. The stoichiometric ratio of the film was investigated by filtering the signals of carbon and copper. The remaining atomic ratio of Pd:Se is close to 1:2. No other elements can be found in the spectrum. Furthermore, the film on sapphire was measured by XRD. **Figure 2d-2f** show the broad range and magnified XRD spectrum. The (002) (≈ 22^o) and (113) (≈ 41.9^o) peaks matches the XRD peaks of single crystalline $PdSe_2$. The average crystal domain size of the (113) plane is about 148 nm according to the Scherrer formula $D = (0.94\ \lambda) / (\beta \cos\theta)$, where D = average crystallite size, β = FWHM in radians, θ = Bragg angle, $\lambda = 0.154$ nm.

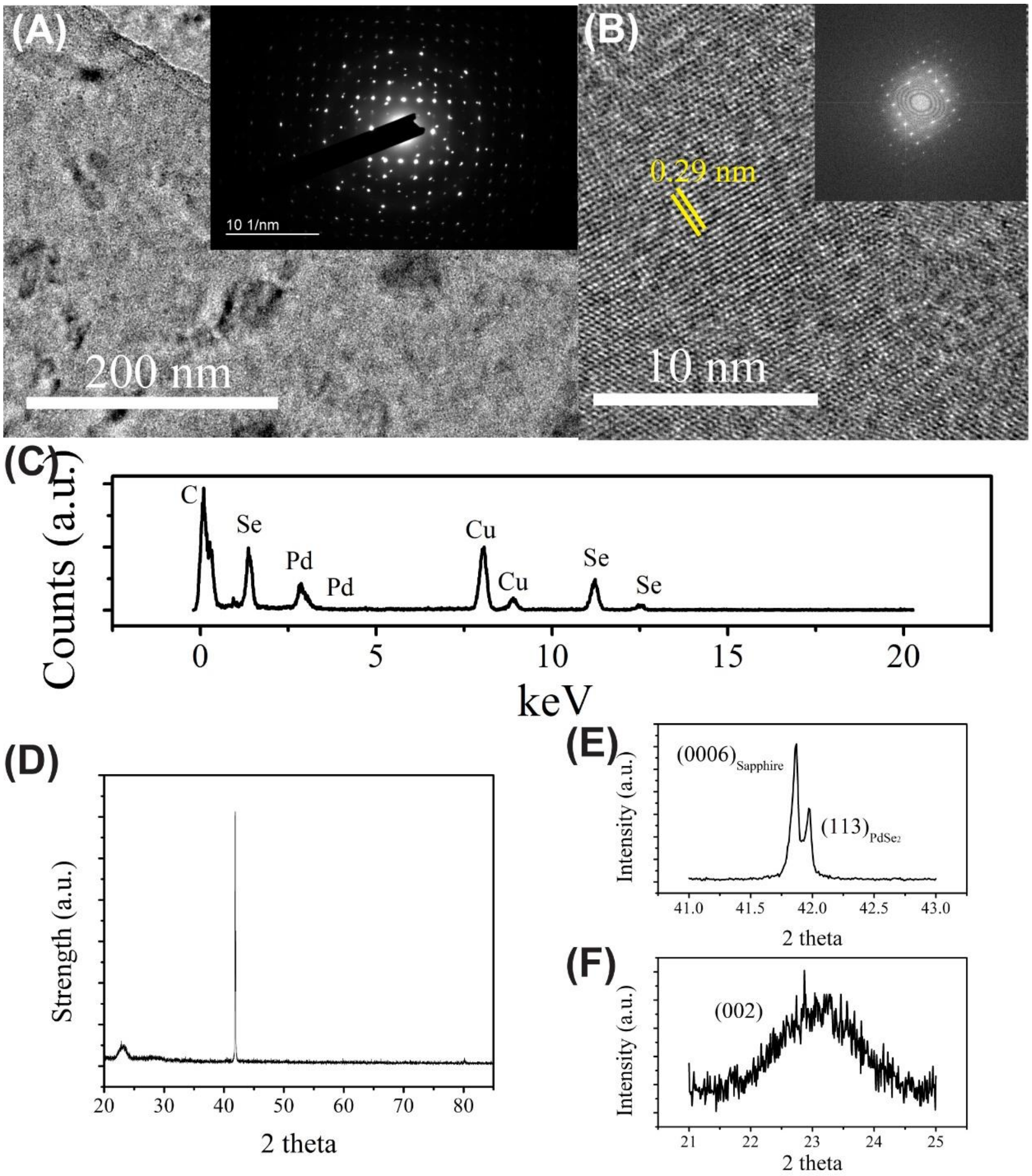

Figure 5.4 Material characterization of the 9.2 nm-thick $PdSe_2$ film. (A) The TEM image and SAED pattern (inset) of the film. (B) The HRTEM image and FFT (inset) of the film. (C) EDX spectrum of the film measured on the carbon coated copper grid. (D) XRD of the films. Enlarged XRD spectrum of (E) 41^o to 43^o and (F) 21^o to 25^o.

5.3.3 $PdSe_2$ phototransistor

To fabricate the $PdSe_2$ transistor, a thin layer of polystyrene (PS) was deposited on the $PdSe_2$ by spin-coating. To ensure the cleanliness and the intrinsic performance of the $PdSe_2$, the PS/$PdSe_2$ composite was peeled off by allowing deionized water to penetrate into the interface between $PdSe_2$ and sapphire slowly. The as-synthesized $PdSe_2$ thin films were then wet-transferred on a SiO2/Si with pre-defined Cr/Au electrode. The film was further annealed at 120 ^{o}C for 30 minutes for better contact. Finally, toluene was used to remove the PS under ambient conditions and the $PdSe_2$ transistors were ready to use.

The bottom gate FET configuration was further employed to investigate the transport properties of the 9.2 nm – thick $PdSe_2$ film. **Figure 5.5A** and **5.5B** show the dual sweep transfer and output characteristics curves of the $PdSe_2$ FET. The transfer characteristic curve shows the p-type characteristic with an on/off ratio of 1.50 under the sweep of gate voltage. Since the measurements were conducted in a nitrogen filled glove box with O_2 and H_2O concentration < 0.1 ppm, trappings from surface adsorbate were eliminated. The small hysteresis of the transistor indicates that the intrinsic traps of the polycrystalline $PdSe_2$ do not hinder the movement of the charge carriers effectively. The output characteristic curves show a typical resistance change of semiconductor channel in FET structure under different gate voltages. The field effect mobility

μ = 1.20 cm^2 V^{-1} s^{-1} was calculated according to the equation:[106], [107]

$$\mu = \frac{L}{WC_{OX}V_{ds}} \times \frac{dI_{DS}}{dV_g} \qquad (5\text{-}1)$$

where channel length L and width W is 5 μm and 800 μm respectively, the capacitance C_{ox} ($C_{ox} = \varepsilon_0\varepsilon_r/d$, $\varepsilon_0 = 8.854 \times 10^{-12}$ F m^{-1}, ε_r for SiO_2 is 3.9, and SiO_2 thickness d = 300 nm) and V_{SD} = 3V.[1]

The FET was then tested for photodetection under V_{SD} = 3V and V_g = 0V. The light emitting diodes (LEDs) with wavelengths of 420 nm, 530 nm, 850 nm, 980 nm and 1200 nm were served as the light sources. During light illumination, the $PdSe_2$ channel absorbs photons energy and generate of electron-hole-pairs (EHPs). The voltage bias V_{SD} will separate the electron and holes to different electrodes and the photocurrent will be detected. The device shows a broadband photoresponse from 420 nm to 1200 nm. The photocurrents (the difference of the currents with and without light illumination) are shown in **Figure 5.5C.** They show the stable photocurrent change under the same light intensity illumination. A rise time of 182 ms and decay time of 1.50 s was recorded (**Figure 5.5D**).

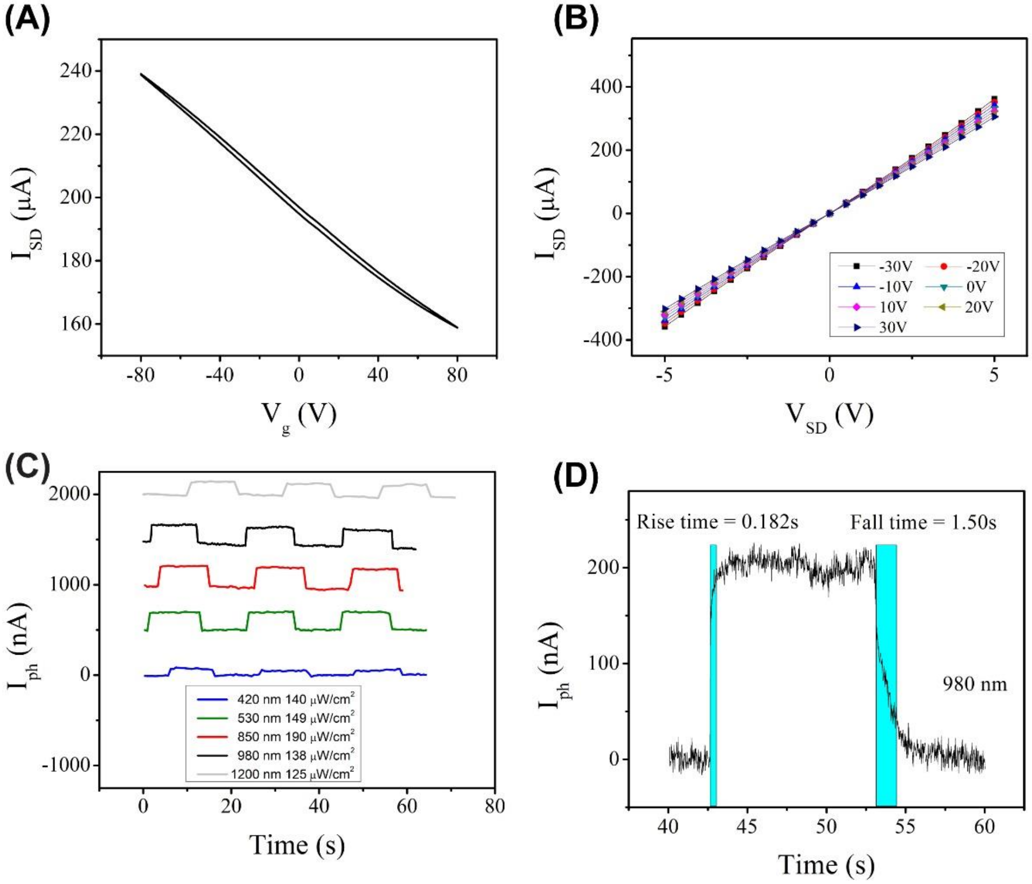

Figure 5.5 The electrical and light detection performance of the 9.2 nm – thick $PdSe_2$ transistors. (A) Dual sweep transfer characteristics curve and (B) output characteristics curve, (C) the photoresponse under different light wavelength and (D) the response time of device under 980 nm (Intensity : 138 μW cm^{-2}).

The log-log plots of the photocurrent and power are shown in the **Figure 5.6**. Under different sensing wavelengths, the log-log plots show the linear relationship between log I_{ph} and log P. Hence the typical $I_{ph} \propto P^{\beta}$ relationship can be experimentally established. The β values in the plots are ranging from 0.13 to 0.49 and less than the ideal value 1. The results indicate that there are loss of photocurrent in the transistor.[108] However, it is reasonable that the polycrystalline

$PdSe_2$ has material defects, the defect sites would act as the recombination location of photogenerated carrier.

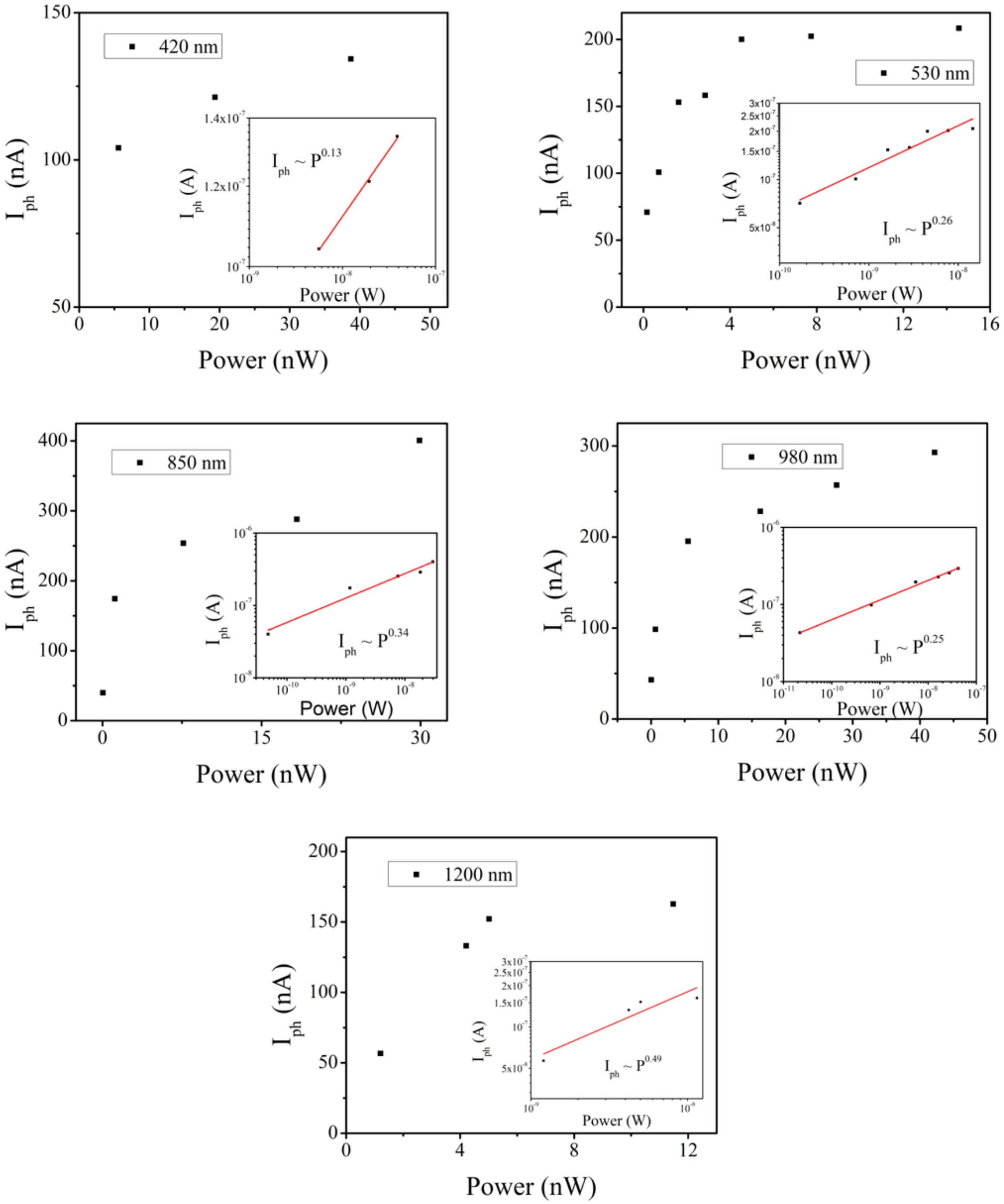

Figure 5.6 Photocurrent and power relationship in linear and logarithm scale. Linear relationship in logarithm scale are found in all sensing wavelength.

As the figure of merit in photodetection, responsivity R and specific detectivity D* were calculated. The responsivity R of the FET under the illumination of the aforementioned lights was then calculated by equation (1-1):

$$\mathrm{R} = \frac{I_{ph}}{\mathrm{P}} \tag{1-1}$$

where P is the illuminated power and I_{ph} is the photocurrent. I_{ph} is deduced by the subtraction of the currents with and without light illumination. Among all the testing conditions, the highest responsivity is found to be 1.96 × 10^3 A W^{-1} when 980 nm light with a power of 22 pW is used. The lowest responsivity is recorded (3.47 A W^{-1}) when 420 nm light is used. **Figure 5.7A** shows the photoresponsivity of the device at various wavelengths. The gain of the transistor is about 2.48 × 10^3, which is estimated by the equation $\mathrm{G} = \frac{I_{ph}}{\mathrm{P}} \times \frac{E}{q\eta}$,[64] where E is the photon energy of the incident light, η is the external quantum efficiency (assuming 100%) and q is the elementary charge.

The specific detectivity D* is another figure of merit of the photodetectors. To evaluate the D* values of the FET under different light intensities and wavelengths, the following equations for D* and noise equivalent power (NEP) are employed:[109]

$$\mathrm{NEP} = \frac{i_{n,rms}}{R} \quad \text{and} \quad \mathrm{D}^* = \frac{\sqrt{AB}}{NEP} = \frac{R\sqrt{AB}}{i_{n,rms}}$$

where A is the effective illuminated area of the channel = 4 × 10^{-7} cm^{-2}, B is the bandwidth, $i_{n,rms}$ is the root mean square value of the noise current and R is the responsivity of the device. Since 1/f noise was shown to be the most dominant noise source in 2DLM transistors,[21], [25] the noise level $i_{n,rms}$ of the $PdSe_2$ FET was found by the Fourier transform (FFT) of the measured dark current (**Figure 5.7B**) and was about ≈ 722 $pAHz^{-1/2}$ per unit bandwidth (B = 1 Hz). The maximum D* and their corresponding NEP values of different wavelengths are plotted in **Figure 5.7C**. The FET shows the highest specific detectivity in the sensing range 420 nm to 1200 nm within the values of 1.63×10^8 to 1.72×10^{10} W / $Hz^{1/2}$. The D* values are similar to other reported 2DLM transistors.[60]

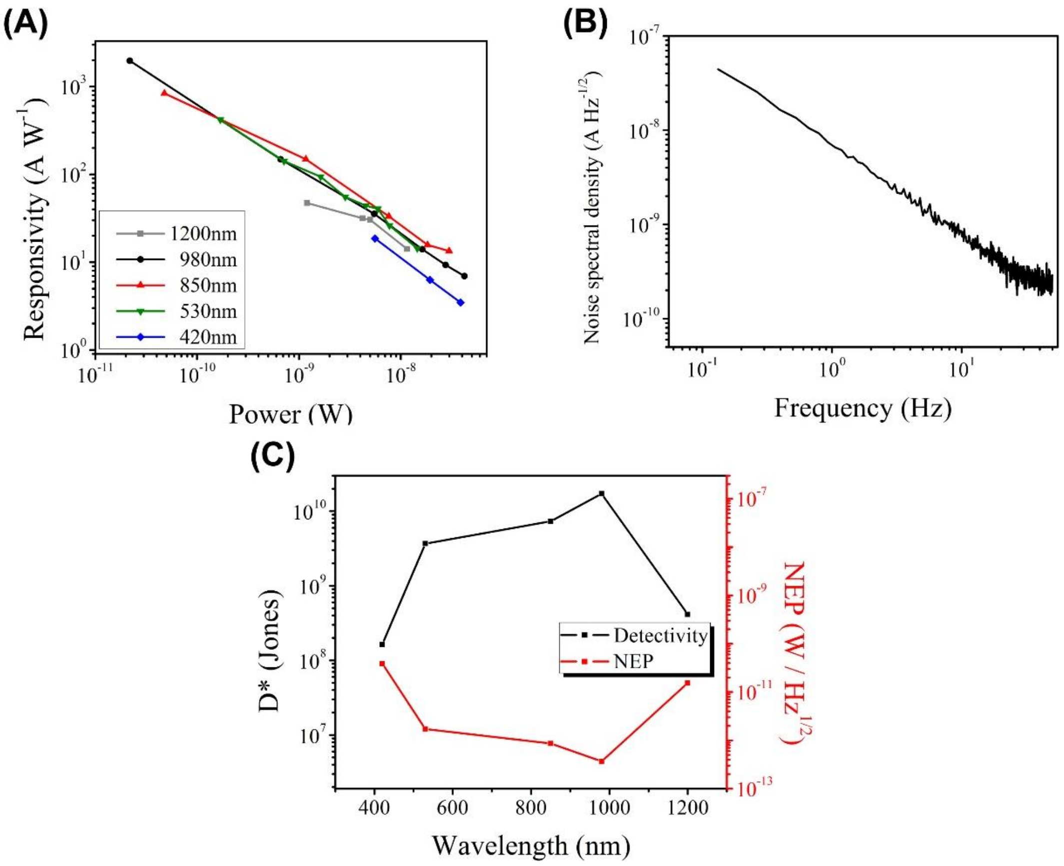

Figure 5.7 (A) Responsivity of the 9.2 nm – thick $PdSe_2$ transistor under different light illumination. (B) Analysis of noise spectral density of the device by the FFT of the dark current noise and (C) specific detectivities (D*) at different wavelengths

According to the previously reported $PdSe_2$ transistors which were fabricated by mechanical exfoliation of bulk crystals, they exhibited better photoresponse and responsivity in NIR region than the visible light spectrum.[40], [110] Although the polycrystalline structure of our $PdSe_2$ inevitably increases the free charge carriers from the defects and hence the conductivity, which result in a relatively low on/off ratio. However, the transistor also shows a better photoresponse in NIR region than the visible light region. Moreover, our $PdSe_2$ transistor shows similar responsivity and detectivity values to them. The highest reported responsivity and detectivity of pristine $PdSe_2$ transistor were about 708 A W^{-1} and 8.2×10^9 Jones at the wavelength of 1064 nm,[110] while our highest responsivity and detectivity of $PdSe_2$ transistor is 1960 A W^{-1} and 1.72×10^{10} Jones at the wavelength of 980 nm. It has been reviewed that some of the 2DLM photodetectors had achieved high responsivity due to long life time of the photocarriers, but not high mobility. Those mechanism will lead to a long response time in photodetection.[25] However, as indicated by the aforementioned β values which are smaller than 1, the material defects in polycrystalline materials will acted as the recombination center of the photocarriers and reduce the average life time. Regarding to this issue, although the thickness and synthesis are different, **Table 5.1** shows our results with other large area $MoSe_2$, WSe_2, MoS_2, $SnSe_2$ and ReS_2 phototransistors with similar device architecture.[61], [69], [73], [75], [111], [112] Our device exhibits a good balance between high responsivity and fast response time with the broadest detection range. The results reveal the selenization is a facile method for large scale production of $PdSe_2$ film for broadband photodetection.

Table 5.1 Comparison of the other 2DLM photodetectors. (1L: 1 layer, FL: few layers, CVD: chemical vapor deposition)

Channel	Fabrication method	Response Time (ms)	R (AW^{-1})	Detection range (nm)	Reference
9.2 nm $PdSe_2$	Selenization	182 (rise), 1500 (fall)	1960	420 – 1200	This work
FL $MoSe_2$	CVD	400	93.7	638	[69]
1L WSe_2	CVD	1000	1.1	532	[73]
1L MoS_2	CVD	1000	0.0011	488, 514.5	[75]
1L MoS_2	CVD	220000	2200	532	[111]
FL $SnSe_2$	CVD	100000	1.9	800	[112]
1L ReS_2	CVD	100000	16.14	633	[61]

5.4 Summary

In summary, we successfully synthesized large area polycrystalline $PdSe_2$ by selenization of Pd films. The crystallinity, electrical and optoelectronic properties of $PdSe_2$ were shown to be suitable for photodetection. The responsivity of the $PdSe_2$ phototransistors can reach 1960 AW^{-1} under the 980 nm illumination with relatively fast response time. Our work suggests that $PdSe_2$ is a promising material for broadband photodetection.

Chapter 6 Growth of vertically aligned $PtSe_2$ films towards hydrogen evolution reaction

6.1 Introduction

Platinum selenide ($PtSe_2$) is a noble metal based member of TMDC family with bandgaps of 1.2 eV and 0.21 eV for monolayer and bilayer samples respectively. The multiple-layer 1T-phase $PtSe_2$ exhibits semi-metallic behaviour [113] and the $PtSe_2$ nanoparticles show HER activity.[114] As described in Chapter 2, TMDCs with exposed edges are beneficial to HER. By considering the transfer of the electrons in their in-plane direction is more efficient than that in their out-of-plane direction, the vertically aligned $PtSe_2$ films would be more beneficial to HER.[85] Hence, the semimetallic, vertically aligned $PtSe_2$ electrode is a potential candidate for high performance HER.

The $PtSe_2$ films were prepared by depositing Pt films onto a substrate followed by selenization. The edge site density of the $PtSe_2$ films can be effectively controlled and the relationship between the edge density and the cathodic current density can be established. The edge density is determined by combining the Fast Fourier Transform (FFT) analysis of TEM images and software ImageJ. The high HER performance of the edge-rich $PtSe_2$ films reveals a new path to develop edge-rich TMDC electrocatalysts.

6.2 Chemicals and substrate

Selenium powder (99.99%) was purchased from Sigma Aldrich. Polished 2” in diameter c-plane (0001) sapphire wafer and polished 4” SiO_2/Si (500 nm thick) were purchased from Silicon Valley Microelectronics, Inc.

6.3 Results and discussion

6.3.1 Basic characterization of $PtSe_2$ films

Figure 6.1A and **6.1B** show the schematic synthesis process of the vertically aligned $PtSe_2$. Detail of the synthesis process is described in section 3.1.4. **Figure 6.1C** shows the photos of the as-prepared $PtSe_2$ films with thicknesses ranging from 1.9 nm to 76 nm on SiO_2/Si substrates. The crystal structure of $PtSe_2$ consists one layer of Pt atoms sandwiched between two layers of Se atoms. The Raman spectra of the $PtSe_2$ films with different thicknesses are shown in **Figure 6.1D**. The spectra reveal two feature peaks located around

189.4 cm^{-1} and 220.3 cm^{-1}, which correspond to E_g in-plane and A_{1g} out-of-plane Raman active modes respectively.[115] The E_g mode of the $PtSe_2$ is redshifted by around 5 cm^{-1} when the thickness increases from 1.9 nm to 76 nm, similar to that observed in the E^1_{2g} mode in MoS_2,[115] while the A_{1g} mode shows nearly no shift. Besides, the Raman intensity of the A_{1g} mode shows a significant increase when increasing the thickness of the $PtSe_2$ films, which might be induced by the enhancement of out-of-plane interactions through the increase of layer numbers.[115] **Figure 6.1E** shows some AFM images which indicate the thickness of the $PtSe_2$ films.

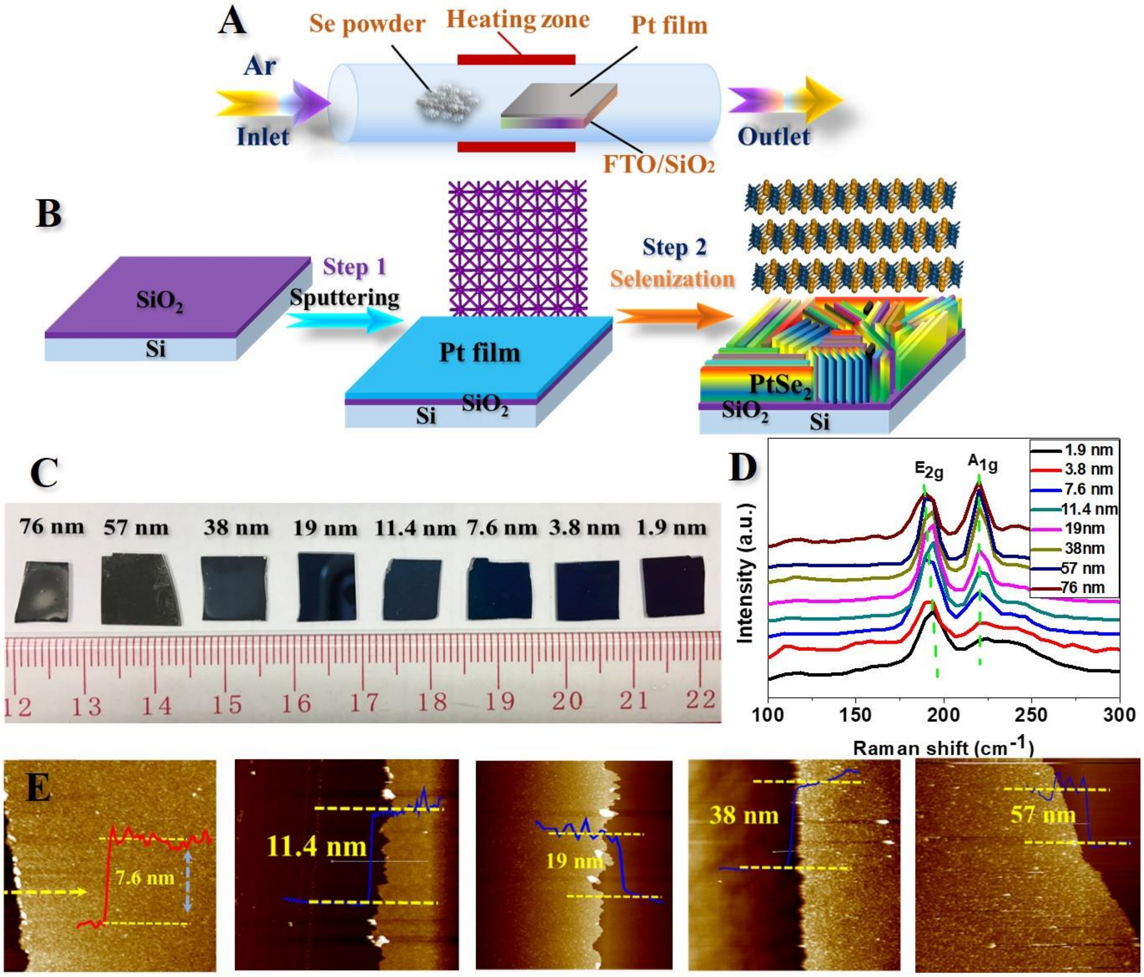

Figure 6.1 (A) Schematic illustrations of the growth process for $PtSe_2$. (B) Two-step growth method for the synthesis of $PtSe_2$ film. Step 1: deposition of Pt film on SiO_2/Si substrate by magnetron sputtering. Step 2: Selenization of the Pt film into $PtSe_2$. (C) Photo of the as-prepared $PtSe_2$ films with various thicknesses. (D) Raman spectra of $PtSe_2$ film with different thickness on SiO_2/Si substrate. (E) AFM images of the $PtSe_2$ films with different thicknesses on SiO_2/Si substrates

To confirm the crystal structure of the as-prepared $PtSe_2$ films, X-ray diffraction (XRD) was performed. **Figure 6.2** shows the XRD pattern of the $PtSe_2$ sample (38 nm). The $PtSe_2$ film possesses two pronounced peaks located at 16.5° and 44.3° corresponding to the (001) and (111) crystal planes respectively.

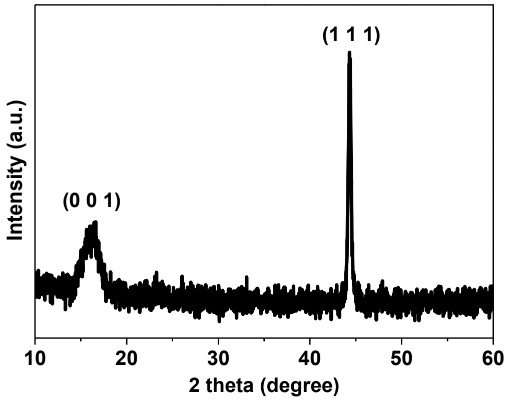

Figure 6.2 A typical XRD pattern for $PtSe_2$ film on SiO_2/Si

The method can also synthesize $PtSe_2$ films onto FTO glass substrates, as shown in **Figure 6.3A**. The Raman spectra of the $PtSe_2$ films with different thicknesses on FTO can be found in **Figure 6.3B**. The peaks are similar to **Figure 6.1D**. **Figure 6.3C** depicts the UV–vis–NIR absorption spectra of the $PtSe_2$ films with different thicknesses on FTO. The absorption spectra cover UV to NIR regions. The absorption intensity of the $PtSe_2$ increases with the increasing thickness, which is confirmed by the color changes of the $PtSe_2$ as shown in **Figure 6.3A**.

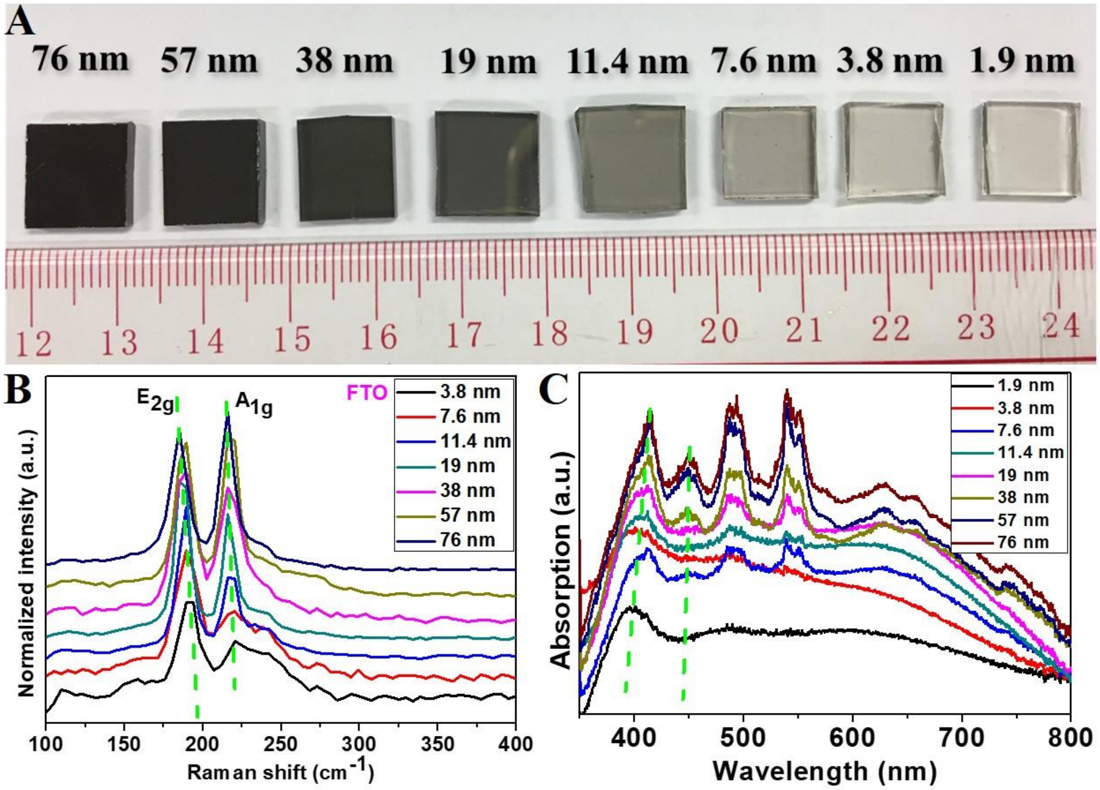

Figure 6.3 (A) Optical image of the $PtSe_2$ films on FTO substrates. The inset shows a typical Raman spectrum; (B) Raman spectra of various samples as shown in (A). (C) Absorption spectra of the $PtSe_2$ films on FTO substrates as a function of thickness.

X-ray photoelectron spectroscopy (XPS) was used to analyze the $PtSe_2$ film. The results is shown in **Figure 6.4A**. The Pt-related peaks (i.e., Pt-4$f_{5/2}$ at 76.2 eV and Pt-4$f_{7/2}$ at 72.9 eV) and the Se-related peaks (i.e., Se-3$d_{3/2}$ at 55.1 eV and Se-3$d_{5/2}$ at 54.3 eV) are corresponding to the reported values for $PtSe_2$ film.[114] The oxidation states of Pt and Se can be found in **Figure 6.4B** and **Figure 6.4C**, respectively. For the Pt 4f spectrum, a primary peak located at ~ 72.9 eV is attributed to $PtSe_2$. The peaks located at ~ 71.5 eV, ~ 74.6 eV and

~ 75.2 eV are corresponded to unreached Pt metal whereas the one located at ~ 77.4 eV is attributed to oxides (i.e. PtO_x). By comparing the relative atomic percentages of $PtSe_2$, Pt (5.5 at%) and PtO_x (1.8 at%), we can conclude that the majority of the Pt has been transformed into $PtSe_2$ (92.7 at%). As for the Se 3d spectrum, besides the primary peak from $PtSe_2$, the other peaks located at 52.8 eV and 58 eV are attributed to Se and Se-O respectively.

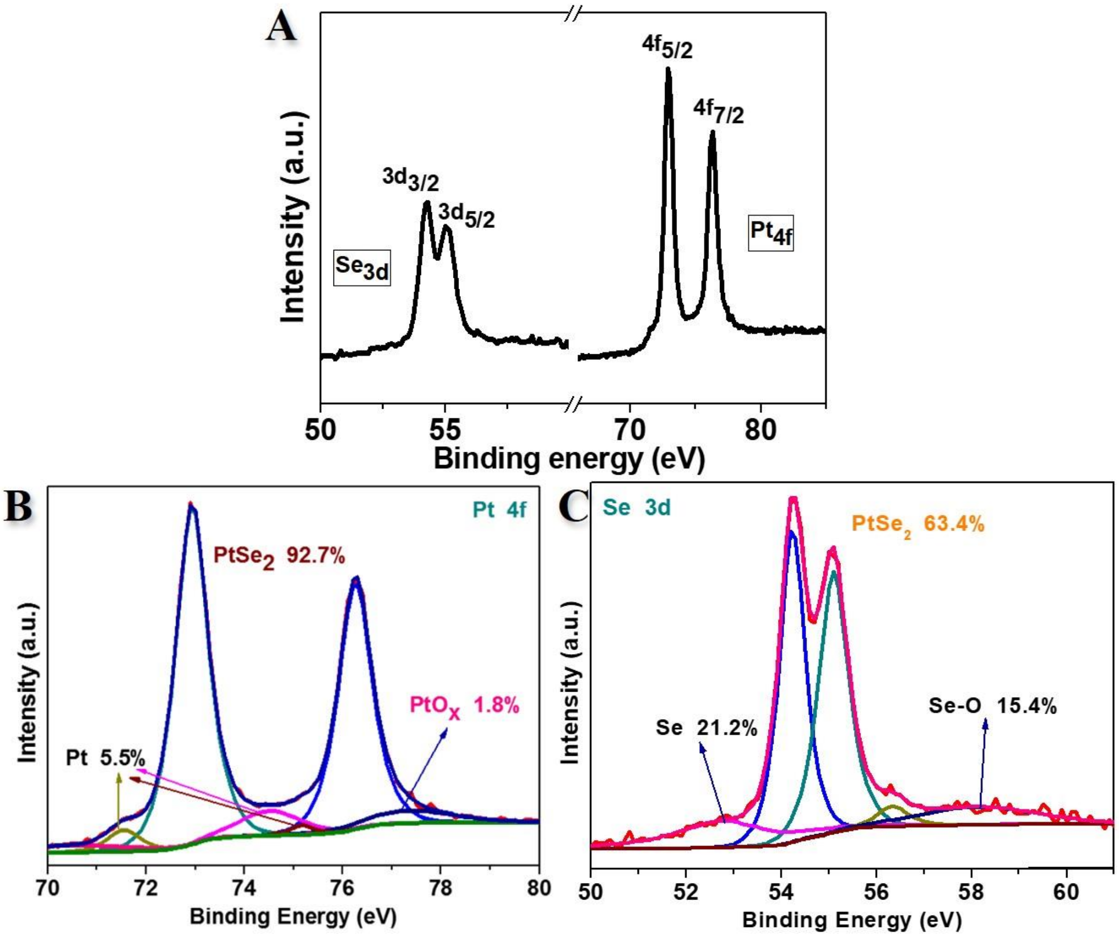

Figure 6.4 (A)The XPS spectrum showing Pt 4f and Se 3d; (B) and (C) show the XPS spectra of Pt 4f and Se 3d with deconvolution peak fitting respectively

STEM measurement was performed to characterize the $PtSe_2$ films. The films were found to have some area with vertically aligned $PtSe_2$. **Figure 6.5** compares the morphology of the films with thickness 3.8 nm and 38 nm. **Figure 6.5A** and **6.5B** shows the low-magnification TEM images of the $PtSe_2$ films while the STEM was operated in TEM mode. The obtained film is nearly continuous. **Figure 6.5C** and **6.5D** show their TEM images with the higher resolution. The insets in **Figure 6.5C** and **6.5D** show their SAED patterns and confirms both samples are polycrystalline. For the 3.8 nm – thick $PtSe_2$ film in **Figure 6.5C**, the five highlighted red circles in SAED pattern are corresponding to (100), (110), (200), (113) and (122) planes with lattice spacings of 3.25, 1.82, 1.64, 1.24 and 1.11 Å, respectively. For the 38 nm-thick $PtSe_2$ film in **Figure 6.5D,** the seven highlighted red circles are corresponding to (001) (100), (011), (012), (110), (111) and (201) planes with lattice spacing of 5.21, 3.25, 2.74, 2.01, 1.83, 1.77 and 1.54 Å, respectively. **Figure 6.5E** shows the HRTEM image of the 3.8 nm-thick $PtSe_2$ film. The crystal plane spacing of the sample is ~0.182 nm, which corresponds to (110) crystal plane of the $PtSe_2$. **Figure 6.5F** shows the HRTEM image of the 38 nm-thick $PtSe_2$ film. The main surface sites are turned into edge sites when the film thickness increases. It clearly reveals the periodic atom arrangement of the $PtSe_2$ film at the imaging location. The inset reveals the line scan profile of that location, which shows that the layer-to-layer spacing is 5.2 Å and corresponding to (001) crystal plane. The images show the vertically aligned layers standing on the surface are more frequently found in the thicker film. The results of the 38 nm-thick $PtSe_2$ film are similar to the previously reported MoS_2 and MoS_2 which layers are vertically aligned.[13] The result shows the edge density of the $PtSe_2$ films is different for different thickness.

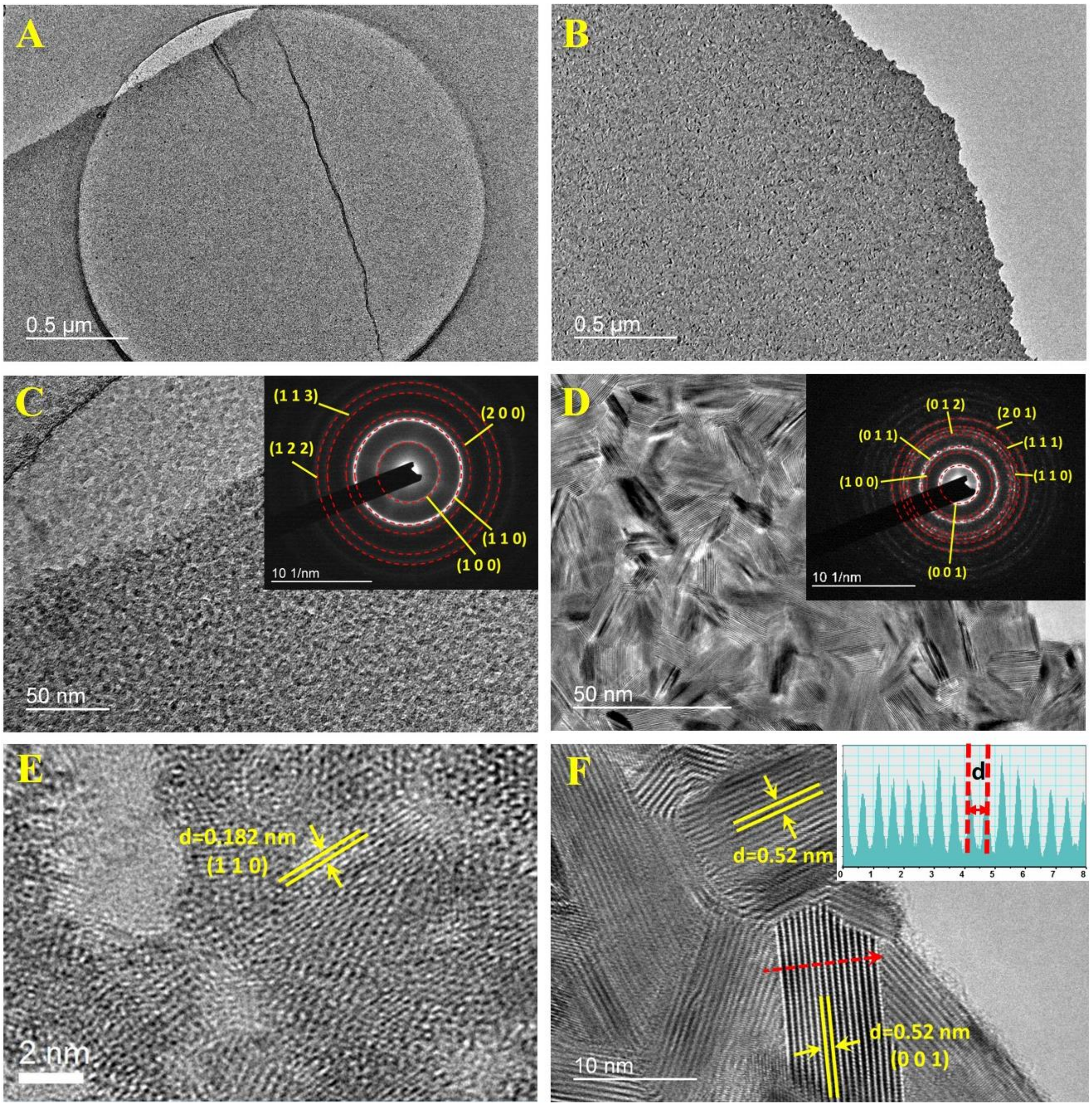

Figure 6.5 Low magnification TEM image of the (A) 3.8 nm – thick and (B) 38 nm – thick $PtSe_2$ film, respectively. Higher magnification TEM image of the (C) 3.8 nm – thick and (D) 38 nm – thick $PtSe_2$ film, respectively. Insets in (C) and (D) show their SAED patterns. HRTEM images of (E) 3.8 nm – thick and (F) 38 nm – thick $PtSe_2$, respectively. Inset in (F) reveals the layer-to-layer spacing is 5.2 Å.

The EDX result is shown in **Figure 6.6. Figure 6.6A** confirms that the studied sample consists of Pt and Se elements. The area in **Figure 6.6B** was selected to perform STEM-EDX mapping images. The STEM-EDX mapping images (**Figure 6.6C** and **6.6D)** show the homogenous distribution of Se and Pt elements.

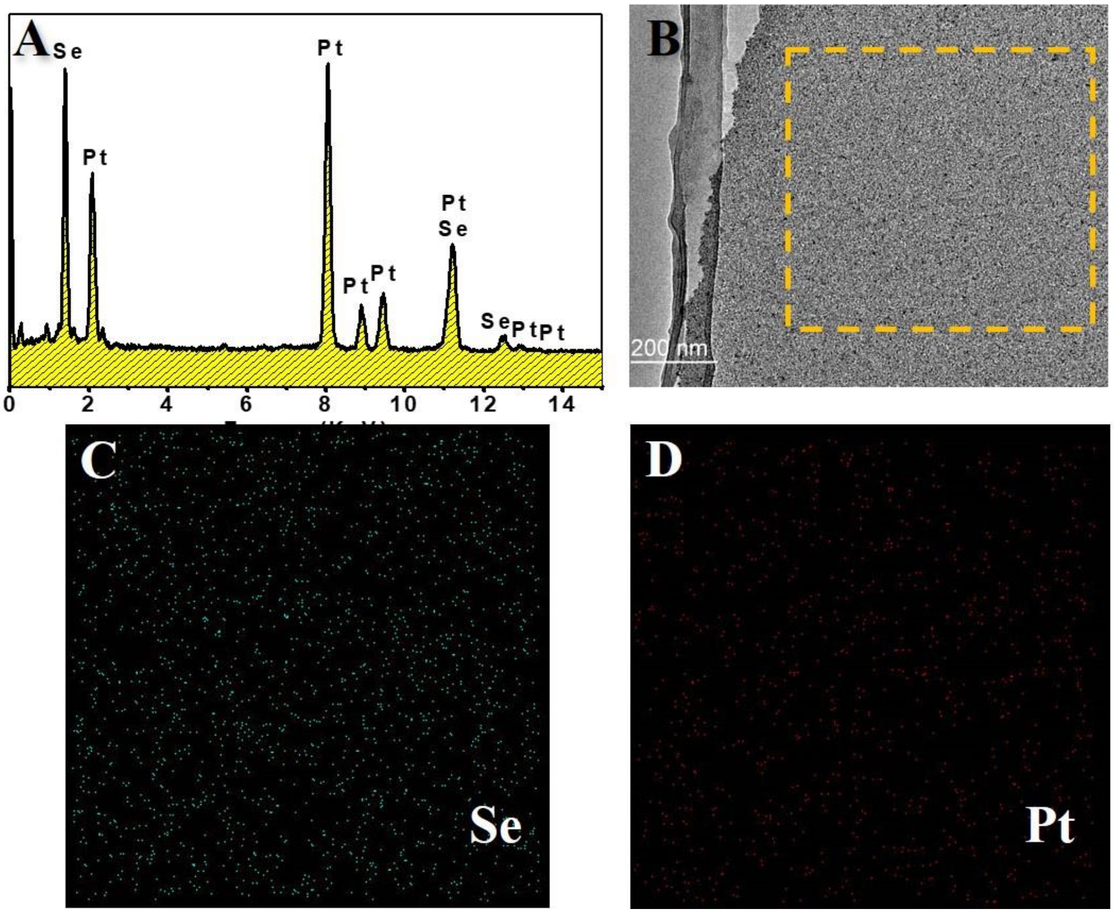

Figure 6.6 (A) EDX result of the studied sample. (B) Low-magnification TEM image of the $PtSe_2$ film with selected area; (C) and (D) STEM-EDX mapping of Se and Pt elements in the sample.

6.3.2 Edge density

In order to estimate the edge density of the $PtSe_2$ thin films as a function of the film thickness, we developed a method by applying image analysis tool to reveal the edge structures of the sample in a TEM image. **Figure 6.7A** shows the TEM image of a 57 nm-thick $PtSe_2$ film. The fast Fourier transform (FFT) of the image is shown in **Figure 6.7B**. The edge structures can be separated by filtering the reciprocal space (i.e. FFT of the original image). Some selective masks are applied on the FFT image to the unwanted corresponding interlayer spacing of $PtSe_2$. After reconstructions by inverse FFT (**Figure 6.7C**), the contrast of the edge structures can be enhanced while the domains in other crystal directions are suppressed. Then the Gaussian blurring is applied (**Figure 6.7D**) to reduce the lattice contrast and appropriate threshold for the edges of the vertically grown domains (**Figure 6.7E**). The total area coverage of the vertically grown domains can be retrieved (**Figure 6.7F**) by the Analyze Particles function in the ImageJ software. The edge coverage density of the 57 nm-thick $PtSe_2$ film is estimated to be ~ 48%.

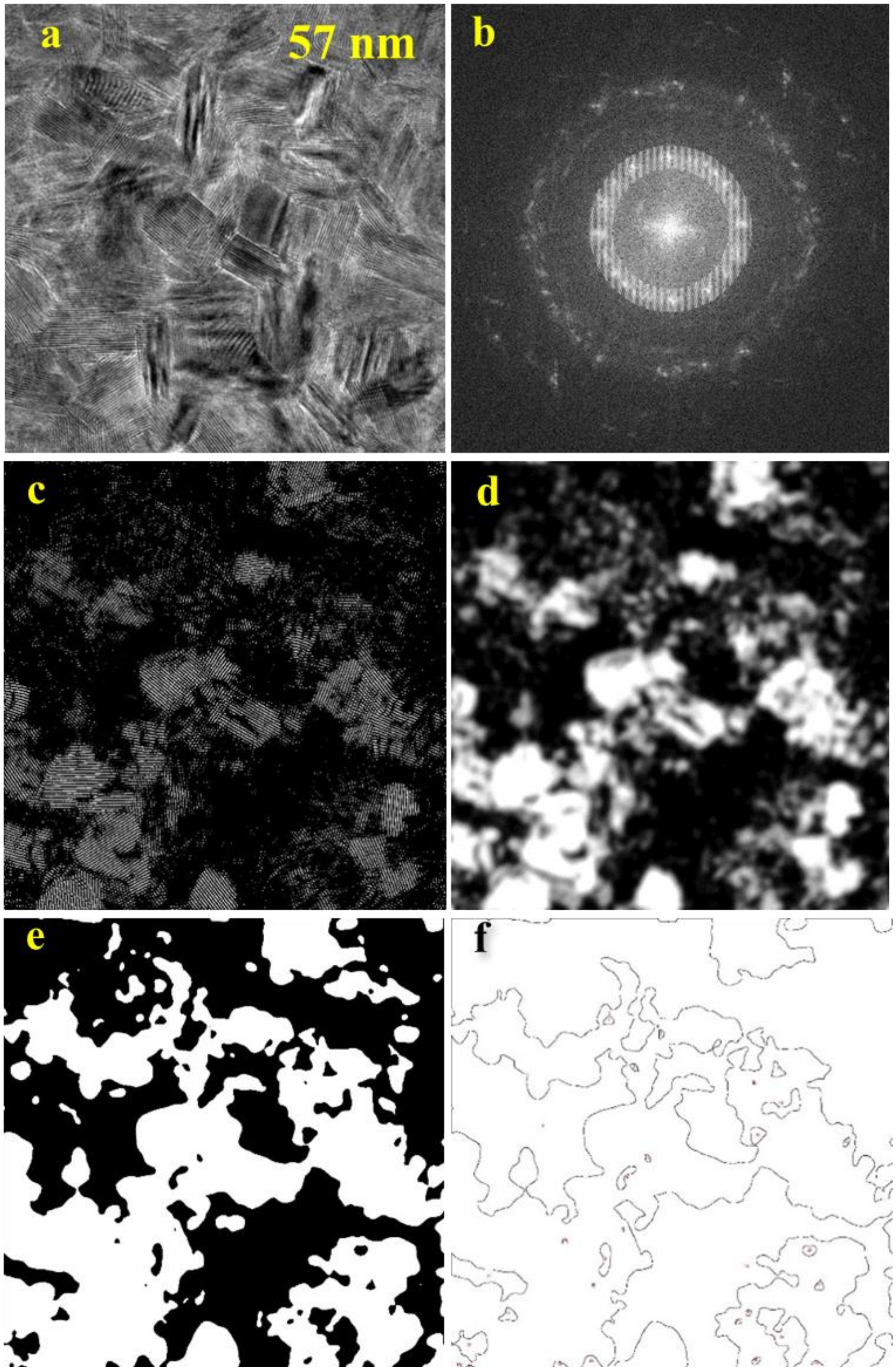

Figure 6.7 (a) Original TEM image of the $PtSe_2$ film; (b) Corresponding FFT image; (c) after filtering and invert FFT process; (d) after applied Gaussian Blurring; (e) apply threshold; (f) count area percentage by IMAGE J software. Then the edge coverage density on the top surface can be estimated to be ~48% for 57 nm thick $PtSe_2$ film.

By applying this technique, the edge density of the $PtSe_2$ thin films based on at least three regions with various thicknesses are listed in **Table 6.1**. As the thickness of the $PtSe_2$ film increases from 3.8 nm to 76 nm, the edge density increases from ~0 to ~81%, which could be confirmed by observing the increase of edge sites on the surface of $PtSe_2$ by increasing its thickness as shown in **Figure 6.8**. It should be noted that the edge density here only represents the coverage of the edge structures on the top surface. The edge structures can also be found below the top surface.

Table 6.1 The relationship between the thickness of $PtSe_2$ film and the corresponding edge site density.

Thickness	3.8 nm	7.6 nm	19 nm	38 nm	57 nm	76 nm
Edge density	~ 0	~ 2±0.2%	~ 8±0.3%	~ 39±1%	~ 48±2%	~ 81±5%

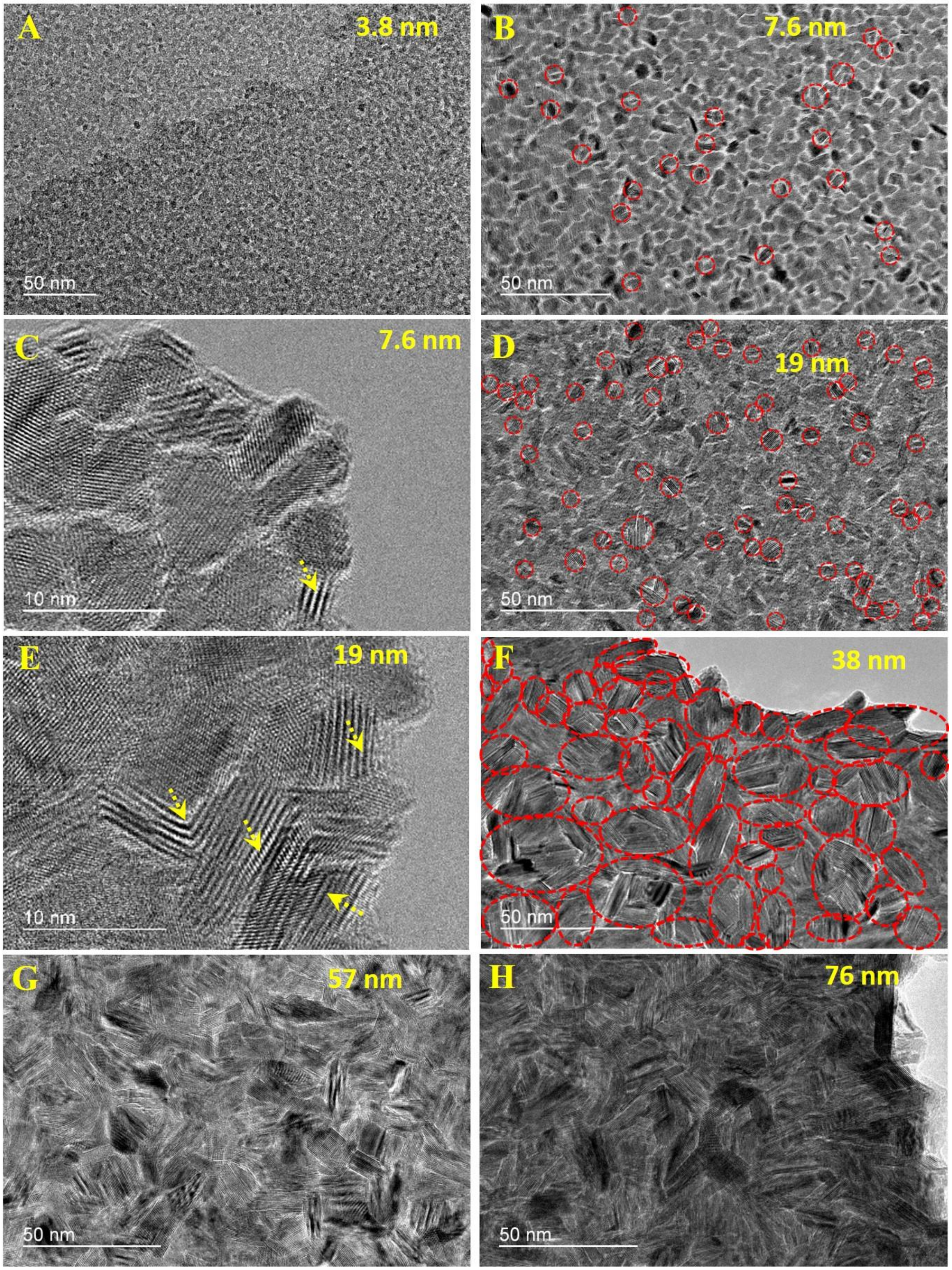

Figure 6.8 (A) TEM image of the $PtSe_2$ film with a thickness of 3.8 nm; (B) TEM image of a 7.6 nm thick $PtSe_2$ film; (C) HRTEM image corresponds to (B); (D) TEM image of a 19 nm thick $PtSe_2$ film; (E) HRTEM images corresponds to (D); (F)-(H) TEM images of 38 nm, 57nm and 76 nm $PtSe_2$ films Here the yellow arrows represent the edge-rich areas.

The morphologies and the growth process of our edge-rich $PtSe_2$ films are similar to the MoS_2 and $MoSe_2$ with vertically aligned layers.[13] The growth mechanism of our edge-rich $PtSe_2$ films may follow the one proposed by the authors where the chemical conversion occurs much faster than the diffusion of the Se gas into the film. In the mechanism, the diffusion along the layers through van der Waals gaps is much faster across the layers. Consequently, the layers grew perpendicular to the substrate. The thicker the Pt films provide a larger density of edge structures.

6.3.3 HER performance of the $PtSe_2$ films

In order to evaluate the electrocatalytic HER activity of the $PtSe_2$ films, LSV measurement was carried out in a standard three-electrode system with 0.5 M H_2SO_4 solution as electrolyte. Detailed characterization condition is given in section 3.2.8. To wet-transferred the $PtSe_2$ films onto a glassy carbon (GC) disk electrode to serve as working electrode, a protective layer of PMMA was spin-coated onto the $PtSe_2$ film. After that, the substrate with the PMMA coated $PtSe_2$ was placed into a NaOH bath. The detached PMMA coated $PtSe_2$ film was then transferred onto the glassy carbon electrode. Acetone was used to remove the PMMA and the working electrode fabrication is completed. Bare GC and Pt working electrodes were also characterized under the same measurement conditions for comparison.

Figure 6.9A shows the schematic illustration of the H_2 generation on the edge-rich $PtSe_2$ films. **Figure 6.9B** shows the polarization curves of the $PtSe_2$ electrodes with different thicknesses, GC electrode and platinum electrode. When the potential towards the negative potential direction, the cathodic current density increases due to the electrocatalytic reduction of protons to H_2. As a substrate electrode, the HER activity of the bare GC electrode is poor with an onset overpotential about 787 mV. It can be seen that all the $PtSe_2$ electrodes exhibit electrocatalytic HER activity and the cathodic current density increases with the $PtSe_2$ films thickness. The maximum current density of 227 mA/cm^2 is achieved on the $PtSe_2$ film with a thickness of 76 nm, which is about half of the current density of the Pt electrode. The HER performance of the $PtSe_2$ electrodes are obviously much better than that of the GC electrode. In addition, the smallest onset overpotential recorded on the $PtSe_2$ electrode is located at −170 mV vs. RHE, corresponding to a small HER overpotential of ~ 327 mV at a current density of 10 mA/cm^2. This result suggests that the $PtSe_2$ electrodes amplify proton reduction process. This phenomenon could be attributed to the high edge density on the surface of the $PtSe_2$ films. As shown in **Figure 6.9C**, an increasing relationship between the edge density and the current density is established. The edge-rich $PtSe_2$ films play a key role in enhancing the HER activity.

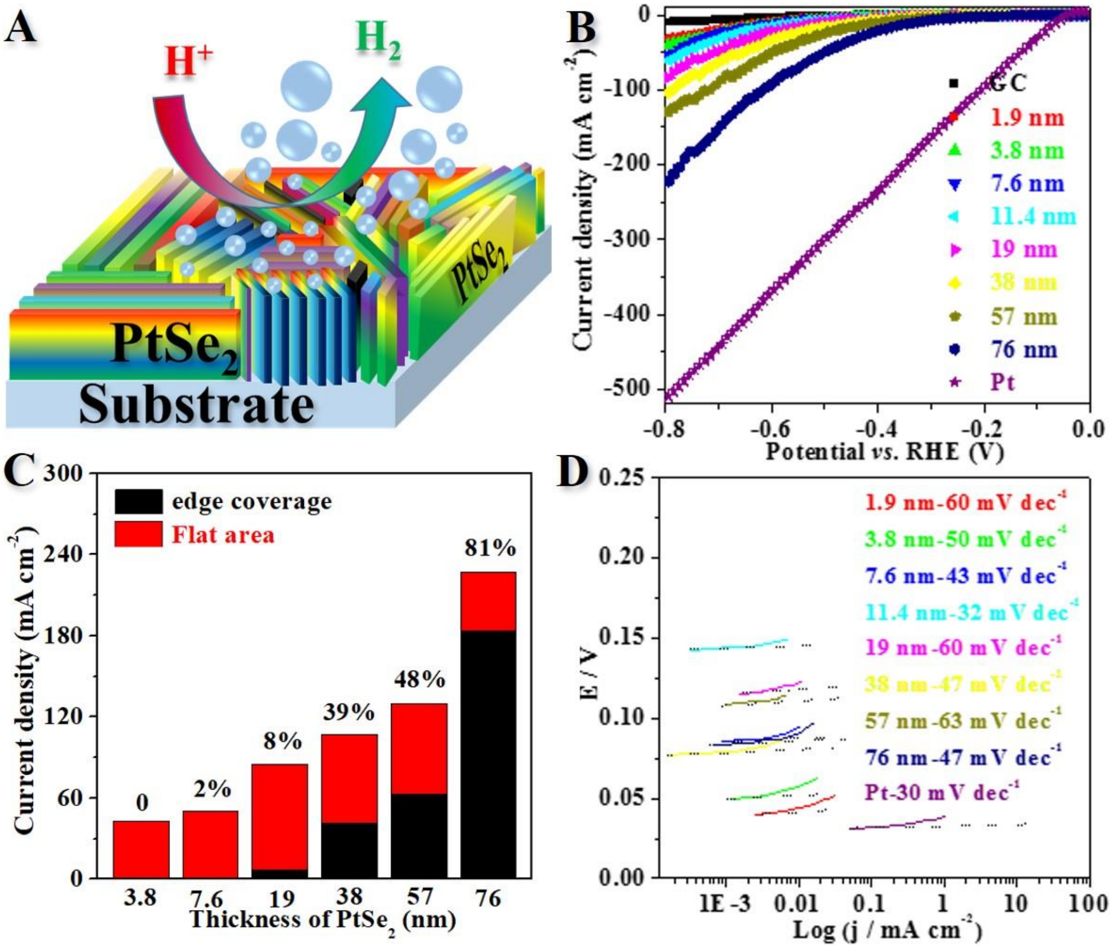

Figure 6.9 The electrocatalytic performance of $PtSe_2$ film. (A) Schematic illustration of the HER activity of $PtSe_2$ film; (B) polarization curves; (C) the relationship between the current density and edge sites density on the top surface of $PtSe_2$ film; (D) Tafel plots corresponding to (B);

Moreover, Tafel slope is extracted evaluate the performance of the HER catalyst. The corresponding values of the samples can be calculated according to the Tafel equation.[116] Accordingly, the Tafel slopes for the $PtSe_2$ with different thicknesses can be found in **Figure 6.9D**, which reveals the values of Tafel slope ranging from 32 to 63 mV dec^{-1}. It is worth noting that, the smallest Tafel slope of ~ 32 mV dec^{-1} for $PtSe_2$ is comparable to that of the Pt/C catalyst or even smaller than that of many other 2D HER catalysts,[43], [117]–[119] indicating the distinct HER activity of $PtSe_2$. Meanwhile, the exchange current density, j_0, can be determined by the Tafel equation [13], yielding a value of 1.5×10^{-5} A cm^{-2} for 76 nm $PtSe_2$. Then a turn over frequency (TOF) at 0 V of 0.054 s^{-1} for $PtSe_2$ can be obtained (**Table 6.2**), which is 4 times that of MoS_2 and $MoSe_2$, revealing the better catalyst efficiency of $PtSe_2$.

Table 6.2 Comparison of TOFs of the edge-terminated $PtSe_2$, MoS_2 and $MoSe_2$ films

Materials	Exchange current density (A cm^{-2})	Exchange current per site (A $site^{-1}$)	TOF (s^{-1})	Reference
MoS_2	2.2×10^{-6}	4.1×10^{-21}	0.013	[13]
$MoSe_2$	2.0×10^{-6}	4.5×10^{-21}	0.014	[13]
$PtSe_2$ (76 nm)	1.5×10^{-5}	1.7×10^{-20}	0.054	This work

In addition, high activity and good stability are equally important for an advanced HER catalyst. Therefore, the current-time curve of the $PtSe_2$ electrode was examined in 0.5 M

H_2SO_4 solution. As shown in **Figure 6.10A** and **Figure 6.10B**, the overpotential of the $PtSe_2$ electrode with current density of 10 mA cm^{-2} current density increases by only 4 mV after 1000 potential cycles. An experimental photo (**Figure 6.10C**) of the $PtSe_2$-coated GC electrode covered by many bubbles, implying the effective HER activity of edge-rich $PtSe_2$ film.

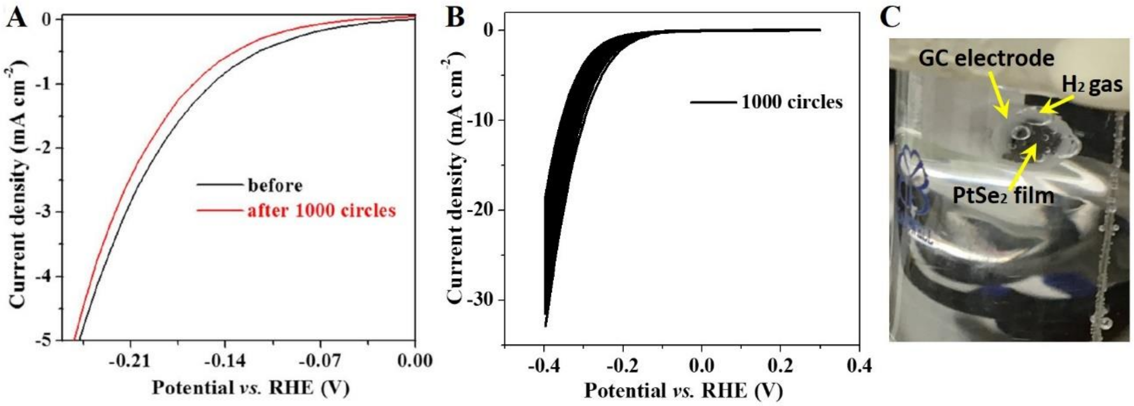

Figure 6.10 (A) polarization curves of $PtSe_2$ film: before and after 1000 circles. (B) Cyclic voltammograms of the $PtSe_2$ film for 1000 circles (C) Digital photos show the H_2 bubbles on $PtSe_2$/GC electrode. The inset shows the working electrode, counter electrode and reference electrode in the measurement system

6.4 Conclusion

In summary, we demonstrate a facile way to prepare scalable and edge-density controllable $PtSe_2$ films by direct selenization of Pt films. The edge density of the $PtSe_2$ films can be as high as 81% with a maximum cathodic current density of 227 mA cm^{-2}. An increasing relationship between edge density and the HER activity is established. Our work opens a new pathway for preparing edge-density controllable materials for HER system.

Chapter 7 Conclusion and Future Works

7.1 Conclusion

A facile method was developed to prepare $AgBiS_2$ NCs in an ambient environment. The $AgBiS_2$ NCs sensitized graphene transistor showed high responsivity of 10^3 to 10^5A/W with infrared illumination.

We synthesized large area polycrystalline $PdSe_2$ by selenization of Pd films. The crystallinity, electrical and optoelectronic properties of $PdSe_2$ were shown to be suitable for photodetection. The responsivity of the $PdSe_2$ phototransistors can reach 1960 A/W under the 980 nm illumination with relatively fast response time. Our work suggests that $PdSe_2$ is a promising material for broadband photodetection.

We also demonstrated a facile way to prepare scalable and edge-density controllable $PtSe_2$ films by direct selenization of Pt films. The edge density of the $PtSe_2$ films can be as high as 81% with a maximum cathodic current density of 227 mA/cm^2. A linear relationship between edge density and the HER activity is established. Our work opens a new pathway for preparing edge-density controllable materials for HER system.

7.2 Future works

Although 2DLMs showed their potential application in HER and photodetection, more efforts should be made on the material synthesis and device fabrication method to realize the application of 2DLMs in the future. Besides the fundamental research of the new 2DLMs needs to be continued, the rate of electron transfer plays an important role in hydrogen gas production in HER and response time in photodetection.

For example, if someone recording high quality video, high gain with video frame rate which is about 30 kHz to 60 kHz are needed. Hence, the tactics of extending the life time of photocarriers, such as photogating effect, seem not the good approach to meet the requirements in those application due to the drawback in response time. Regarding to this issue, increasing the mobility of channel is another feasible method to improve the responsivity and gain, however the mobility of the pristine 2DLMs is limited by the intrinsic materials properties. To overcome this limitation, chemical doping in channel may be a controllable method to enhance the mobility. It is reported that some small organic molecules can increase the mobility of the 2DLMs. Although the mechanism of enhancing mobility by doping is not very clear, the researches on chemical doping would be an interesting topics and beneficial to practical application of 2DLMs.

References

[1] Xie, C.; Mak, C.H.; Tao, X.; Yan, F.; Photodetectors based on two-dimensional layered materials beyond graphene. *Advanced Functional Materials* **2017,** *27*(19), 1603886.

[2] Xia, F.; Wang, H.; Xiao, D.; Dubey, M; Ramasubramaniam, A.; Two-dimensional material nanophotonics. *Nature Photonics* **2014,** *8*(12), 899.

[3] Kufer, D.; Konstantatos, G.; Photo-FETs: phototransistors enabled by 2D and 0D nanomaterials. *ACS Photonics*, **2016,** *3*(12), 2197-2210.

[4] Konstantatos, G.; Sargent, E. H.; Nanostructured materials for photon detection. *Nature Nanotechnology* **2010,** *5*(6), 391.

[5] Park J.; Lee W.; Choi T.; Hwang S.H.; Myoung J.M.; Jung J.H.; et al., Layer-modulated synthesis of uniform tungsten disulfide nanosheet using gas-phase precursors. *Nanoscale* **2015,** *7*(4), 1308-1313.

[6] Koppens, F. H. L.; Mueller, T., Avouris; P., Ferrari; A. C., Vitiello, M. S.; Polini, M.; Photodetectors based on graphene, other two-dimensional materials and hybrid systems. *Nature Nanotechnology* **2014,** *9*(10), 780.

[7] Novoselov K.S.; Geim A. K.; Morozov S. V.; Jiang D.; Zhang Y.;

Dubonos S. V.; et al.; Electric field effect in atomically thin carbon films. *Science* **2004,** *306*(5696), 666-669.

[8] Mueller, T.; Xia, F.; Avouris, P.; Graphene photodetectors for high-speed optical communications. *Nature Photonics* **2010,** *4*(5), 297.

[9] Li, X.; Xiong, X.; Wu, Y.; Toward high-performance two-dimensional black phosphorus electronic and optoelectronic devices. *Chinese Physics B,* **2017,** *26*(3), 037307.

[10] Kufer, D.; Nikitskiy, I.; Lasanta, T.; Navickaite, G.; Koppens, F.H.P.; Konstantatos, G.; Hybrid 2D–0D MoS_2–PbS quantum dot photodetectors. *Advanced Materials,* **2015,** *27*(1), 176-180.

[11] Zhang, W.; Chiu, M. H.; Chen, C. H.; Chen, W.; Li, L. J.; Wee, A. T. S.; Role of metal contacts in high-performance phototransistors based on WSe_2 monolayers. *ACS Nano* **2014**, *8*(8), 8653-8661.

[12] Mayorga-Martinez, C. C.; Mohamad Latiff, N.; Eng, A. Y. S.; Sofer, Z.; Pumera, M.; Black phosphorus nanoparticle labels for immunoassays via hydrogen evolution reaction mediation. *Analytical Chemistry* **2016,** *88*(20), 10074-10079.

[13]Kong, D.; Wang, H.; Cha, J. J.; Pasta, M.; Koski, K. J.; Yao, J.; Cui, Y.; Synthesis of MoS_2 and $MoSe_2$ films with vertically aligned layers. *Nano Letters* **2013,** *13*(3), 1341-1347.

[14]Wu, Z.; Fang, B.; Bonakdarpour, A.; Sun, A.; Wilkinson, D. P.; Wang, D.; WS_2 nanosheets as a highly efficient electrocatalyst for hydrogen evolution reaction. *Applied Catalysis B: Environmental* **2012,** *125*, 59-66.

[15]Novoselov, K. S.; Mishchenko, A.; Carvalho, A.; Neto, A. C.; 2D materials and van der Waals heterostructures. *Science* **2016,** *353*(6298), aac9439.

[16]Viti, L.; Hu, J.; Coquillat, D.; Knap, W.; Tredicucci, A.; Politano, A.; Vitiello, M. S.; Black phosphorus terahertz photodetectors. *Advanced Materials* **2015,** *27*(37), 5567-5572.

[17]Li L.; Yu Y.; Ye G.J.; Ge Q.; Ou X.; Wu H.; et al.; Black phosphorus field-effect transistors. *Nature Nanotechnology* **2014,** *9*(5), 372.

[18]Buscema, M.; Groenendijk, D. J.; Blanter, S. I.; Steele, G. A.; Van Der Zant, H. S.; Castellanos-Gomez, A.; Fast and broadband photoresponse of few-layer black phosphorus field-effect transistors. *Nano Letters* **2014,**

14(6), 3347-3352.

[19]Yin Z.; Li H.; Li H.; Jiang L.; Shi Y.; Sun Y.; et al.; Single-layer MoS_2 phototransistors. *ACS Nano* **2011,** *6*(1), 74-80.

[20]Lopez-Sanchez, O.; Lembke, D.; Kayci, M.; Radenovic, A.; Kis, A.; Ultrasensitive photodetectors based on monolayer MoS_2. *Nature Nanotechnology* **2013,** *8*(7), 497.

[21]Ni Z.; Ma L.; Du S.; Xu Y.; Yuan M.; Fang H.; et al.; Plasmonic silicon quantum dots enabled high-sensitivity ultrabroadband photodetection of graphene-based hybrid phototransistors. *ACS Nano*, **2017,** *11*(10), 9854-9862.

[22]Konstantatos G.; Badioli M.; Gaudreau L.; Osmond J.; Bernechea M.; deArquer F.P.G.; et al.; Hybrid graphene–quantum dot phototransistors with ultrahigh gain. *Nature Nanotechnology* **2012,** *7*(6), 363.

[23]Kwak, D. H.; Lim, D. H.; Ra, H. S.; Ramasamy, P.; Lee, J. S.; High performance hybrid graphene–$CsPbBr_{3-x}I_x$ perovskite nanocrystal photodetector. *RSC Advances* **2016,** *6*(69), 65252-65256.

[24]Bernechea, M.; Miller, N. C.; Xercavins, G.; So, D.; Stavrinadis, A.;

Konstantatos, G.; Solution-processed solar cells based on environmentally friendly $AgBiS_2$ nanocrystals. *Nature Photonics* **2016,** *10*(8), 521.

[25]Konstantatos, G.; Current status and technological prospect of photodetectors based on two-dimensional materials. *Nature Communications* **2018,** *9*(1), 5266.

[26]Huo, N.; Konstantatos, G.; Recent Progress and Future Prospects of 2D-Based Photodetectors. *Advanced Materials* **2018,** *30*(51), 1801164.

[27]Xie, C.; Yan, F.; Perovskite/poly(3-hexylthiophene)/graphene multiheterojunction phototransistors with ultrahigh gain in broadband wavelength region. *ACS applied materials & interfaces* **2017,** *9*(2), 1569-1576.

[28]McCreary, K. M.; Hanbicki, A. T.; Jernigan, G. G.; Culbertson, J. C.; Jonker, B. T.; Synthesis of large-area WS_2 monolayers with exceptional photoluminescence. *Scientific reports* **2016,** *6*, 19159.

[29]Van Der Zande, A. M.; Huang, P. Y.; Chenet, D. A.; Berkelbach, T. C.; You, Y.; Lee, G. H.; et al.; Grains and grain boundaries in highly crystalline monolayer molybdenum disulphide. *Nature Materials* **2013,**

12(6), 554.

[30]Zhou J.; Lin J.; Huang X.; Zhou Y.; Chen Y.; Xia J.; Wang H.; Xie Y.; Yu H.; Lei J.; et al.; A library of atomically thin metal chalcogenides. *Nature* **2018,** *556*(7701), 355.

[31]Wang Z.; Liu P.; Ito Y.; Ning S.; Tan Y.; Fujita T.; Hirata A.; Chen M.; Chemical vapor deposition of monolayer $Mo_{1-x}W_xS_2$ crystals with tunable band gaps. *Scientific Reports* **2016,** *6*, 21536.

[32]Thangaraja A.; Shinde S.M.; Kalita G.; Tanemura M.; An effective approach to synthesize monolayer tungsten disulphide crystals using tungsten halide precursor. *Applied Physics Letters* **2016,** *108*(5), 053104.

[33]Yu Y.; Hu S.; Su L.; Huang L.; Liu Y.; Jin Z.; Purezky A.A.; Geohegan D.B.; Kim K.W.; Zhang Y.; Cao L.; Equally efficient interlayer exciton relaxation and improved absorption in epitaxial and nonepitaxial MoS_2/WS_2 heterostructures. *Nano Letters* **2014,** *15*(1), 486-491.

[34]Huang Y.; Deng H.X.; Xu K.; Wang Z.X.; Wang Q.S.; Wang F.M.; Wang F.; Zhan X.; Li S.; Luo J.; He J.; Highly sensitive and fast phototransistor based on large size CVD-grown SnS_2 nanosheets. *Nanoscale* **2015,** *7*(33),

14093-14099.

[35]Zhao Y.; Qiao J.; Yu Z.; Yu P.; Xu K.; Lau S.P.; Zhou W.; Liu Z.; Wang X.; Ji W.; Chai Y.; High-electron-mobility and air-stable 2D layered $PtSe_2$ FETs. *Advanced Materials* **2017,** *29*(5), 1604230.

[36]Liu E.; Long M.; Zeng J.; Luo W.; Wang Y.; Pan Y.; Zhou W.; Wang B.; Hu W.; Ni Z.; et al.; High responsivity phototransistors based on few-layer ReS_2 for weak signal detection. *Advanced Functional Materials* **2016,** *26*(12), 1938-1944.

[37]Yin L.; Xu K.; Wen Y.; Wang Z.; Huang Y.; Wang F.; Shifa T.A.; Cheng R.; Ma H.; He J.; Ultrafast and ultrasensitive phototransistors based on few-layered $HfSe_2$. *Applied Physics Letters* **2016,** *109*(21), 213105.

[38]Chow W.L.; Yu P.; Liu F.; Hong J.; Wang X.; Zeng Q.; Hsu C.H.; Zhu C.; Zhou J.; Wang X.; et al.; High mobility 2D palladium diselenide field-effect transistors with tunable ambipolar characteristics. *Advanced Materials* **2017,** *29*(21), 1602969.

[39]Zeng L.H.; Wu D.; Lin S.H.; Xie C.; Yuan H.Y.; Lu W.; Lau S.P.; Chai Y.; Luo L.B.; Li Z.J.; Tsang Y.H.; Controlled Synthesis of 2D Palladium

Diselenide for Sensitive Photodetector Applications. *Advanced Functional Materials* **2019,** *29*(1), 1806878.

[40]Long M.; Wang Y.; Wang P.; Zhou X.; Xia H.; Luo C.; Huang S.; Zhang G.; Yan H.; Fan Z.; et al.; Palladium diselenide long-wavelength infrared photodetector with high sensitivity and stability. *ACS Nano* **2019,** *13*(2), 2511-2519.

[41]Dincer I.; Zamfirescu C.; *Sustainable Hydrogen Production*. Elsevier, **2016**.

[42]Dresselhaus M.S.; Thomas I.L.; Alternative energy technologies. *Nature* **2001,** *414*(6861), 332..

[43]Lu Q.; Yu Y.; Ma Q.; Chen B.; Zhang H.; 2D transition-metal-dichalcogenide-nanosheet-based composites for photocatalytic and electrocatalytic hydrogen evolution reactions. *Advanced Materials* **2016,** *28*(10), 1917-1933.

[44]He Z. and Que W., Molybdenum disulfide nanomaterials: structures, properties, synthesis and recent progress on hydrogen evolution reaction. *Applied Materials Today* **2016,** *3*, 23-56.

[45]Yang Y.; Fei H.; Ruan G.; Li Y.; Tour J.M.; Vertically aligned WS_2 nanosheets for water splitting. *Advanced Functional Materials* **2015,** *25*(39), 6199-6204.

[46]Laursen A.B.; Kegnæs S.; Dahl S.; Chorkendorff I.; Molybdenum sulfides —efficient and viable materials for electro-and photoelectrocatalytic hydrogen evolution. *Energy & Environmental Science* **2012,** *5*(2), 5577-5591.

[47]Jaramillo T.F.; Jørgensen K.P.; Bonde J.; Nielsen J.H.; Horch S.; Chorkendorff I.; Identification of active edge sites for electrochemical H_2 evolution from MoS_2 nanocatalysts. *Science* **2007,** *317*(5834), 100-102.

[48]Dasari B.L.; Nouri J.M.; Brabazon D.; Naher S.; Graphene and derivatives–Synthesis techniques, properties and their energy applications. *Energy* **2017,** *140*, 766-778.

[49]Wu J.; Koon G.K.W.; Xiang D.; Han C.; Toh C.T.; Kulkarni E.S.; Verzhbitskiy I.; Carvalho A.; Rodin A.S.; Koenig S.P.; et al.; Colossal ultraviolet photoresponsivity of few-layer black phosphorus. *ACS Nano* **2015,** *9*(8), 8070-8077.

[50]Ma C.; Shi Y.; Hu W.; Chiu M.H.; Liu Z.; Bera A.; Li F.; Wang H.; Li L.J.; Wu T.; Heterostructured $WS_2/CH_3NH_3PbI_3$ photoconductors with suppressed dark current and enhanced photodetectivity. *Advanced Materials* **2016,** *28*(19), 3683-3689.

[51]Coleman J.N.; Lotya M.; O'Neill1 A.; Bergin S.D.; King P.J.; Khan U.; Young K.; Gaucher A.; De S.; Smith R.J.; et al.; Two-dimensional nanosheets produced by liquid exfoliation of layered materials. *Science* **2011,** *331*(6017), 568-571.

[52]Nicolosi V.; Chhowalla M.; Kanatzidis M.G.; Strano M.S.; Coleman J.N.; Liquid exfoliation of layered materials. *Science* **2013,** *340*(6139), 1226419.

[53]Backes C.; Higgins T.M.; Kelly A.; Boland C.; Harvey A.; Hanlon D.; Coleman J.N.; Guidelines for exfoliation, characterization and processing of layered materials produced by liquid exfoliation. *Chemistry of Materials* **2016,** *29*(1), 243-255.

[54]Zeng Z.; Yin Z.; Huang X.; Li H.; He Q.; Lu G.; Boey F.; Zhang H.; Single-Layer Semiconducting Nanosheets: High-yield preparation and device fabrication. *Angewandte Chemie International Edition* **2011,**

50(47), 11093-11097.

[55] Sun Z.Z.; Yan Z.; Yao J.; Beitler E.; Zhu .Y; Tour J.M.; Growth of graphene from solid carbon sources. *Nature* **2010,** *468*(7323), 549.

[56] Tao L.; Lee J.; Chou H.; Holt M.; Ruoff R.S; Akinwande D.; Synthesis of high quality monolayer graphene at reduced temperature on hydrogen-enriched evaporated copper (111) films. *ACS Nano,* **2012,** *6*(3), 2319-2325.

[57] Sheng Y.; Tan H.; Wang X.; Warner J.H.; Hydrogen addition for centimeter-sized monolayer tungsten disulfide continuous films by ambient pressure chemical vapor deposition. *Chemistry of Materials* **2017,** *29*(11), 4904-4911.

[58] Kim Y.; Bark H.; Ryu G.H.; Lee Z.; Lee C.; Wafer-scale monolayer MoS_2 grown by chemical vapor deposition using a reaction of MoO_3 and H_2S. *Journal of Physics: Condensed Matter* **2016,** *28*(18), 184002.

[59] Xue Y.; Zhang Y.; Liu Y.; Liu H.; Song J.; Sophia J.; Liu J.; Xu Z.; Xu Q.; Wang Z.; et al.; Scalable production of a few-layer MoS_2/WS_2 vertical heterojunction array and its application for photodetectors. *ACS Nano* **2015,** *10*(1), 573-580.

[60]Zhou X.; Zhang Q.; Gan L.; Li H.; Zhai T.; Large-Size Growth of Ultrathin SnS_2 Nanosheets and High Performance for Phototransistors. *Advanced Functional Materials* **2016,** *26*(24), 4405-4413.

[61]Zhang E.; Jin Y.; Yuan X.; Wang W.; Zhang C.; Tang L.; Liu S.; Zhou P.; Hu W.; Xiu F.; ReS_2-Based Field-Effect Transistors and Photodetectors. *Advanced Functional Materials* **2015,** *25*(26), 4076-4082.

[62]Hoffman J.B.; Schleper A.L.; Kamat P.V.; *Journal of the American Chemical Society* **2015,** *138*(27), 8603-8611.

[63]Chen X.; Liu X.; Wu B.; Nan H.; Guo H.; Ni Z.; Wang F.; Wang X.; Shi Y.; Wang X.; Improving the performance of graphene phototransistors using a heterostructure as the light-absorbing layer. *Nano Letters* **2017,** *17*(10), 6391-6396.

[64]Li J.; Niu L.; Zheng Z.; Yan F.; Photosensitive graphene transistors. *Advanced Materials* **2014,** *26*(31), 5239-5273.

[65]Schwierz, F.; Graphene transistors. *Nature Nanotechnology* **2010,** *5*(7), 487.

[66]Bonaccorso F.; Sun Z.; Hasan T.; Ferrari A.C.; Graphene photonics and

optoelectronics. *Nature Photonics* **2010,** *4*(9), 611.

[67]Xia F.; Mueller T.; Lin Y.; Valdes-garcia A.; Avouris P.; Ultrafast graphene photodetector. *Nature Nanotechnology* **2009,** *4*(12), 839.

[68]Liu H.; Du Y.; Deng Y.; Ye P.D.; Semiconducting black phosphorus: synthesis, transport properties and electronic applications. *Chemical Society Reviews* **2015,** *44*(9), 2732-2743.

[69]Jung C.; Kim S.; Moon H.; Han G.; Kwon J.; Hong Y.K.; Omkaram I.; Yoon Y.; Kim S.; Park J.; Highly crystalline CVD-grown multilayer $MoSe_2$ thin film transistor for fast photodetector. *Scientific Reports* **2015,** *5*, 15313.

[70]Lu J.; Carvalho A.; Liu H.; Lim S.X.; Castro Neto A.H.; Sow C.H.;. Hybrid Bilayer WSe_2–$CH_3NH_3PbI_3$ Organolead Halide Perovskite as a High-Performance Photodetector. *Angewandte Chemie* **2016,** *128*(39), 12124-12128.

[71]Xu K.; Wang Z.; Wang F.; Huang Y.; Wang F.; Yin L.; Jiang C.; He J.; Ultrasensitive Phototransistors Based on Few-Layered HfS_2. *Advanced Materials* **2015,** *27*(47), 7881-7887.

[72]Tsai D.S.; Liu K.K.; Lien D.H.; Tsai M.L.; Kang C.F.; Lin C.A.; Li L.J.; He J.H.; Few-layer MoS_2 with high broadband photogain and fast optical switching for use in harsh environments. *ACS Nano* **2013,** *7*(5), 3905-3911.

[73]Chen J.; Liu B.; Liu Y.; Tang W.; Nai C.T.; Li L.; Zheng J.; Gao L.; Zheng Y.; Shin H.S.; et al.; Chemical Vapor Deposition of Large-Sized Hexagonal WSe_2 Crystals on Dielectric Substrates. *Advanced materials* **2015,** *27*(42), 6722-6727.

[74]Kagan C.R.; Lifshitz E.; Sargent E.H.; Talapin D.V.; Building devices from colloidal quantum dots. *Science* **2016,** *353*(6302), aac5523.

[75]Perea-López N.; Lin Z.; Pradhan N.R.; Iñiguez-Rábago A.; Elías A.L.; McCreary A.; Lou J.; Ajayan P.M.; Terrones H.; Balicas L.; Terrones M.; CVD-grown monolayered MoS_2 as an effective photosensor operating at low-voltage. *2D Materials* **2014,** *1*(1), 011004.

[76]Perea-lópez N.; Elías A.L.; Berkdemir A.; Castro-Beltran A.; Gutiérrez H.R.; Feng S.; LV R.; Hayashi T.; López-Urías F.; Ghosh S.; et al.; Photosensor device based on few-layered WS_2 films. *Advanced Functional Materials* **2013,** *23*(44), 5511-5517.

[77]Lan C.; Li C.; Yin Y.; Liu Y.; Large-area synthesis of monolayer WS_2 and its ambient-sensitive photo-detecting performance. *Nanoscale* **2015,** *7*(14), 5974-5980.

[78]Yu Y.; Zhang Y.; Song X.; Zhang H.; Cao M.; Che Y.; Dai H.; Yang J.; Zhang H.; Yao J.; PbS-decorated WS_2 phototransistors with fast response. *ACS Photonics* **2017,** *4*(4), 950-956.

[79]Chang Y.; Zhang W.; Zhu Y.; Han Y.; Pu J.; Chang J.; Hsu W.; Huang J.; Hsu C.; Chiu M.; et al.; Monolayer $MoSe_2$ grown by chemical vapor deposition for fast photodetection. *ACS Nano* **2014,** *8*(8), 8582-8590.

[80]Pradhan N.R.; Ludwig J.; Lu Z.; Rhodes D.; Bishop M.M.; Thirunavukkuarasu K.; McGill S.A.; Smirnov D.; Balicas L.; High photoresponsivity and short photoresponse times in few-layered WSe_2 transistors. *ACS Applied Materials & Interfaces* **2015,** *7*(22), 12080-12088.

[81]Yang S.; Tongay S.; Li Y.; Yue Q.; Xia J.; Li S.; Li J.; Wei S.; Layer-dependent electrical and optoelectronic responses of $ReSe_2$ nanosheet transistors. *Nanoscale* **2014,** *6*(13), 7226-7231.

[82]Hafeez M.; Gan L.; Li H.; Ma Y.; Zhai T.; Large-Area Bilayer ReS_2

Film/Multilayer ReS_2 Flakes Synthesized by Chemical Vapor Deposition for High Performance Photodetectors. *Advanced Functional Materials* **2016,** *26*(25), 4551-4560.

[83]Su G.; Hadjiev V.G.; Loya P.E.; Zhang J.; Lei S.; Maharjan S.; Dong P.; Ajayan P.M.; Lou J.; Peng H.; Chemical vapor deposition of thin crystals of layered semiconductor SnS_2 for fast photodetection application. *Nano Letters* **2014,** *15*(1), 506-513.

[84]Gao L.; Chen C.; Zeng K.; Ge C.; Yang D.; Song H.; Tang J.; Broadband, sensitive and spectrally distinctive SnS_2 nanosheet/PbS colloidal quantum dot hybrid photodetector. *Light: Science & Applications* **2016,** *5*(7), e16126.

[85]Voiry, D.; Yang, J.; Chhowalla, M.; Recent strategies for improving the catalytic activity of 2D TMD nanosheets toward the hydrogen evolution reaction. *Advanced Materials* **2016,** *28*(29), 6197-6206.

[86]Trasatti, S.; Work function, electronegativity, and electrochemical behaviour of metals: III. Electrolytic hydrogen evolution in acid solutions. *Journal of Electroanalytical Chemistry and Interfacial Electrochemistry*

1972, *39*(1), 163-184.

[87] Vandenabeele, P.; *Practical Raman Spectroscopy: An Introduction*. Chichester, United Kingdom: Wiley, **2013**,.

[88] Saran R.; Curry R.J.; Lead sulphide nanocrystal photodetector technologies. *Nature Photonics* **2016,** *10*(2), 81.

[89] Sun Z.; Liu Z.; Li J.; Tai G.; Lau S.P.; Yan F; Infrared photodetectors based on CVD-grown graphene and PbS quantum dots with ultrahigh responsivity. *Advanced Materials* **2012,** *24*(43), 5878-5883.

[90] Cao Y.; Stavrinadis A.; Lasanta T.; So D.; Konstantatos G.; The role of surface passivation for efficient and photostable PbS quantum dot solar cells. *Nature Energy* **2016,** *1*(4), 16035.

[91] Flora G.; Gupta D.; Tiwari A.; Toxicity of lead: a review with recent updates. *Interdisciplinary Toxicology* **2012,** *5*(2), 47-58.

[92] Guin S.N.; Biswas K.; Cation disorder and bond anharmonicity optimize the thermoelectric properties in kinetically stabilized rocksalt $AgBiS_2$ nanocrystals. *Chemistry of Materials* **2013,** *25*(15), 3225-3231.

[93] Lee J.S.; Kovalenko M.V.; Huang J.; Chung D.S.; Talapin D.V.; Band-

like transport, high electron mobility and high photoconductivity in all-inorganic nanocrystal arrays. *Nature Nanotechnology* **2011,** *6*(6), 348.

[94]Wang R.; Shang Y.; Kanjanaboos P.; Zhou W.; Ning Z.; Sargent E.H.; Colloidal quantum dot ligand engineering for high performance solar cells. *Energy & Environmental Science* **2016,** *9*(4), 1130-1143.

[95]Tang J.; Kemp K.W.; Hoogland S.; Jeong K.S.; Liu H.; Levina L.; Furukawa M.; Wang X.; Debnath R.; Cha D.; et al.; Colloidal-quantum-dot photovoltaics using atomic-ligand passivation. *Nature materials* **2011,** *10*(10), 765.

[96]Yasaei P.; Kumar B.; Foroozan T.; Wang C.; Asadi M.; Tuschel D.; Indacochea J.E.; Klie R.F.; Salehi-Khojin A.; High-quality black phosphorus atomic layers by liquid-phase exfoliation. *Advanced Materials* **2015,** *27*(11), 1887-1892.

[97]Chen J.; Tang W.; Tian B.; Liu B.; Zhao X.; LiuY.; Ren T.; Liu W.; Geng D.; Jeong H.Y.; et al.; Chemical vapor deposition of high-quality large-sized MoS_2 crystals on silicon dioxide substrates. *Advanced Science* **2016,** *3*(8), 1500033.

[98]Lee, Y. H.; Zhang X.Q.; Zhang W.; Chang M.; Lin C.; Chang K.D.; Yu Y.C.;, Wang J.T.W.; Chang C.S.; Li L.J.; Lin T.W.; Synthesis of large-area MoS2 atomic layers with chemical vapor deposition. *Advanced Materials* **2012,** *24*(17), 2320-2325.

[99]Yang S.Y.; Shim G.W.; Seo S.B.; Choi S.Y.; Effective shape-controlled growth of monolayer MoS 2 flakes by powder-based chemical vapor deposition. *Nano Research* **2017,** *10*(1), 255-262.

[100] Wang Y.; Li L.; Yao W.; Song S.; Sun J.T.; Pan J.; Ren X.; Li C.; Okunishi E.; Wang Y.; et al.; Monolayer $PtSe_2$, a new semiconducting transition-metal-dichalcogenide, epitaxially grown by direct selenization of Pt. *Nano Letters* **2015,** *15*(6), 4013-4018.

[101] O'Brien M.; McEvoy N.; Motta C.; Zheng J.Y.; Berner N.C.; Kotakoski J.; Elibol K.; Pennycook T.J.; Meyer J.; Yim C.; Raman characterization of platinum diselenide thin films. *2D Materials* **2016,** *3*(2), 021004.

[102] Lin S.; Liu Y.; Hu Z.; Lu W.; Mak C.H.; Zeng L.; Zhao J.; Li Y.; Yan F.; Tsang Y.H.; et al.; Tunable active edge sites in $PtSe_2$ films towards

hydrogen evolution reaction. *Nano Energy* **2017,** *42*, 26-33.

[103] Zeng L.; Tao L.; Tang C.Y.; Zhou B.; Long H.; Chai Y.; Lau S.P.; Tsang Y.H.; High-responsivity UV-vis photodetector based on transferable WS_2 film deposited by magnetron sputtering. *Scientific Reports* **2016,** *6*, 20343.

[104] Oyedele A.D.; Yang S.; Liang L.; Puretzky A.A.; Wang K.; Zhang J.; Yu P.; Pudasaini P.R.; Ghash A.W.; Liu Z.; et al.; $PdSe_2$: Pentagonal two-dimensional layers with high air stability for electronics. *Journal of the American Chemical Society* **2017,** *139*(40), 14090-14097.

[105] Zhang G.; Amani M.; Chaturvedi A.; Tan C.; Bullock J.; Kim H.; Lien D.; Scott M.C.; Zhang H.; Javey A.; Optical and electrical properties of two-dimensional palladium diselenide. *Applied Physics Letters* **2019,** *114*(25), 253102.

[106] Late D.J.; Liu B.; Matte H.S.S.R.; Dravid V.P.; Rao C.N.R.; Hysteresis in single-layer MoS_2 field effect transistors. *ACS Nano* **2012,** *6*(6), 5635-5641.

[107] Wang A.; Yan X.; Zhang M.; Sun S.; Yang M.; Shen W.; Pan X.;

Wang P.; Deng Z.; Controlled synthesis of lead-free and stable perovskite derivative Cs_2SnI_6 nanocrystals via a facile hot-injection process. *Chemistry of Materials* **2016,** *28*(22), 8132-8140.

[108] Dünkel, L.; Photoelectronic Properties of Semiconductors. *Zeitschrift für Physikalische Chemie* **1994,** *184*(1-2), 296-297.

[109] Xie C.; You P.; Liu Z.; Li L.; Yan F.; Ultrasensitive broadband phototransistors based on perovskite/organic-semiconductor vertical heterojunctions. *Light: Science & Applications* **2017,** *6*(8), e17023.

[110] Liang Q.; Wang Q.; Zhang Q.; Wei J.; Lim S.X.; Zhu R.; Hu J.; Wei W.; Lee C.; Sow C.; et al.; High-Performance, Room Temperature, Ultra-Broadband Photodetectors Based on Air-Stable $PdSe_2$. *Advanced Materials* **2019,** *31*(24), 1807609.

[111] Zhang W.; Huang J.; Chen C.; Chang Y.; Cheng Y.; Li L.J.; High-gain phototransistors based on a CVD MoS_2 monolayer. *Advanced Materials* **2013,** *25*(25), 3456-3461.

[112] Huang Y.; Xu K.; Wang Z.; Shifa T.A.; Wang Q.; Wang F.; Jiang C.; He J.; Designing the shape evolution of $SnSe_2$ nanosheets and their

optoelectronic properties. *Nanoscale* **2015,** *7*(41), 17375-17380.

[113] Wang Y.; Li L.; Yao W.; Song S.; Sun J.T.; Pan J.; Ren X.; Li C.; Okunishi E.; Wang Y.; et al.; Monolayer $PtSe_2$, a new semiconducting transition-metal-dichalcogenide, epitaxially grown by direct selenization of Pt. *Nano Letters* **2015,** *15*(6), 4013-4018.

[114] Chia X.; Adriano A.; Lazar P.; Sofer Z.; Luxa J.; Pumera M.; Layered platinum dichalcogenides (PtS_2, $PtSe_2$, and $PtTe_2$) electrocatalysis: monotonic dependence on the chalcogen size. *Advanced Functional Materials* **2016,** *26*(24), 4306-4318.

[115] Yim C.; Lee K.; McEvoy N.; O'Brien M.; Riazimehr S.; Berner N.C.; Cullen C.P.; Kotakoski J.; Meyer J.C.; Lemme M.C.; Duesberg G.S.; High-performance hybrid electronic devices from layered $PtSe_2$ films grown at low temperature. *ACS Nano* **2016,** *10*(10), 9550-9558.

[116] Zeng M.; Li Y.; Recent advances in heterogeneous electrocatalysts for the hydrogen evolution reaction. *Journal of Materials Chemistry A* **2015,** *3*(29), 14942-14962.

[117] Shi Y.; Zhang B.; Recent advances in transition metal phosphide

nanomaterials: synthesis and applications in hydrogen evolution reaction. *Chemical Society Reviews* **2016,** *45*(6), 1529-1541.

[118] Wu Z.; Wang J.; Liu R.; Xia K.; Xuan C.; Guo J.; Lei W.; Wang D.; Facile preparation of carbon sphere supported molybdenum compounds (P, C and S) as hydrogen evolution electrocatalysts in acid and alkaline electrolytes. *Nano Energy* **2017,** *32*, 511-519.

[119] Bae C.; Ho T.A.; Kim H.; Lee S.; Lim S.; Kim M.; Yoo H.; Montero-Moreno J.M.; Park J.H.; Shini H.; Bulk layered heterojunction as an efficient electrocatalyst for hydrogen evolution. *Science Advances* **2017,** *3*(3), e1602215.